Eddy Current Damping Stroke Sensor

Thesis by

Shane Shahrestani

In Partial Fulfillment of the Requirements for the degree of

Doctor of Philosophy

Caltech

California Institute of Technology

Pasadena, California

2021

(Defended March 26, 2021)

© 2021

Shane Shahrestani

ORCID: 0000-0001-7561-4590

To My Parents, Marjaneh and Shahram

ACKNOWLEDGEMENTS

car I promised you as a child! I would like to thank my aunts, uncles, and cousins for helping raise me. Khalejoon and Alijoon, thank you for your kindness and patience. Kiano and Shelby, thanks for being my two first friends and putting up with me. I love you all.

To my friends, thank you for being my support system. To Paige McGhee: thank you for always being there for me and supporting my dreams. Even at my lowest, you're always there to pick me up. To Andy Ton, Candice Le, Nate Christian, and Brandon Yang: thank you for always having my back as I discovered myself through UCLA and beyond. To Ariana Zargarian, Alex Ballatori, Tony Chen, Sonia Rodrigues, Kavitha Thiagarajan, and Alice Laughlin: thank you for your friendship and emotional support through medical school. I would not be here if it weren't for all of your love and support. I hope you all know how much you mean to me and I hope that our friendships continue in perpetuity.

I count myself lucky to have two of the best mentors any student could ask for: Dr. Yu-Chong Tai and Dr. Gabriel Zada. Not only are they excellent examples of academic success, but they are also both exceptional human beings. Thank you, Dr. Tai, for teaching me so much about fundamental research. His knowledge on all engineering topics is extremely impressive, and he always somehow has a solution to every problem that may arise in my research. Dr. Tai is a rare example of a professor who deeply cares about his students. It is his guidance and support that has allowed me to develop this medical device, and I am thankful for the time and effort he gave to us as students in his lab. I would also like to thank Dr. Zada for being an incredible clinical mentor and friend. Dr. Zada's clinical input throughout this project undoubtedly helped guide the efficient development of this device. After working with him, I hope to one day be a neurosurgeon half as skilled and caring as he is.

ABSTRACT

Existing paradigms for stroke diagnosis typically involve computed tomography (CT) or magnetic resonance (MR) imaging to classify ischemic versus hemorrhagic stroke variants, as treatment for these subtypes varies widely. Delays in diagnosis and issues related to transport of unstable patients may worsen neurological status. As such, translational medical devices that accelerate time to treatment in the field or hospital setting have the potential to lower morbidity and mortality in stroke patients. We demonstrated feasibility of rapid and accurate bedside stroke detection using a novel, handheld portable eddy current damping imaging device in laboratory benchtop as well as live human clinical ischemic and hemorrhagic stroke settings. We show that diagnosis of stroke may potentially be reduced from several hours to minutes, with additional spatial localization of intracranial hemorrhage, thereby rapidly guiding time-sensitive medical decisions for clinical intervention such as tissue plasminogen activator (tPA). The sensor additionally detects ischemic and hemorrhagic lesions located deep inside the brain, and its range can be selectively tuned during sensor design and fabrication.

PUBLISHED CONTENT AND CONTRIBUTIONS

1. Shahrestani, S., Zada, G., Chou, T.C., Toy, B., Yao, B., Garrett, N., Sanossian, N., Brunswick, A., Tai, Y.C. "Noninvasive Transcranial Classification of Stroke Using A Portable Eddy Current Damping Sensor." Submitted.

S.S. participated in the conception of the project, constructed the sensor, conducted the human experiments, wrote the manuscript, and created the computational models.

2. Shahrestani, S., Zada, G., Tai, Y.C. "Development of Computational Models for Microtesla-Level Magnetic Brain Scanning: A Novel Avenue for Device Development." Submitted.

S.S. participated in the conception of the project, constructed the sensor, conducted the cadaver experiments, wrote the manuscript, and created the computational models.

3. Shahrestani, S., Chou, T.C., Zada, G., Borok, Z., Rao, A.P., Tai, Y.C. "A Wearable Eddy Current Damping Pulmonary Function Sensor for Continuous Non- Contact Point-Of-Care Monitoring During the COVID-19 Pandemic." Submitted.

S.S. participated in the conception of the project, constructed the sensor, conducted the human experiments, wrote the manuscript, and created the computational models.

TABLE OF CONTENTS

LIST OF ILLUSTRATIONS

LIST OF TABLES

CHAPTER 1: BACKGROUND

Stroke continues to be the second leading cause of death worldwide and results in upwards of 5.5 million casualties per year [1, 2]. The high prevalence and rates of disability associated with stroke cost the United States healthcare system more than $71 billion per year, and recent studies from the Center for Medicare and Medicaid Innovation (CMMI) Bundled Payments for Care Improvement (BPCI) initiative suggest that stroke may be contributing towards healthcare losses due to high rates of readmission and complications [3, 4]. As such, the high rates of morbidity and mortality following stroke continue to inspire contemporary research with hopes of reducing the time to treatment, expanding diagnostic technologies, and facilitating patient triage to minimize post-stroke complications.

This thesis aims to develop a novel medical device to accelerate stroke diagnosis and classification. The work described here aims to describe the clinical profile of ischemic and hemorrhagic stroke, explain the bottlenecks in current diagnostic technologies, and propose a contemporary solution for rapid stroke diagnosis and patient triage. The solution described here utilizes a portable eddy current damping (ECD) magnetic sensor to allow for rapid bedside diagnosis and imaging of stroke. Interdisciplinary collaboration dovetailing medicine, electrical engineering, mechanical engineering, and computational science may allow for the development of novel medical devices capable of reshaping the paradigms used in current stroke diagnosis and management.

Chapter 1 presents the clinical picture of stroke and discusses the current paradigm for treatment of stroke subtypes. Chapter 2 explains the operating principles of the ECD sensor. This discussion includes the underlying physics and construction of the biodevice. Further, it is here that we discuss optimization of our sensor circuitry and limitations that we faced during the development phase. Chapter 3 marks the start of the results and includes the benchtop experimentation performed with this sensor. Tuning curves are discussed with respect to the sensitivity to volume and distance for each sensor. In addition, preliminary experiments demonstrating device feasibility with plastic skull models are described and image production methodology is outlined. From here, Chapter 4 demonstrates the translational capabilities of the ECD sensor, moving from benchtop experiments to human cadaver experimentation. The success of these cadaver experiments allowed for Institutional Review Board (IRB) approval and testing on live human stroke patients, outlined in Chapter 5. Output from the ECD sensor is compared to that of computed tomography (CT) scanning for a number of stroke patients, allowing for the discussion of device accuracy. Chapter 6 gives some insight into the theoretical limits of the ECD sensor through finite element modeling (FEM) and explores mechanical optimization of the device. Lastly, Chapter 7 provides a conclusion, summarizing the advancements, results, and limitations seen in the previous chapters.

Prior to human testing, several experiments were conducted using cadaveric human heads. I would like to thank the donors who were generous enough to donate their bodies for the advancement of science. In addition, I would also like to thank the many live human stroke patients, as well as their families, who agreed to be a part of this study. There is something to be said about the character of individuals who participate in medical research knowing that while they face no potential

benefits, their involvement may allow for the creation of a device that can help others who may face a similar situation. We thank you all for your kindness and generosity.

1.1 Structure of the Brain

On average, the length of a human head length is approximately 19.7cm for males and 18.7cm for females, and the average height is approximately 23.2cm for males and 21.6cm for females. The tissue of the scalp is organized into five distinct layers: skin, dense connective tissue, epicranial aponeurosis, loose areolar connective tissue, and periosteum [5]. Within the scalp, most of the neurovasculature can be found within the dense connective tissue. Additionally, body mass index (BMI) and sex-dependent variations in adipose tissue may be found within the dense connective tissue of the scalp. Similarly, the average skull thicknesses for frontal, parietal, and occipital skull regions are 6.58mm, 5.37mm, and 7.56mm respectively for males and 7.48mm, 5.58mm, and 8.17mm respectively for females [6]. Below the skull lie the meningeal layers, which include the dural, arachnoid, and pial layers respectively.
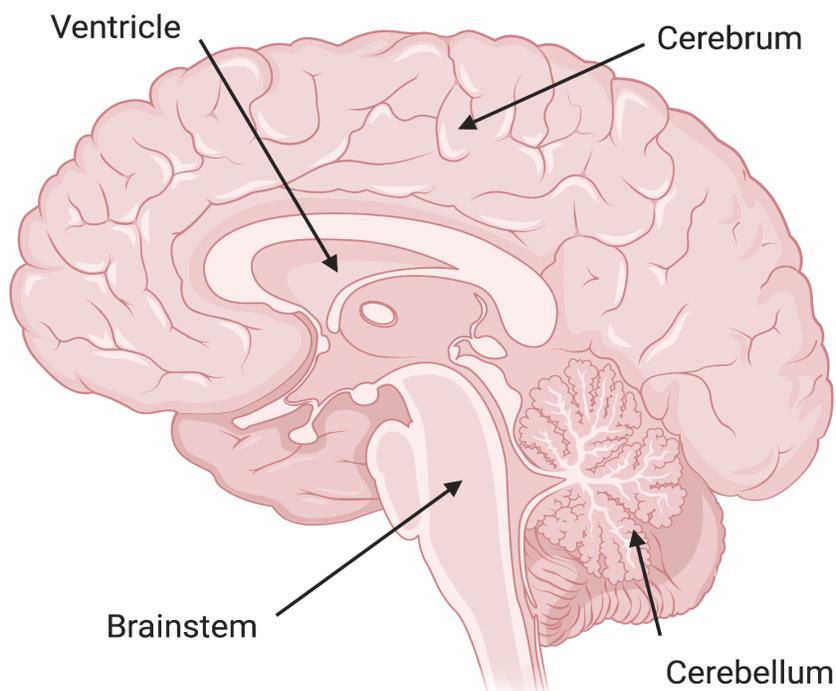
Figure 1-1. Anatomy of the human brain. Created with BioRender.com

The brain is organized into three main components: the cerebrum, cerebellum, and brainstem (Figure 1-1). Each component is bilaterally symmetrical and the empty space within each component forms the ventricular spaces, which contain cerebrospinal fluid (CSF). The anterior cerebral artery (ACA) supplies most of the anterior cerebrum (frontal lobe), the middle cerebral artery (MCA) supplies most of the medial cerebrum (parts of the frontal and temporal/parietal lobes), and the posterior cerebral artery (PCA) supplies most of the posterior cortex (occipital lobe). Deeper brain structures are supplied by a mix of the main cerebral arteries and other arterial branches, including those from the basilar and vertebral arteries.

1.2 Intracranial Pathology: Ischemic Stroke

Ischemic stroke occurs when an intracerebral vessel is obstructed by a thrombus or embolus, resulting in ischemia-driven neuronal damage. As such, ischemic strokes involving the MCA occur most frequently due to the high number of bifurcations from the MCA to supply blood to a large territory of the brain [7]. Ischemic strokes are further subdivided by etiology, with large artery thrombotic strokes due to atherosclerosis making up 20% of cases, small artery (lacunar) strokes due to microatheromas making up 25% of cases, cardiogenic embolic stroke making up 15% of cases, cryptogenic strokes of unknown origin making up 5-10% of cases, and strokes associated with other causes (such as drug use) making up 20-25% of cases [2].

Risk factors for ischemic stroke include both lifestyle and genetic contributors. Lifestyle factors including tobacco use, alcohol use, diabetes mellitus, and high fat diets may increase the risk for the occurrence of an ischemic stroke [8, 9]. Further, prior studies have shown that a family history of ischemic stroke may increase the risk for both large and small-vessel ischemic stroke [10]. Deeper investigation into specific genetic polymorphisms resulting in familial transmission of ischemic stroke have revealed that factor V Leiden Arg506Gln (OR, 1.33; 95% CI, 1.12-1.58), methylenetetrahydrofolate reductase C677T (OR, 1.24; 95% CI, 1.08-1.42), prothrombin G20210A (OR, 1.44; 95% CI, 1.11-1.86), and angiotensin-converting enzyme insertion/deletion (OR, 1.21; 95% CI, 1.08-1.35) may be responsible for the increased risk of ischemic stroke [11]. Lastly, several medical conditions may increase an individual's risk of ischemic stroke. Individuals with a prior history of transient ischemic attack (TIA) have been shown to have an increased odds of experiencing an ischemic stroke due to their similar neurovascular disease origins [8, 12]. Also, individuals with atrial fibrillation are at a higher risk for embolism production due to variable local hemostasis, and the production of emboli increases the risk for cardiogenic embolic stroke [13,

14]. Thus, the multifaceted etiology of ischemic stroke has resulted in difficulties in prevention and management.

When an individual experiences an ischemic stroke, several characteristic symptoms are often present. Sudden weakness of the face or limbs, confusion, difficulty speaking, visual disturbances, difficulty walking, impaired coordination, and headache are all common symptoms experienced during an ischemic stroke [15]. Oftentimes these symptoms present unilaterally on one side of the body. Because the nervous system is organized such that one side of the brain controls the motor and sensory function of the contralateral body, many times it is possible to identify the laterality of the stroke based on the side of the body affected. If an ischemic stroke occurs in a deeper brain region, such as the brainstem, the presenting symptoms may be much more severe and include problems with vital functions, including breathing.

Diagnosis of ischemic stroke involves clinical suspicion and diagnostic imaging procedures, which include either magnetic resonance imaging (MRI) or CT imaging. For patients with suspected stroke, CT imaging is often preferred over MRI because of its increased temporal resolution. An example noncontrast CT image of an ischemic stroke is seen in Figure 1-2.
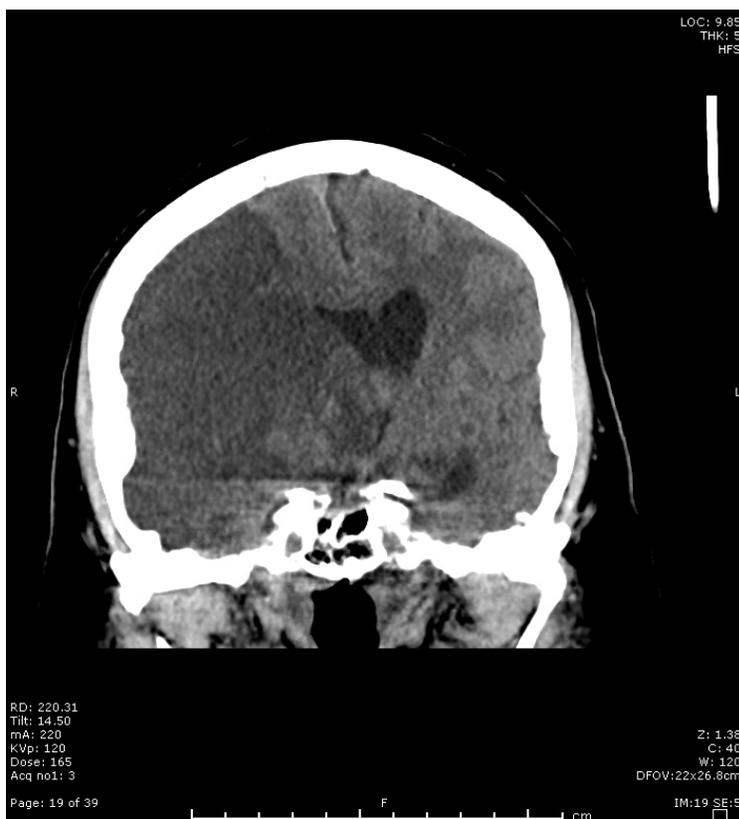
Figure 1-2. Coronal representation of ischemic stroke on noncontrast CT imaging

On CT imaging, early ischemic changes appear as areas of hypodensity, with loss of gray-white matter differentiation and sulcal effacement resulting from tissue swelling [16]. However, the presentation of ischemic stroke on imaging may vary as a function of time following ictus. In the hyperacute phase (0-6 hours following ictus), clinical imaging may not accurately pick-up regions of ischemia. However, as the ictus transitions from the hyperacute phase to acute (6-24 hours), subacute (1-7 days), and chronic (>1 month) phases, the lesion may become increasingly apparent on CT imaging [17]. As such, repeat imaging following ischemic stroke occurs frequently to best manage the changing landscape surrounding the ictus.

Lastly, once an ischemic stroke has been identified, the current mainstay for treatment involves intravenous thrombolysis with tissue-type plasminogen activator (tPA) within 4.5 hours of stroke onset [18, 19]. Administration of tPA outside of this time window may reduce drug efficacy and result in severe drug-mediated complications, including intracerebral hemorrhage (ICH) [20, 21]. Additionally, endovascular thrombectomy (EVT) provides another treatment option for patients diagnosed with ischemic stroke [22]. EVT entails either using stents to recanalize and retrieve the thrombus or using endovascular suction devices to suck the thrombus out of the vessel. The safety of both techniques has been proven and several studies have demonstrated that both EVT techniques yield similar patient outcomes [23, 24]. However, treatment with EVT is still highly time-dependent, and the current recommendations mandate EVT treatment within 3-4.5 hours in anterior circulation strokes and within 24 hours for posterior circulation strokes for best patient outcomes [22, 25–27]. Thus, it is clear that rapid diagnosis of stroke may yield the best potential outcomes by facilitating timely treatment.

1.3 Intracranial Pathology: Hemorrhagic Stroke

Hemorrhagic stroke, also known as ICH, is defined as a rupture in a weak intracranial artery resulting in bleeding within the brain. While hemorrhagic strokes (~13% of cases) are less common than ischemic strokes (~87% of cases)[28], they are associated with significant higher rates of morbidity and mortality. As such, ischemic stroke has been associated with a 60% one-year survival rate and ICH has been associated with a 38% one-year survival rate [29]. Oftentimes, hemorrhagic stroke is subdivided by the location of the ICH into one of four categories: epidural hematomas (above the dura mater but below the skull) account for 5-15% of all hemorrhagic stroke

mortalities and often occur in the context of skull fracture and head injury, subdural hematoma (below the dura mater but above the arachnoid mater) occurs in 5-25% of patients with head injury and affects males twice as often as females, subarachnoid hemorrhages (between the brain and arachnoid mater) account for about 5% of all hemorrhagic strokes, and intraparenchymal hemorrhages (within the brain parenchyma) account for 10-20% of all hemorrhagic strokes and often occur in elderly patients [30].

Risk factors for ICH are similar to those of ischemic stroke and include tobacco use, alcohol use, diabetes mellitus, and a high-fat diet [31–33]. However, hypertension has been shown to be the most significant risk factor for ICH, with inadequate blood pressure control having a hazard ratio of 3.53 in lobar ICH and 4.23 in nonlobar ICH [34]. Furthermore, a family history of ICH has been shown to increase the risk of both lobar ICH (odds ratio: 3.9) and nonlobar ICH (odds ratio: 5.4), and previous studies have hypothesized that the familial inheritance of Apolipoprotein E4 may confer this increased risk [35].

Several medical diagnoses may also increase the risk of ICH in certain patient cohorts. Unruptured cerebral aneurysms are found in roughly 3% of the population and are formed as an outpouching of an arterial wall [36]. Although many aneurysms go unruptured, they are significant risk factors for the development of a hemorrhagic stroke, and they contribute significantly towards the incidence of subarachnoid hemorrhage [37]. An example of the turbulent flow seen within an unruptured aneurysm may be seen in Figure 1-3. In addition, arteriovenous malformations (AVMs), defined as a cluster of abnormally formed blood vessels, may increase the risk of ICH in patients of all ages, but especially in children [38]. Lastly, patients on anticoagulant (blood-

thinning) medication may be at an increased risk for hemorrhagic stroke because these drugs reduce the clotting ability of the blood and make bleeding into the brain more likely [39].
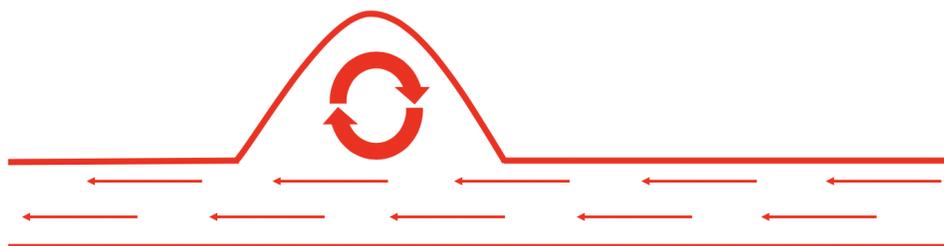
Figure 1-3. Diagram of the blood flow seen within an unruptured aneurysm.

Individuals who experience hemorrhagic stroke may present with several characteristic symptoms at the clinic. Acute onset headaches, sometimes described as "thunderclap headaches" in the context of aneurysmal subarachnoid hemorrhage, have been shown to affect roughly 92.4% of all patients with hemorrhagic stroke [40, 41]. Similarly, agitation has been described in roughly 17.4% of all patients and mydriatic pupils have been observed in 86.8% of all patients with hemorrhagic stroke [41]. In addition, the Glasgow Coma Scale (GCS) serves as a standard assessment for the level of consciousness of patients following hemorrhagic stroke, with the best possible score being 15 (oriented, following commands, eyes open spontaneously) and the worst score being 3 (no eye movement, no verbal response to painful stimuli, no motor responses) [42]. In many cases of hemorrhagic stroke, significant decline in GCS scoring is reported [43]. These drops in GCS are mostly due to the etiology of ICH in which the increased intracranial pressure (ICP) resulting from the hematoma cannot expand against the rigid skull bones, thus compressing the brain parenchyma.

Diagnosis of hemorrhagic stroke often involves clinical suspicion following the onset of symptoms. As such, patients with suspected hemorrhage may receive diagnostic imaging with MRI or CT scanning. Similar to ischemic stroke, most patients are imaged using CT scanning rather than MRI because of its high temporal resolution. An example noncontrast CT image of an ischemic stroke is seen in Figure 1-4.
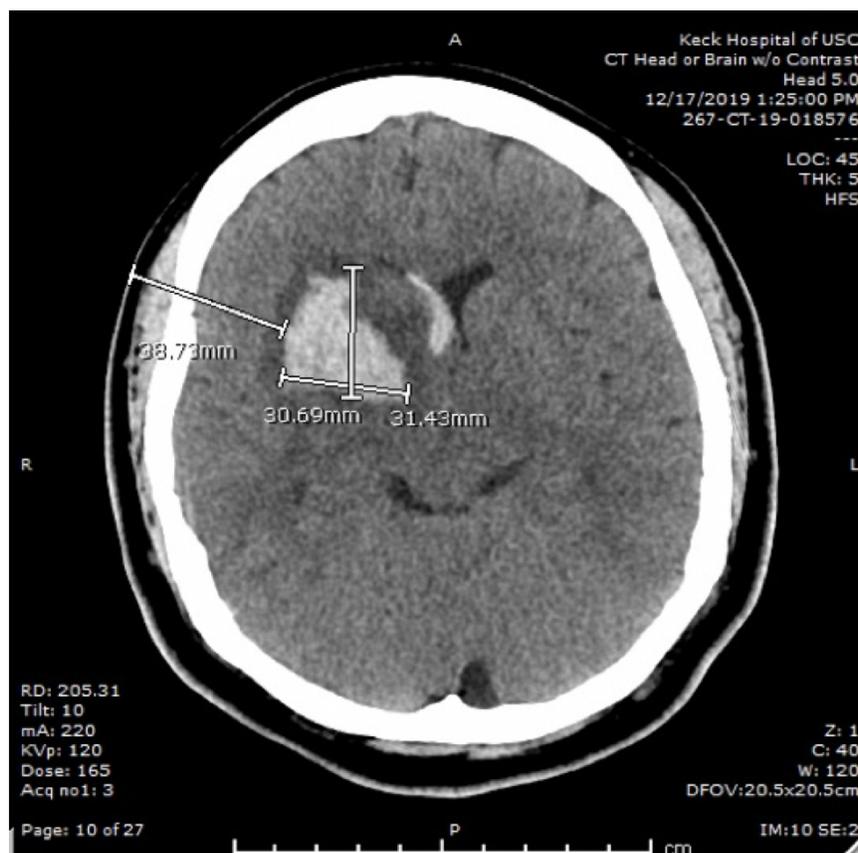
Figure 1-4. Axial representation of hemorrhagic stroke on noncontrast CT imaging

On CT imaging, ICH immediately appears as a region of hyperdensity similar to the signal generated by bone and the subtype of hemorrhagic stroke may be characterized by the location of the hematoma. Unlike ischemic stroke, ICH is visible on CT imaging immediately following the

cerebrovascular event [44]. The presence of a "spot" sign on CT imaging, which is defined as a small enhancing foci within the hematoma, has been recognized to predict hematoma enlargement [45]. Between 1 and 6 weeks, hematomas become isodense with brain parenchyma and chronic hematomas older than 6 weeks appear hypodense on CT imaging [44]. Finally, the treatment of ICH heavily depends on the size and depth of the lesion within the brain parenchyma. Many large and superficial hematomas are neurosurgical evaluated and evacuated to prevent pressure-driven brain damage in the patient. However, small (<10mL) and deep hematomas are rarely evacuated based off of established surgical recommendations [46]. Regardless of bleed size, the blood pressure of all patients is closely monitored to prevent a secondary ICH or ischemia. Stroke guidelines recommend a systolic blood pressure <160 mmHg or a mean arterial pressure (MAP) below 110 mmHg in patients following hemorrhagic stroke [47]. Obviously, hypertension is not ideal following ICH because high arterial pressures may increase the risk of a secondary bleed. Conversely, if the blood pressure is precipitously reduced, cerebral perfusion will directly decrease and there will be a risk of perihematomal ischemia at the site of the ICH [48]. As such, management of patient blood pressure following ICH is critical and necessary steps must be taken to ensure adequate blood pressure without the risk of a secondary hemorrhage or ischemia. Similarly, ICP must be managed following hemorrhagic stroke to prevent pressure-driven brain damage. Elevation of the bed to 30-degrees, sedation, osmotic diuresis (mannitol), CSF drainage via ventriculostomy, and hyperventilation may all act to reduce ICP following hemorrhagic stroke [44].

1.4 Current Stroke Diagnostic Paradigm

As previously discussed, the current stroke diagnostic paradigm relies on mostly CT imaging, and sometimes MRI imaging, to confirm the stroke subtype, location, and characteristics prior to treatment. Because patient transport to the hospital is required prior to imaging, current estimates suggest that the average time to treatment following stroke may be 2 hours because MRI/CT imaging is required prior to treatment [49–51]. In addition, neurological examination by a physician and radiologist interpretation of the head scan is required prior to treatment. On the same note, hospitals with limited imaging resources and high patient demand may not be able to immediately scan all patients with suspected stroke, further lengthening the time to diagnosis and treatment in patients based on which hospital they are transported to. During this time, the rate of neuronal death is constant, contributing to the high rates of morbidity and mortality classically seen following hemorrhagic stroke [52]. A general timeline for the diagnosis and treatment of stroke may be seen in Figure 1-5.
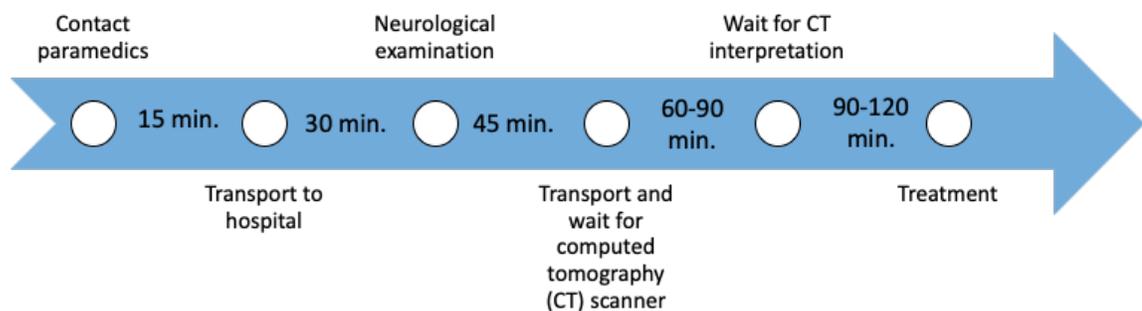
Figure 1-5. Timeline for stroke diagnosis and treatment

Furthermore, previous studies have described the disadvantages of traditional stroke imaging methods [50, 51, 53]. Namely, newer imaging procedures boast increased spatial resolution with

a hefty time cost and financial burden [53]. Furthermore, although head CT imaging produces only small amounts of radiation, exposure to radiation through CT scanning has been linked to an increased rate of cancer over long time periods [54–56]. However, in the context of a cerebrovascular emergency, the potential benefits of CT imaging to diagnose stroke definitely outweigh the potential harms associated with exposure to radiation. As such, translational medical devices that allow for rapid stroke detection without the risk of radiation continue to be investigated with hopes of increasing the safety and efficiency of stroke diagnosis.

In addition, both CT and MRI imaging devices are extremely expensive and require trained technicians to operate these machines, further adding to the expenses associated with neuroimaging. MRI machines are purchased at the cost of roughly $1.5 million US dollars, and this cost can increase significantly depending on the strength (number of Teslas) of the MRI machine [57]. CT machines cost, on average, $150,000 but may cost several million dollars depending on the capabilities of the machine [58, 59]. Furthermore, studies evaluating the economics of hospital diagnostic imaging procedures have found that CT scanning is associated with $51 in expenses and $1,565 in charges and MRI scanning is associated with $165 in expenses and $2,048 in charges per scan [60]. From this data, it is clear that diagnostic imaging in hospital systems with high patient numbers will be undeniably associated with astronomical operating costs.

As of late, the hospital system of the United States has begun investigating bundled payment systems for medical diagnoses and treatments. Within a bundled healthcare plan, a health system will receive a diagnosis-dependent lump sum once a patient is admitted, which will be drawn from

to cover the costs of diagnostic imaging, physician case, medications, etc. If the patient is discharged with little complications, the health system keeps the profits of the lump sum and distributes it accordingly to all providers who participated in taking care of the patient. However, as patients are readmitted for various complications following initial treatment, associated costs of care are deducted from the initial lump sum. As such, bundled payment systems require participant providers to assume risk and encourage health systems to treat patients as well as possible to reduce complication rates, allowing healthcare providers to maintain net profits as patients are discharged from their facilities. In the case of stroke, recent studies evaluating the CMMI BPCI have found that hospitals lose money when using the bundled payment system because stroke is associated with high rates of post-discharge complications and readmissions [4]. Thus, translational medical devices that reduce the time to treatment may reduce patient morbidity and mortality following stroke, allowing for savings within the healthcare system, increased payment to patient providers, and reduced complication rates in stroke patients.

1.5 Novel Approaches to Stroke Diagnosis

Several novel medical devices have been investigated with hopes of reducing the time to treatment in stroke care. Technologies using near-infrared spectroscopy (NIRS) to detect intracranial hematomas have been developed and have been granted Food and Drug Administration (FDA) approval as a class II device [61–63]. However, such devices are limited by the penetration of infrared waves through dense skull bone and brain parenchyma, so only bleeds located within less than 2.5cm of the brain surface may be detected [61, 62, 64, 65]. In addition, NIRS devices are unable to probe for cerebral ischemia and thus may not be able to differentiate strokes by subtype.

Furthermore, current devices only have the capacity to probe four areas on each hemisphere of the brain for hematomas and are unable to support continuous scanning and imaging [61, 62, 64, 65]. The ECD sensor described in this study demonstrates several advantages compared to NIRS technology, which is shown in Table 1-1.

Features	ECD Sensor	MRI	CT	Infrascanner(NIR)
No Radiation	✔	✔		✔
Fast	✔			✔
Produces an Image	✔	✔	✔	
Compact	✔			✔
Cost	✔			

Table 1-1. Advantages of ECD sensor compared to similar modalities

Similarly, a device using volumetric impedance phase shift spectroscopy (VIPS) to detect large vessel occlusion and hemorrhage have also been granted FDA approval as a class II device [62]. While such a device shows promise in stroke classification, it still does not allow for image production and does not afford an affordable alternative to traditional diagnostic imaging. Another approach that has been investigated is the use of microwave-based detection of stroke [66]. While this approach boasts similar accuracy as VIPS, it has several limitations, one of which being that such devices do not support continuous scanning but rather scan several points within the brain [67]. As such, it is possible that small strokes that do not align with the sensor array may go unnoticed.

Furthermore, previous studies have explored blood-based detection of stroke through the use of RNA and protein biomarkers. Protein biomarkers that may suggest the presence of an ischemic stroke include S100 calcium binding protein B (S-100B), neuron-specific enolase (NSE), myelin basic protein (MBP), and glial fibrillary acidic protein (GFAP)[68]. In addition, nonspecific protein biomarkers of inflammation have been explored as biomarkers of ischemic stroke, including C-reactive protein (CRP), interleukin-6 (IL-6), tissue necrosis factor-alpha (TNF-α), vascular cell adhesion protein 1 (VCAM 1), intercellular adhesion molecule 1 (ICAM 1), N-methyl-d-aspartate (NMDA) receptor antibodies and matrix metalloproteinases (MMPs), D-Dimer, and von-Willebrand factor (vWF)[68]. RNA biomarkers of ischemic stroke focus on the variations in gene expression within cells of the peripheral circulation following ischemic stroke, seizures, hypoglycemia, and hypoxia [69]. While many of these protein biomarkers show promise in detecting ischemic stroke, the current standard of care still emphasizes diagnostic imaging because many of these biomarkers are nonspecific to stroke and may be elevated following traumatic brain injury (TBI) or systemic illness. In addition, visualization of the stroke is necessary prior to treatment in order to ensure proper treatment. Because ischemic strokes are often treated with EVT and hemorrhagic strokes are often treated with neurosurgical evacuation, accurate localization of the ischemic or hemorrhagic lesion is necessary to guide timely medical intervention. As such, diagnostic imaging continues to be the current standard of care.

Lastly, there has been a large push towards developing mobile CT and MRI imaging devices to facilitate in-hospital stroke triage as well as mobile ambulances with diagnostic imaging modalities on board. Mobile CT imaging devices have been adopted by a number of hospitals to facilitate diagnostic imaging without the need for patient transport. Although these devices may reduce the

time to diagnosis, they have the same limitations of CT machines and use radiation, incur operating costs, and are expensive to purchase. In addition to these limitations, mobile CT imaging devices have additional limitations including a limited range of technique protocols (fixed 120 kV), helical pitch (fixed 1.4), and the need to select reconstruction filters prior to the scan (without opportunity to re-reconstruct with a different filter) [70]. Similar portable MRI devices have been demonstrated on benchtop extensively but continue to be much more difficult to develop as a portable or mobile device because of the high sensitivity to surrounding magnetic noise and the large magnetic field that must be generated prior to diagnostic imaging [71].

Although many creative solutions have been developed to reduce the time to treatment and diagnosis in stroke patients, further experimentation, methodologies, and novel medical devices are warranted to develop a solution with minimal limitations. No doubt, cheap and portable translational medical devices capable of detecting stroke, differentiating stroke subtypes, producing an image, and providing information on the depth/volume of the lesion may play a large role in facilitating stroke diagnosis and treatment.

1.6 Conclusion

The high metabolic demand of the brain makes it particularly susceptible to injury. Stroke, including both ischemic and hemorrhagic subtypes, continue to represent a large cause of mortality within the United States and globally. One factor that continues to contribute towards the high morbidity and mortality of stroke is the long time to treatment experienced by many stroke patients. Therefore, novel translational medical devices capable of reducing this time to treatment may facilitate stroke diagnosis and treatment with hopes of reducing the degree of acute brain injury.

Current work evaluating novel diagnostic strategies for stroke have proposed several creative approaches, including the use of VIPS, NIRS, microwave-based diagnosis, and blood-based biomarker assays to diagnose and classify stroke. However, none of these novel techniques allow for stroke visualization, and many of these approaches lack the granularity required to diagnose stroke prior to treatment. In addition, many of these novel approaches are associated with significant costs to the patient, further limiting widespread use.

As such, cheap, portable, and rapid stroke diagnosis and classification devices would allow for rapid patient diagnosis, triage, and treatment. This thesis will discuss an ECD sensor capable of producing high-fidelity stroke localization and diagnosis with hopes of reducing the time to treatment.

CHAPTER 2: SENSOR PRINCIPLES & DEVELOPMENT

2.1 Introduction

Sensors detect, measure, and record the physical properties of a target, and modern sensor advancements have introduced sensing devices in virtually every setting including hospitals. In the case of the stroke sensor described in this thesis, conductivity is the physical property of interest and relevant circuitry must be designed in such a way to maximize signal generation. As such, the purpose of this chapter is to discuss the physics underlying the eddy current damping sensor, considerations to increase the signal-to-noise ratio (SNR), circuit architecture, and future circuit considerations to improve sensing capabilities.

2.2 Background of Eddy Current Damping

The magnetic field generated by the inductor produces an electromotive force (EMF) that creates a looping 'eddy' current in the conductive material described through Ohm's law:

$$\vec{J} = \sigma \vec{E}$$

where $\vec{J}$ is the current density, σ is the conductivity, and $\vec{E}$ is the electric field. When a conductor is in close proximity with such a time-varying magnetic field, eddy currents are generated within the conductive material. In accordance with Lenz's Law, the looping eddy currents are in the direction opposite to the magnetic field, thus creating a repulsive force.

The unique electromagnetic properties associated with ECD have resulted in several precedent devices, primarily used for industrial applications. ECD automobile braking systems have been developed that utilize the counteracting magnetic fields generated within the conductive target to slow vehicles. The advantages of ECD braking include, but are not limited to, contactless implementation, rapid response, small number of parts, and easy implementation of controllers [72]. Similarly, the reliability of the ECD phenomenon has also seen its use in automobile suspension systems, roller coaster braking, and elevator braking [73–76].

Furthermore, nondestructive testing (NDT) has historically been utilized in the inspection and diagnosis of cracks and corrosion in the aerospace industry [77]. The current paradigm of airplane inspection involves NDT eddy current testing of aircraft wheels, fuselage, and layered structures with inductive sensors similar to the one described in this thesis for stroke sensing. Additionally, contemporary evidence suggests that arrays of ECD sensors may be implemented to detect cracks in aircraft tubes with millimeter resolution and a tolerance of ±20% [78].

2.3 ECD Sensor Circuit

The ECD sensor equivalent circuit model consists of a sensor coil paired with a capacitor to form an electrical resonant circuit, which is significantly from the architecture of previous ECD sensors used in industry for metal detection and crack inspection consisting of a bridge circuit that measures the sensor coil impedance [79, 80]. Thus, the sensor operates as a coil carrying an alternating current (AC), which produces a time-varying magnetic field in accordance to Faraday's Law:

$$\nabla \times \vec{E} = \frac{\partial \vec{B}}{\partial t}$$

where ∇ is the curl operator, $\vec{E}$ is the electric field as a function of position and time, and $\vec{B}$ is the magnetic field as a function of position and time. This resonant circuit, or LC tank, may then experience a change in resonant frequency (Rf) and coil impedance following the introduction of materials with varying conductivity profiles into the coil sensor's magnetic field. The circuit used to record ECD signals consists of a capacitor in parallel with an inductor which can be seen in Figure 2-1.
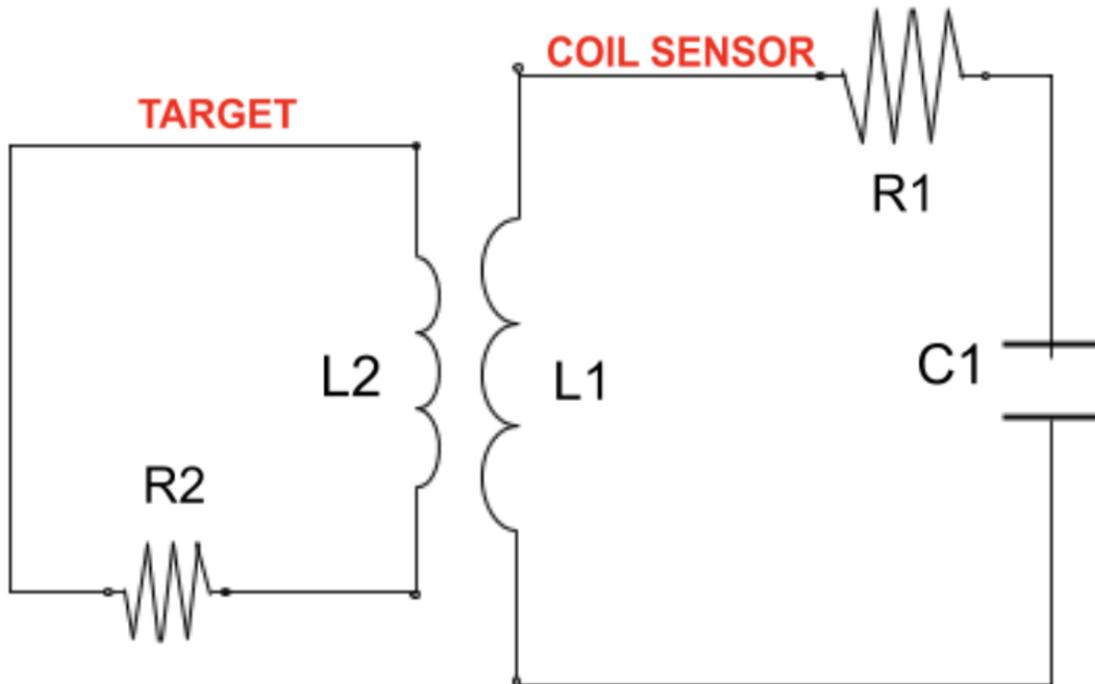
Figure 2-1. Sensor circuit

As seen in the figure above, L1 represents the inductance of the sensor, C1 represents the capacitor paired with the inductor to form an LC tank, and R1 represents the internal resistance of the coil sensor. Similarly, L2 represents the inductance of the target and R2 represents the resistance associated with the target. Placing the coil sensor in proximity with the target generated coupling between L1 and L2, resulting in the characteristics changes in inductance and Rf measured by the circuit.

2.4 ECD Sensor Physics

When eddy currents are produced within the coil sensor, they generally flow in a manner that increases coil resistance and decreases coil inductance, a change that may be measured through

the use of a precise frequency counter. As eddy currents are generated within our coils, we use the Texas Instruments LDC 1101 chip to convert signals from our coils into computer readout [81]. Each coil was connected to its own LDC 1101 chip, and sensor outputs were recorded in series from each chip and stored on a local computer for analysis.

In accordance with the previous theory, when a conductive target is placed in proximity with the coil sensor, the generation of eddy currents in the target will produce a counteracting magnetic field that will decrease coil inductance and increase coil resistance. Conversely, when a nonconductive target is placed in proximity with the coil sensor, the counteracting magnetic field may increase coil inductance and decrease coil resistance compared to baseline values. As such, it is theoretically possible to obtain unique, proximity-dependent electrical signals based off of the subtype of stroke present in the patient.

Additionally, the EMF generated by the counteracting magnetic fields in the target hinder current flow within the coil sensor and increase the resulting AC resistance. This phenomenon is described by the equation:

$$R_p = \frac{L}{RC}$$

where R_p is the parallel resistance, L is the inductance, R is the resistance, and C is the capacitance. As seen in the equation, the parallel resistance of the electrical circuit is inversely related to the coil's AC resistance. Thus, external targets that lower coil resistance will increase R_p, while targets that increase resistance will decrease R_p.

Any changes in coil resistance can be quantified by using a precise power meter to measure the power dissipation in the coil. Assuming the skull can be modeled as a flat, two-layer structure, then the coil's AC resistance is related to the tissue conductivity implicitly and can be modeled by a set of analytical solutions described by Dodd and Deeds [82]. The LDC integrated circuit (IC) chip provided heterodyne downshifting utilization to achieve higher frequency readout than the ~40 samples per second [81]. It was possible to achieve even higher sampling rates (>200 samples per second) by downshifting the coil voltage to a lower frequency (~1kHz) through the use of a frequency mixer. This signal could then be sampled by an analog-to-digital converter, bandpass-filtered, and conditioned by digital signal processing to recover the original resonant frequency.

2.5 Stroke Sensor Manufacturing

At first, individual coils of different sizes were constructed using plastic cylinders of varying sizes as scaffolds, with 46 AWG Litz wires with a diameter of 0.7cm wrapped around them to create solenoid coils. In our experiment, we constructed three solenoid coils with varying diameters and number of turns with the largest coil having an outer diameter of 11.4cm and 6 turns, the middle having an outer diameter of 4.5cm and 15 turns, and the smallest having an outer diameter of 1.5cm and 35 turns. The magnetic field of a solenoid can be derived from Biot-Savart's Law, yielding the following equation:

$$B = \frac{\mu_0 N I r^2}{2(x^2 + r^2)^{\frac{3}{2}}}$$

where r is the radius of the solenoid, I is the current in the solenoid, μ_0 is the absolute permeability of free space, x is the distance of the target from the center of the coil, and N is the number of turns in the coil. The use of the Litz wires minimized the coil resistance, and the varying diameters and number of turns allowed increasing magnetic field penetration depth from the smallest to largest coil, with turn number N directly proportional to the length and diameter of the coil [83]. In addition, Litz wire minimized the potential for capacitive coupling between different coils. Each of the three coils was circumferentially wrapped with ferrite sheets with the aim of redirecting the magnetic field distribution toward the target and blocking the electromagnetic interference from external sources. The average relative permeability of the ferrite sheet (MULL12060-000, Laird Technologies Inc.) is approximately 135 from 1MHz to 10MHz, which encapsulates the frequency range used in this study [84]. Data was recorded and saved to a computer using a wired USB connection with a maximum possible current of 0.0027 Amperes. Photographed and computer rendered images of the coil sensor may be seen below in Figure 2-2, 2-3, 2-4, and 2-5.
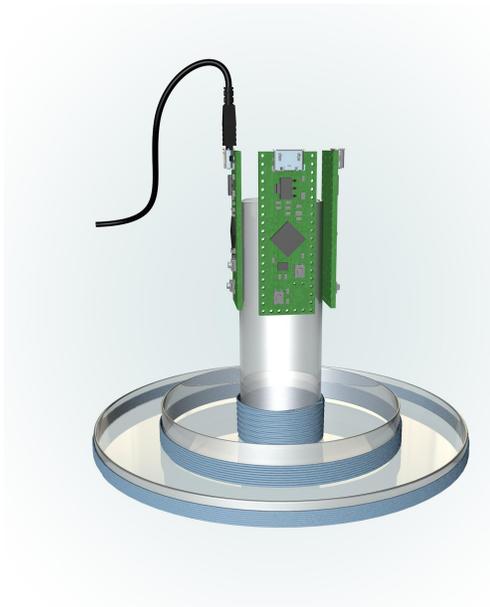
Figure 2-2: Computer rendering of the assembled sensor.
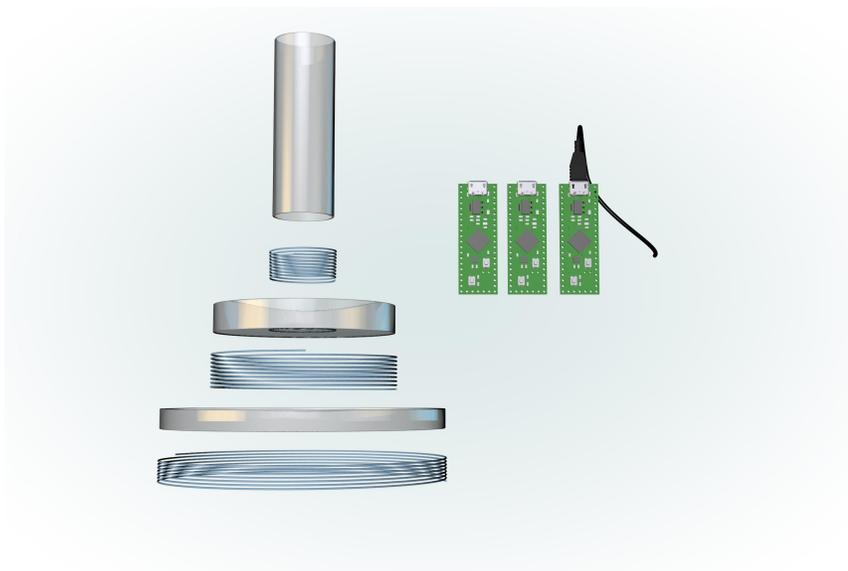
Figure 2-3: Computer rendering of disassembled sensor.
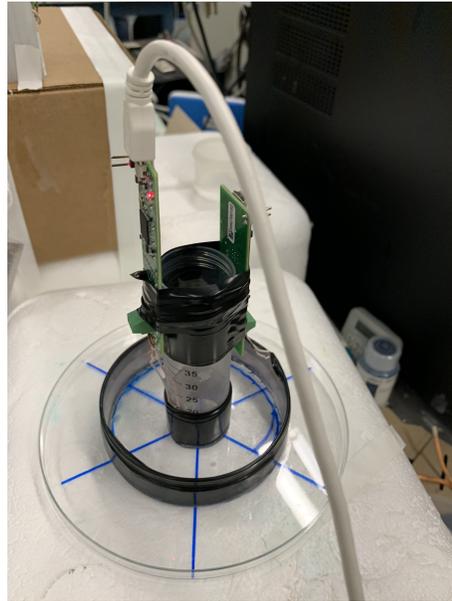
Figure 2-4: Assembled sensor in a laboratory setting.
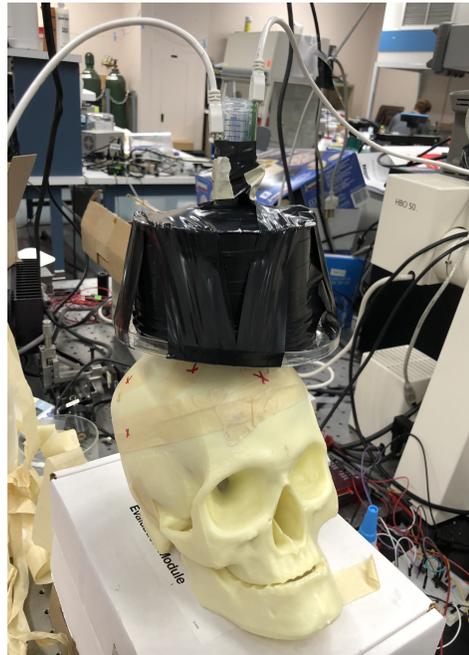
Figure 2-5: Assembled sensor on a plastic skull replica.

2.6 Sensor Heating

Electrical circuits are not perfect at utilizing energy and often emit heat radiation as they operate. The temperature of the circuit often varies as a function of several variables, of which the most important is the operating time of the sensor. Overheating of a sensor may lead to significant disturbances of the sensor output, since heating a metal conductor makes it more difficult for electricity to flow through it. This phenomenon may lead to incorrect resistance and inductance reading that would undoubtedly risk stroke misdiagnosis.

To evaluate whether circuit heating may play a significant effect in sensor operations, we evaluate the specific heat equation which states:

$$Q = mc\Delta T$$

where Q is the specific heat, m is the mass of the material, c is the specific heat of the material, and ΔT is the change in temperature. Plugging in pertinent values for the sensor we get:

$$Q = (50g)(0.385 \ \frac{J}{g * °C})(1°C) = 19.25J$$

As such, we find that 19.25J are required for a temperature change of $1°C$ within our coil sensor. We then combine the preceding equation with equation for electric power which states:

$$P = IV$$

where P is the power in Watts, I is the current, and V is the voltage. Plugging in pertinent values for our sensor we get:

$$P = (0.0027A)(2.6V) = 0.00702 \ \frac{J}{s}$$

Lastly, to solve for the time required to induce a *1℃* within our coil sensor based off of its unique power requirements, we can divide Q by P:

$$t = \frac{Q}{P} = \frac{19.25J}{0.00702 \, \frac{J}{s}} = 2,742.17s$$

Thus, we find that the time required to induce a *1℃* within our coil sensor is 2,742.17 seconds (45.70 minutes). Because the time required to scan patients with the sensor is on the order of several minutes and coils are turned on and off one-by-one in series for testing and scanning, it is highly unlikely that coil heating and related temperature fluctuations play a role in sensor noise and output. Likely, the noise produced as a function of heating in such a coil sensor is negligible.

2.7 Guide Rails for Scanning

In order to achieve accurate location-dependent scanning, guide rails for stroke sensor scanning were developed. On benchtop skull experimentation, a set of eight plastic tubes were arranged horizontally on the skull starting at the forehead and ending at the occiput. All eight rows were equidistant, and a plastic silicone attachment was fastened onto the bottom of the sensor to allow for movement along the plastic tube. These guide rails are visualized on benchtop models in Figure 2-6, 2-7, 2-8, and 2-9.
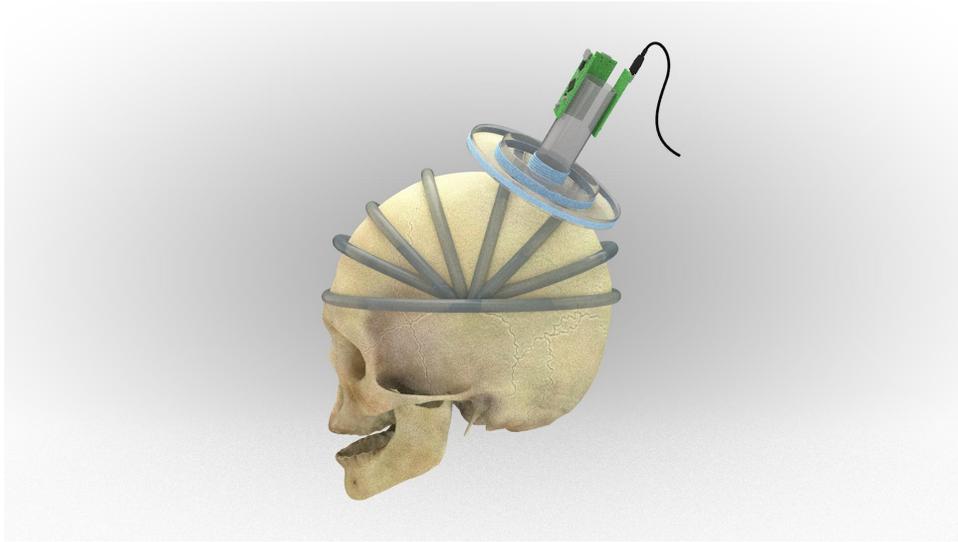
Figure 2-6: Computer model of benchtop skull and guide rails.
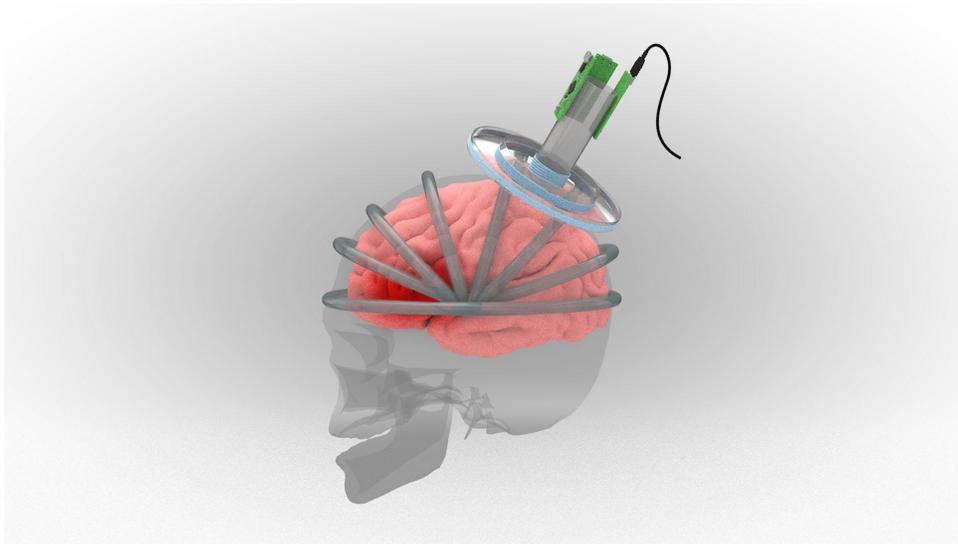
Figure 2-7: Opaque computer model of benchtop skull and guide rails.

Figure 2-8: Benchtop skull model and guide rails.
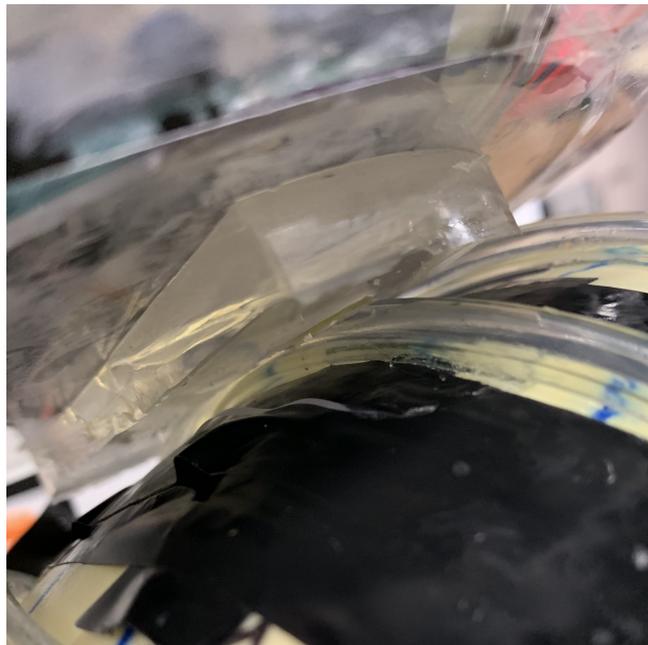
Figure 2-9: Interaction between silicone groove on sensor with guide rail.

Similarly, to accommodate cadaveric and live human scanning with the sensor, the guide rails were translated onto a wearable hat device that 1) prevented direct patient contact with the sensor device, allowing for hygienic scanning of multiple patients and 2) allowed for patient specific adjustments based off of individual head shape and size. These advantages allowed for a quick setup and scanning environment that could be portable and deliverable at a patient's bedside. The portable hat sensor is illustrated in Figure 2-10.

Figure 2-10: Wearable hat setup for stroke sensor scanning.

The purple cushion seen below the chin in Figure 2-10 prevents compression of the patient's neck by the plastic tubing, ensuring that the experimental setup is comfortable for the patient. In

addition, to minimize friction when maneuvering the stroke sensor with silicon base across the plastic guide rails, WD-40 lubricant spray was occasionally applied. This low conductivity synthetic lubricant allowed for improved sensor hand scanning and significantly reduced the time required for patient scanning as well as the margin for error due to movement or the sensor being stuck.

2.8 LDC 1101 Signal-To-Noise

SNR is defined as the ratio of signal obtained by the sensor to that of the noise inherently present within the sensor output. As such, sensors with high SNR are preferred because they can accurately ascertain signal from noise, ensuring the validity of the sensor output for clinical decision making.

All three coils of the stroke sensor were found to resonate at around 1MHz, and the SNR was calculated for each sensor using the LDC 1101 chip. This was done by dividing the magnitude of the coil's signal by the standard deviation over several thousand time points. The small coil was found to have an SNR of 9.34, the medium coil was found to have an SNR of 8.81, and the large coil was found to have an SNR of 7.92. The average SNR for all three coils was 8.69. The trends in SNR as a function of coil diameter may be seen in Figure 2-11 below.
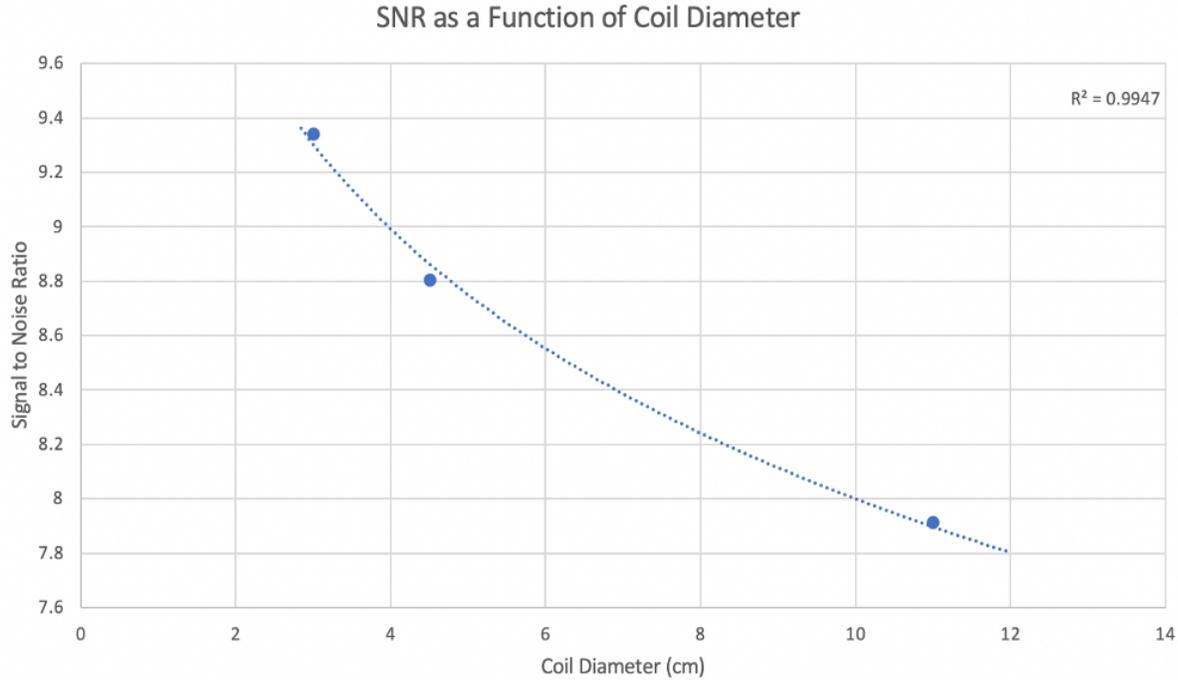
Figure 2-11: SNR as a function of coil diameter.

The SNRs generated for each coil are adequate in distinguishing signals from noise. However, further investigation was required to investigate the sources of noise within the sensor. After trying different types of wire, including wire of different diameters, strand numbers, and orientations, SNR was not found to vary. In addition, Section 2.6 demonstrated that noise was also not likely due to overheating of the sensor during its operational phase. As such, we hypothesized that much of the noise within the sensor may be a result of the limitations of the LDC 1101 chip itself. Because this is a commercial chip, we were unable to modify the circuit during its development phase to fully understand its potential sources of internal noise. As such, we developed an LC tank capable of detecting conductivity changes.

In addition, noise-equivalent distance and volume were explored for the sensors. Noise-equivalence distance/volume is defined as the distance/volume at which the SNR is equal to 1.00.

As described previously, the ECD signals generated within the sensors are a function of both conductivity and distance. Resultantly, both of these factors are important to be considered when calculating noise-equivalence. The noise-equivalent distance in the small coil was 5.1cm for volumes between 20 and 50mL, that for the medium coil was 4.7cm for volumes between 20 and 50mL, and that for the large coil was 9.6cm for volumes between 20 and 50mL. A result of the raw data is shown in Table 1-1.

Noise Equivalent Volume and Distance			
Volume	Distance -1.5cm Coil	Distance - 4.5cm Coil	Distance - 11.4cm Coil
20mL	5.4286cm	4.7673cm	9.7143cm
30mL	5.0069cm	3.8940cm	9.5760cm
40mL	5.0207cm	5.0783cm	9.3641cm
50mL	4.8134cm	5.0853cm	9.7235cm

Table 1-1: Noise-equivalent volume and distance

2.9 Developing an LC Tank

To develop the LC tank, 46 AWG Litz wire was wound around a hollow plastic cylinder with an internal diameter of 11.4cm 6 times to create an inductor. The inductance of the coil was found to be 11.02 μH. To determine the capacitance required to generate resonance at 1MHz, the following equation was utilized:

$$Rf = \frac{1}{2\pi\sqrt{LC}}$$

Plugging in relevant values from our inductor, we get:

$$1 * 10^6 Hz = \frac{1}{2\pi\sqrt{(11.02\ \mu H)C}} \Rightarrow C = 2.3nF$$

As such, a 2.3nF capacitor was connected in parallel with the inductor to create an LC tank. To determine the coil's quality factor (Q), an oscilloscope was connected in parallel with the LC tank, as seen in Figure 2-12.
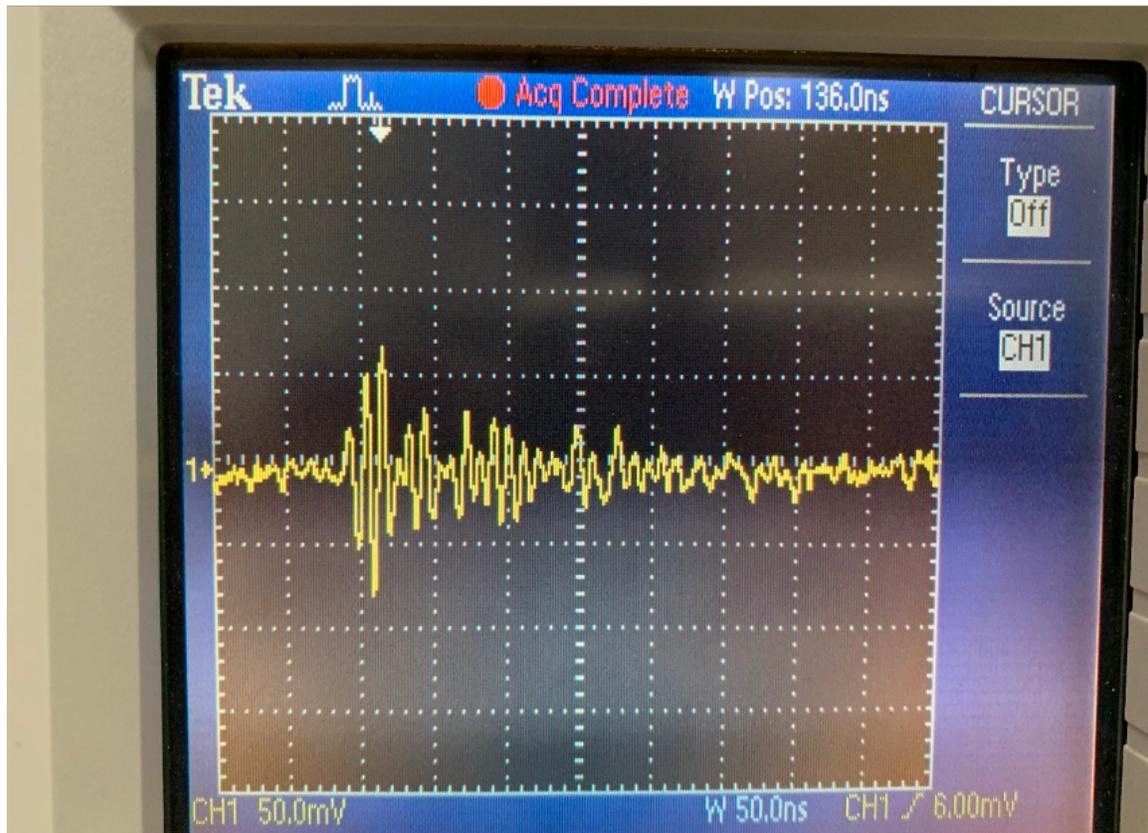
Figure 2-12: Oscilloscope output for the LC tank.

The approximation of Q in such a setting is the product of 2π and the number of oscillations seen on the oscilloscope output. Because the oscilloscope shows 24 oscillations, the approximate Q for this sensor is 150, which is relatively high and appropriate for lesion detection.

Through combining several points of theory regarding the physics underlying the LC tank, it was possible to devise an apparatus capable of quantifying changes in Rf due to local conductivity changes while preserving Q. The first point stems from the definition of Rf, which states that at Rf inductive reactance (XL) is equivalent to capacitive reactance (XC). Thus, at Rf impedance simplifies to:

$$(Z) = \sqrt{R^2 + (X_L - X_C)^2} = \sqrt{R^2} = R$$

In accordance with the above equation, when the Rf is achieved the circuit is able to absorb and/or dissipate the maximum amount of energy. As a result, the current (I) is maximum at Rf. Lastly, the following equation describes the final piece necessary to devise our experimental setup:

$$V_L = I_L x Z_L$$

where V_L is the voltage of the inductor, I_L is the current of the inductor, and Z_L is the impedance of the inductor. Since current reaches a maximum at Rf, we expect voltage to also reach a maximum at Rf.

Thus, the experimental setup involved the LC tank, a precise frequency counter, an oscilloscope, and a function generator. All components were wired in parallel directly to the LC tank to reduce stray capacitance/inductance and to maximize Q. A sine wave was generated by the function generator, and as the function generator frequency changed, so did the voltage output on the oscilloscope screen. To achieve Rf, the function generator frequency was tuned until the sine wave shown on the oscilloscope screen reached a global maximum. This frequency was then recorded as the Rf of the coil, and this value changed as the conductivity of local objects changed. More conductive materials were hypothesized to increase the Rf, and less conductive materials were hypothesized to decrease the Rf.

To calculate the SNR of the LC tank, a Fast Fourier Transform (FFT) was taken of the oscilloscope output. This output is seen below in Figure 2-13.
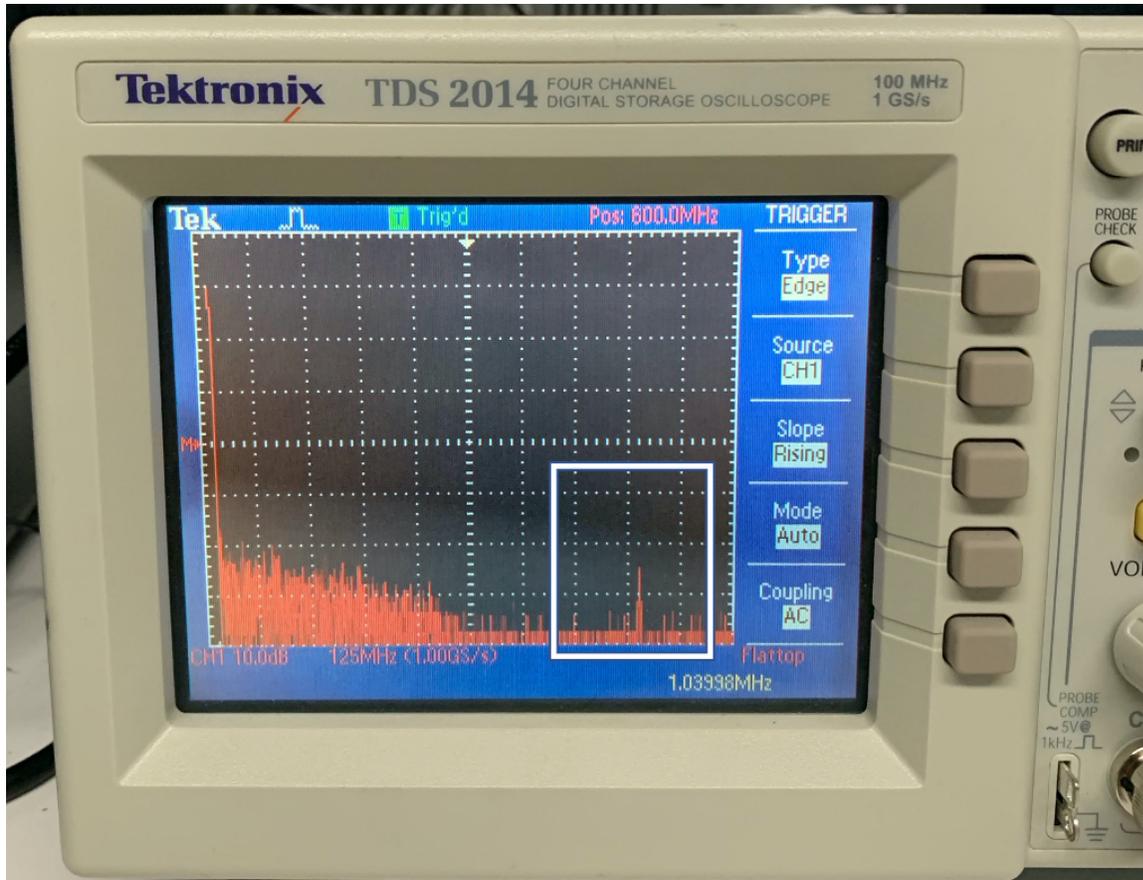
Figure 2-13: FFT of oscilloscope signal.

Taking into account the noise floor and signal amplitude of the FFT signal, the approximate SNR of the LC tank is 14, which marks a small but significant increase from the SNRs of the coils paired with LDC 1101 circuits. This finding suggests that the internal resistance of the LDC 1101 circuit may play a role in reducing the SNR of the sensor, and the future sensor iterations that rely on custom circuits with low internal noise may be even better at detecting intracranial lesions.

2.10 Similar Stroke Devices

Advances in diagnostic technologies that can quickly and non-invasively detect brain hemorrhages would streamline stroke management and reduce delays to diagnosis and treatment in the hospital setting. Technologies using NIRS to detect intracranial hematomas, VIPS to detect large vessel occlusion and hemorrhage, and blood tests and microwaves to classify strokes have been developed, with some achieving FDA approval as a class II device [61–63]. However, such devices are limited by the penetration of infrared and radio waves through dense skull bone and brain parenchyma, and thresholds exist with regard to the size and distance of lesions capable of being detected by this technology [61, 62, 64, 65]. Furthermore, current devices are incapable of producing images of the brain and corresponding lesions following scanning [61, 62, 64, 65]. Furthermore, NIRS technology is severely limited by the depth of penetration of infrared light, limiting scanning to the most superficial 2.5cm of the brain.

The physical properties of ECD sensors described in this chapter make them uniquely capable of avoiding many of the limitations imposed by previous stroke sensors. In addition, the lack of radiation and low magnetic field utilized by the ECD sensor allow it to scan, image, and predict stroke subtype accurately, safely, and efficiently.

2.11 Conclusion

Overall, sensor analysis and optimization are critical parts of medical device development. The stringent requirements of the United States FDA require sound medical device theory in conjunction with experimental evidence, which will be outlined in the next few chapters.

Specifically, medical sensors that are developed for neurocritical conditions, including but not limited to hemorrhagic and ischemic strokes, must demonstrate a high level of accuracy, sensitivity, and specificity to prevent mistakes. While false positives may waste medical provider

time and energy in rushing healthy patients to the emergency room, false negatives are absolutely contraindicated and may make the difference between life and death. This is why SNR must be optimized, to ensure that the signal generated by a hemorrhage or area of ischemia always outweighs the local noise generated through coil operation and environmental factors.

To further increase SNR in future iterations of the stroke sensor, avenues of coil automatization must be explored. Currently, the coil is scanned across the eight rows by hand. Hand scanning, although at times sufficient, is not the optimal setup in such a device because discrepancies between operators may result in additional noise within the sensor output. In addition, any jewelry worn by the scanner including bracelets and watches may further add to the noise of the sensor recordings and diminish the signal generated by the lesion.

CHAPTER 3: BENCHTOP EXPERIMENTATION

3.1 Introduction

As mentioned in previous chapters, the goal of this project is to develop a handheld ECD sensor for rapid stroke detection, localization, and classification. However, in order to establish the basic principles of the ECD sensor, several key benchtop experiments were performed. As such, these experiments were necessary to first establish the safety and feasibility of the sensor prior to translating the device to more complicated models.

First, the theoretical limits of the ECD sensor were explored. These included the range of detection, volume sensitivity, and postprocessing requirements. Next, the finalized ECD sensor was explored on benchtop stroke models. Through these experiments, scanning protocols were determined and software was developed to accurately represent the lesions as a two-dimensional image. Lastly, circuit optimization was explored to investigate the maximum SNR possible with such a sensor.

While the true translational potential of the ECD sensor will be explored in later chapters, a background of the benchtop experiment results is critical in fully assessing the potential of ECD scanning in stroke care.

3.2 Sensitivity to Distance

We moved spherical saline-filled balloons of various volumes at a constant rate towards the large, medium, and small coils, and we were able to discern when a signal was detected with

the threshold signal being defined as 10% of the change from baseline to endpoint. Since increasing coil sizes and turn numbers intrinsically correlate with increasing magnetic field strength, we created tuning curves for each coil. In order to minimize capacitive coupling and reduce the noise of our sensor, we covered each sensor with ferrite sheets, leaving the end facing the target unshielded. The use of magnetic shielding with ferrite material helped to redirect the magnetic field distribution toward the target and block the electromagnetic interference from external sources.

Movement at a constant rate was achieved by fixing the balloon to a syringe pump with plastic rods, such that both the balloon and sensor were far from any metal. The syringe pump was pre-programmed to move the balloon at 0.503 mL per minute towards the sensor. Data was recorded and stored on a local computer during the duration of the experiment until the balloon touched the surface of the stational ECD sensor. The experimental setup may be seen in Figure 3-1.
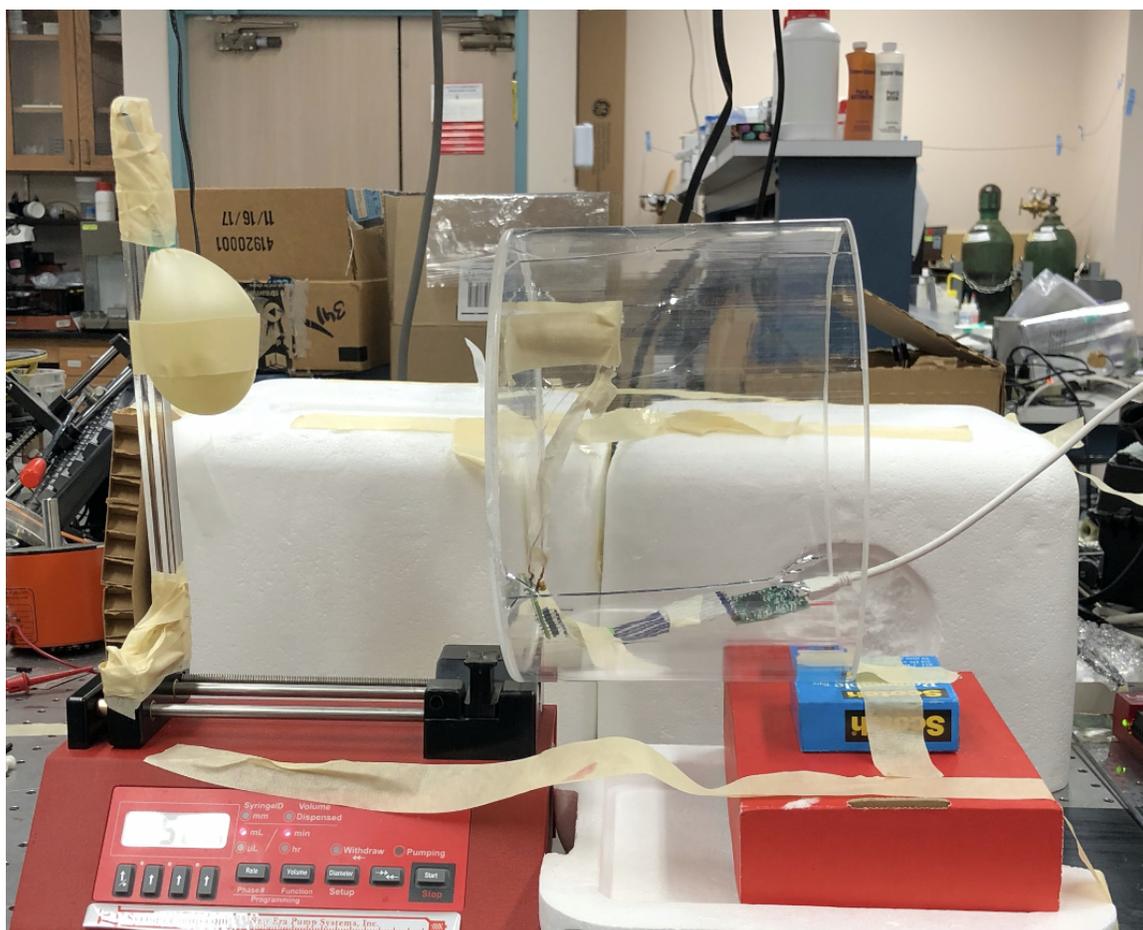
Figure 3-1: Tuning curve experimental setup.

The most prominent tuning curve generated for the ECD sensor involved a 50mL spherical

balloon, and correlated changes in distance with changes in resistance values ($\frac{\Delta R}{R}$). Analysis of the

tuning curves demonstrated that the large coil had the largest range of detection (4.97cm), followed

by the medium sized coil (3.99cm), and lastly the small coil (2.29cm). Per the physics of ECD

described in Chapter 2, it makes sense that the largest coil had the greatest scanning depth, and the

smallest coil had the smallest scanning depth (Figure 3-2).
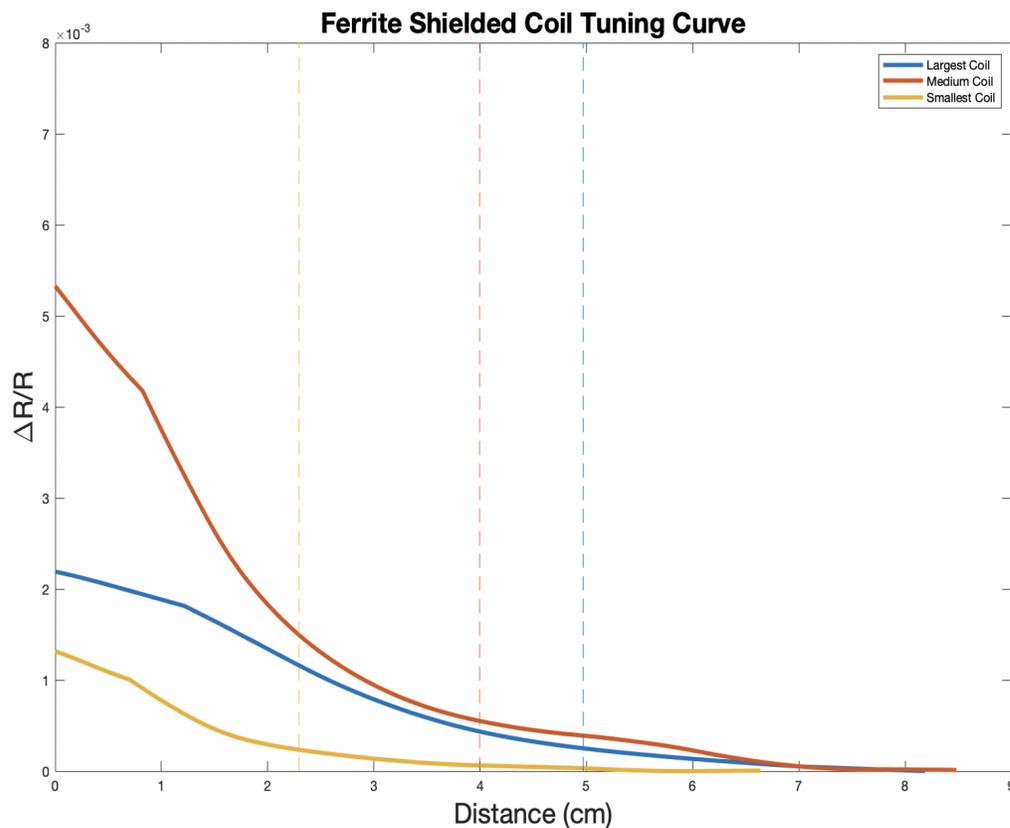
Figure 3-2: Distance tuning curve for ECD sensor.

3.3 Sensitivity to Volume

Furthermore, balloons of different volumes were used to create volume-dependent tuning curves (Figure 3-3). As seen in these curves, the coil sensors have a reproducible volume-dependent resistance change, with larger and more conductive lesions eliciting an increased resistance change and smaller and less conductive lesions eliciting a decreased resistance change. Thus, we can use these tuning curves to approximate the depth and volume of a signal-producing lesion by understanding which coils are able to detect a signal in series coil measurements. It then

follows that a multi-coiled sensor design may not only be able to localize lesions, but it also may

provide important clinical information about the depth of the lesion within the brain.
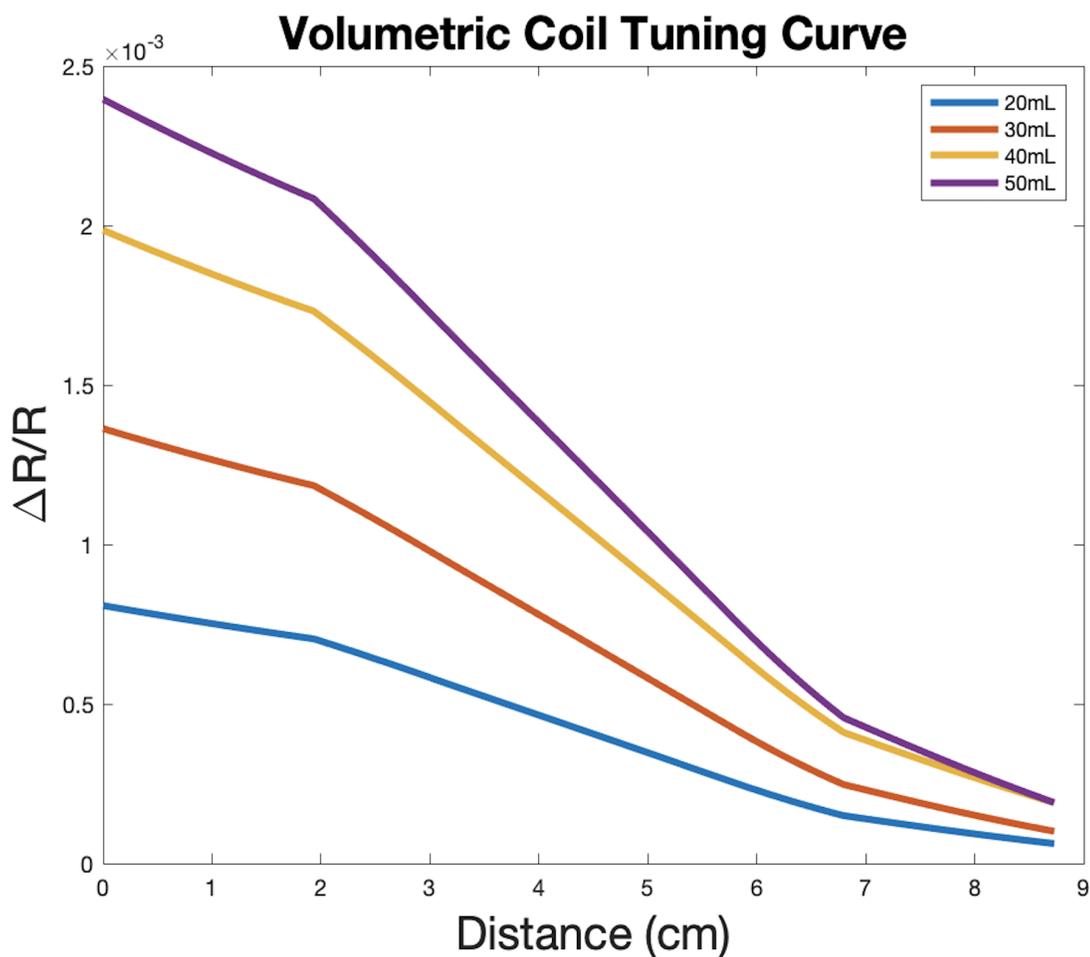
Figure 3-3: Volumetric tuning curve for 3cm ECD sensor.

In addition, the volume tuning curve shown above successfully demonstrates that ECD

signals generated within the model are directly proportional to the size of the lesion, further

bolstering the claim that more conductive lesions (hemorrhagic stroke) may be easily differentiated

from less conductive areas of ischemia (ischemic stroke). Because these changes in volume reflect relative increases or decreases based on the baseline conductivity values of normal control human adult brain, we hypothesized that differential scanning may be necessary to fully interpret point-by-point conductivity values.

3.4 Sensitivity to Shape

To investigate whether the shape of the hemorrhage or infarct may influence the sensitivity at which the ECD operates, we compared signal changes between utilizing a classic spherical saline-filled balloon and a disk-shaped saline-filled whoopie cushion. Small, medium, and large coils were then positioned, and either the spherical or disk-shaped balloon was moved towards the coil. Parallel resistance was recording for balloons of different sizes, including 20mL, 30mL, and 40mL. The signals generated by either balloon subtype were then plotted together for each coil, and the resulting tuning curves may be seen in Figure 3-4.
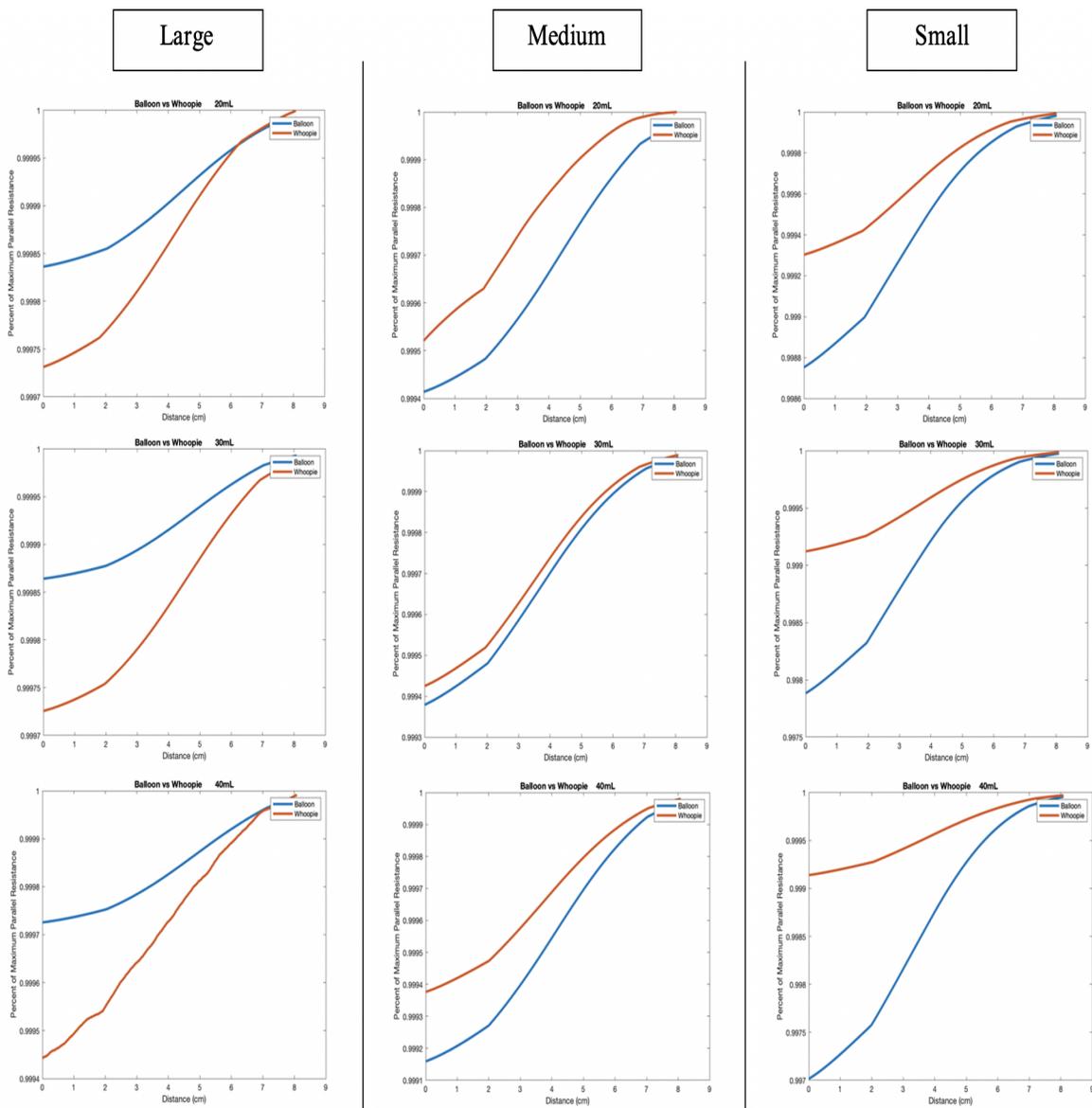
Figure 3-4: Shape tuning curve for three ECD sensors.

As seen in the curves above, the shape of the lesion may result in reproducible changes in R_p. In all graphs, blue lines represent a spherical balloon and red lines represent a disk-shaped whoopie cushion. Namely, our benchtop experiments suggest that the small and medium coils may be more sensitive to lesions that are more spherical in shape, and that the large coil may be more sensitive to lesions that are disk-shaped. Because ICH may present heterogeneously, with well circumscribed lesions having a spherical shape and epidural lesions having more of a disk/egg shape, it is important to understand which lesion types may be detected most accurately. Importantly, all three coils are sensitive to lesions of both shapes, though one shape prevails over the other. It then follows that series coil measurements with all three coils may allow for the most accurate lesion detection.

3.5 Saline Vs Deionized Water

To confirm that a more conductive saline target yields a greater degree of ECD signals compared to non-conductive deionized (DI) water, several experiments were developed for each sensor. The first of the experiments involved letting the sensor run for several seconds, then placing a bottle of either DI water or 0.9% saline directly in front of the sensors. The second experiments involved placing a saline-filled balloon on a non-conductive surface, and scanning across the surface starting one foot away from the balloon, directly over the balloon, the one foot in the other direction on the non-conductive surface. The third experiment was the most complex and involved placing an inflatable balloon inside a bath of 0.09% saline solution. The balloon was inflated with 0.9% saline solution twice in each experiment. The y-axis for all graphs was in the units of R_p and the x-axis unit was time as a function of the sensors' sampling rate. The results of all three

experiments are shown for the large, medium, and small coils in Figure 3-5, 3-6, and 3-7 respectively.
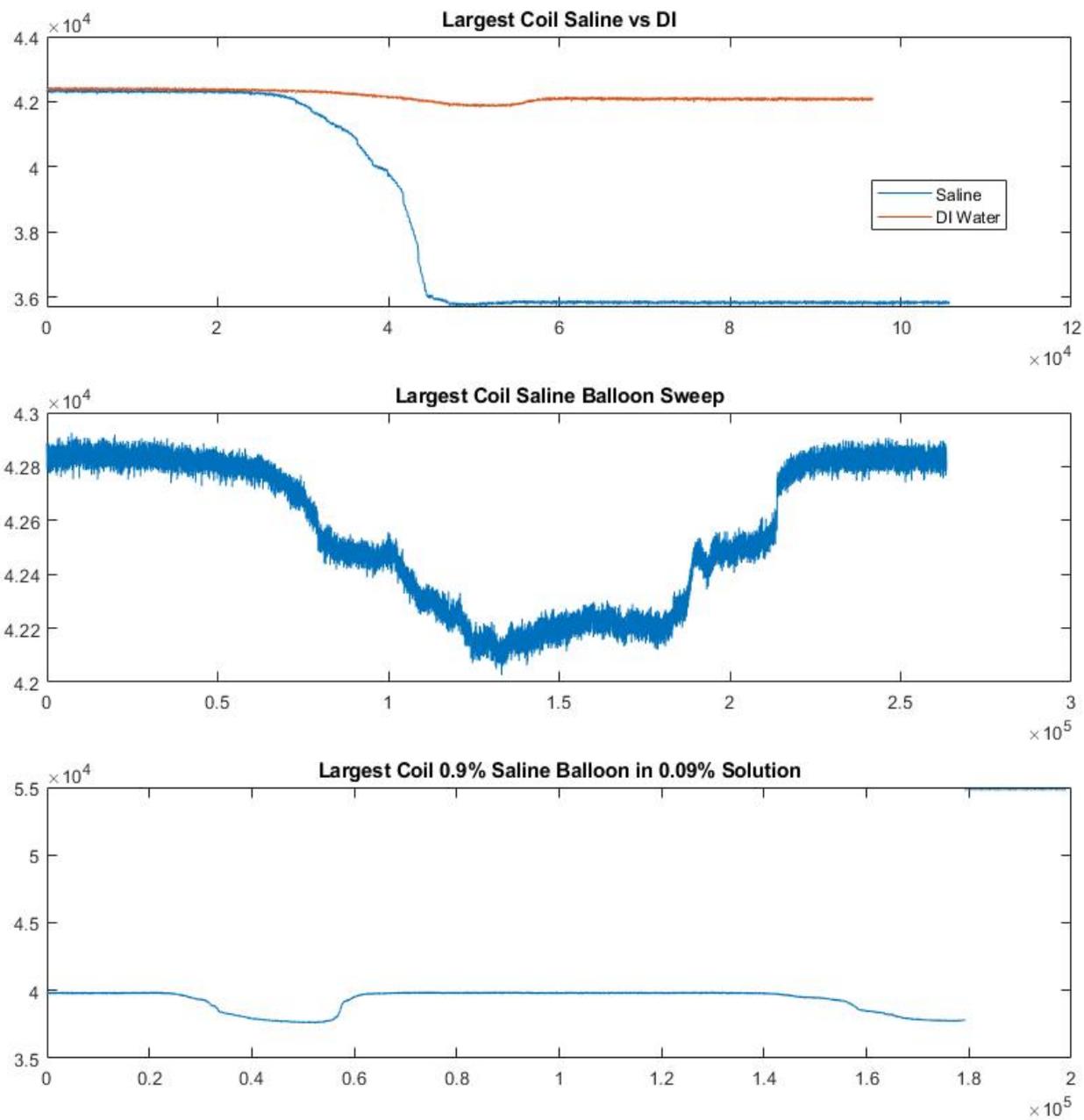
Figure 3-5: Demonstrating Feasibility of Large Coil - DI Water vs Saline.
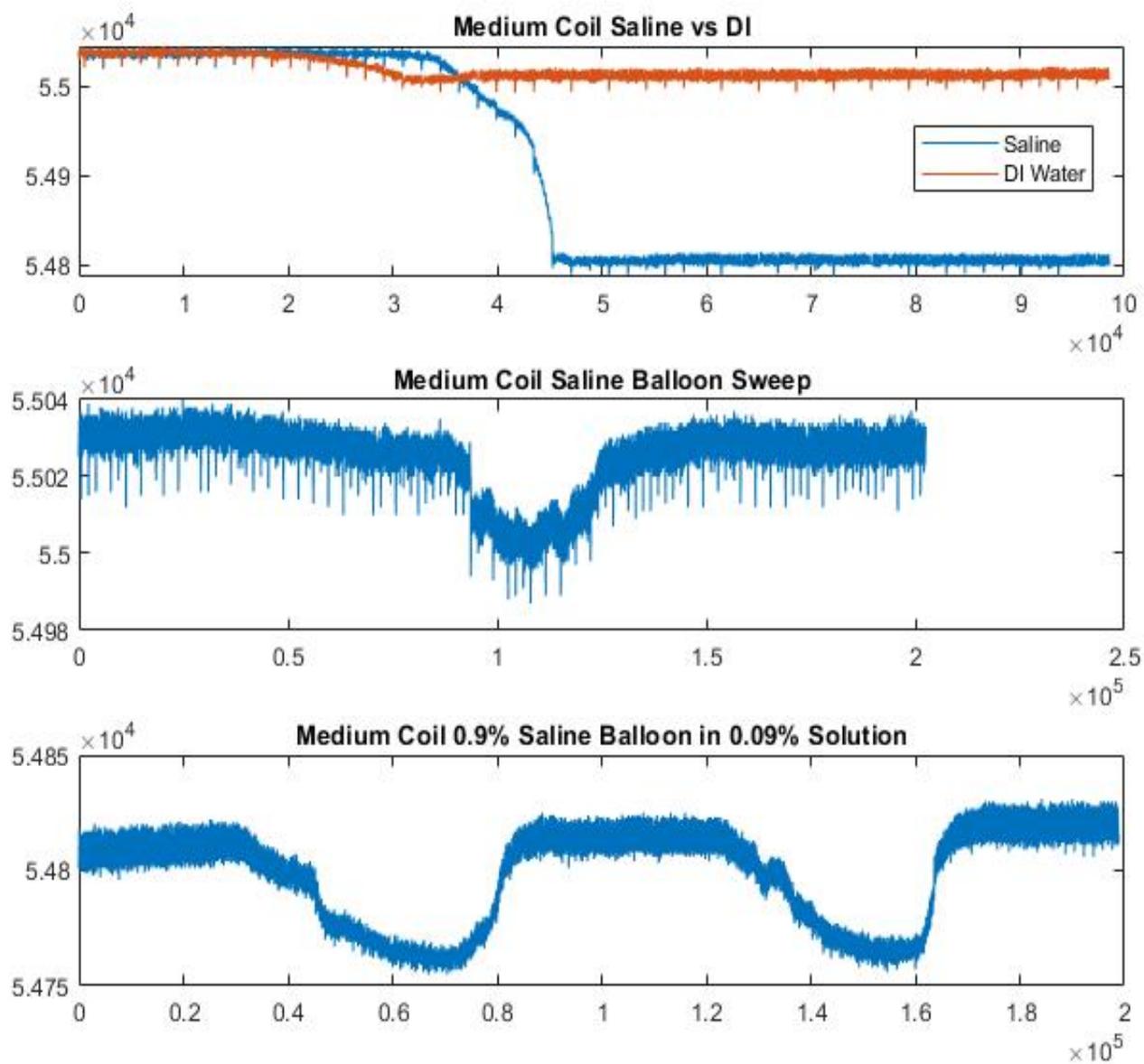
Figure 3-6: Demonstrating Feasibility of Medium Coil - DI Water vs Saline.
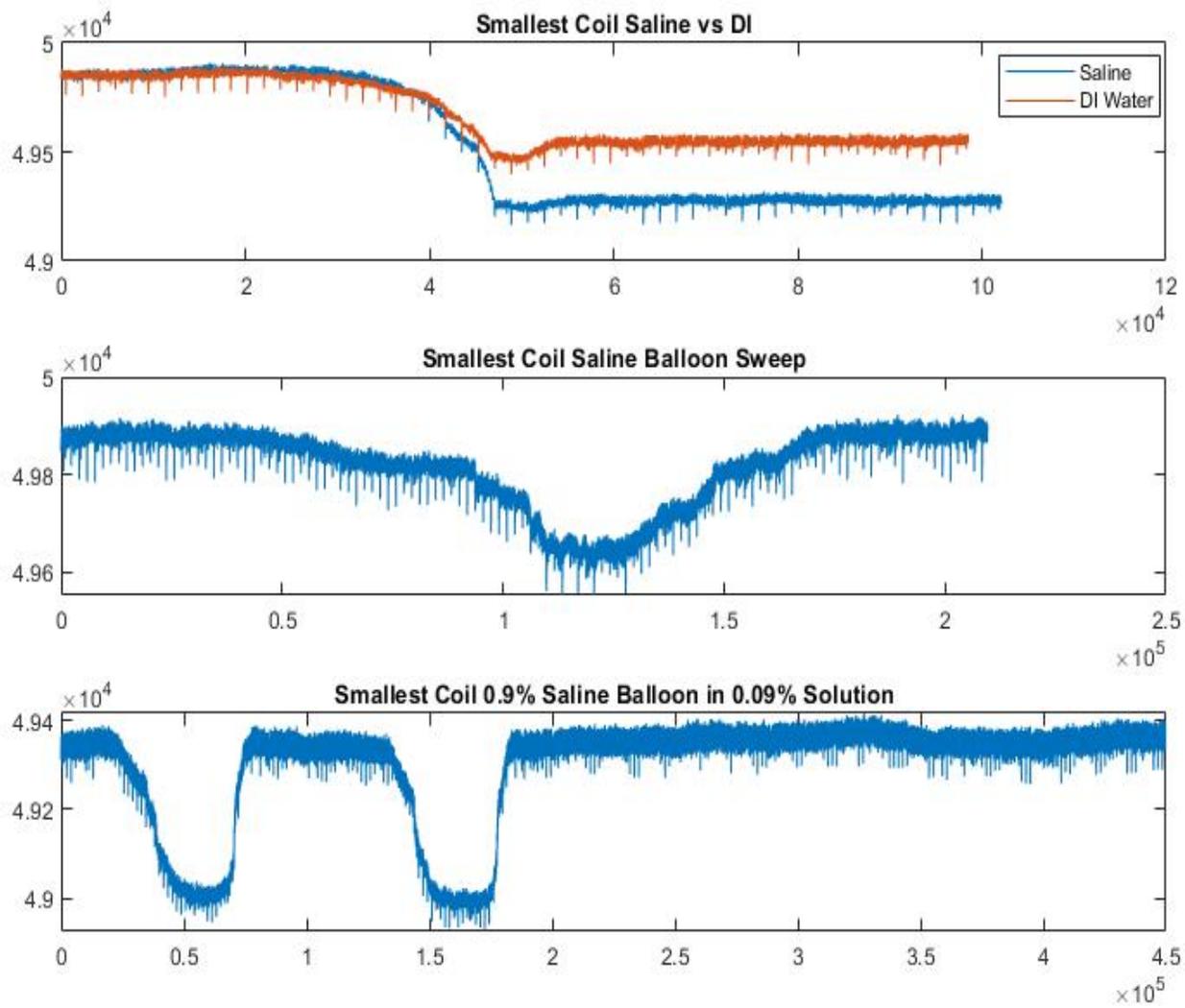
Figure 3-7: Demonstrating Feasibility of Small Coil - DI Water vs Saline.

These preliminary sensor experiments teach us several things. Primarily, when the ECD sensors are operating in air with no target, they are sufficiently stable with little drift, as seen in Experiment 1 for all coils. However, the introduction of a relatively non-conductive DI water solution may decrease coil resistance slightly, and the introduction of conductive saline will significantly decrease coil resistance. Predictably, the degree of damping seen in each coil was positively correlated with the size of the coil, with larger diameter coils boasting greater damping.

Furthermore, all three coils were successfully able to detect the saline-filled balloon while scanning in Experiment 2. The output from each ECD sensor demonstrated an inverted Bell curve, with the trough of the curve achieved when the sensor was directly above the balloon and maximum damping was achieved. These experimental data confirm the idea of utilizing ECD sensors to scan the head, since regions of increased conductivity may result in the highest damping values, while regions of decreased conductivity may result in the lowest damping values through differential scanning.

Lastly, the results from Experiment 3 demonstrate that ECD scanning may still be achieved in non-air media. 0.09% saline has a conductivity value of roughly 0.16 S/m, which is comparable to that of the human brain (0.20 S/m). Thus, because accurate sensing is achieved with the inflation of a saline balloon in a relatively less conductive media, it is feasible to assume that the translational properties of our ECD sensor may hold when applied to experimental stroke models.

3.6 Constructing a Benchtop Brain Model

Construction and testing with benchtop human brain models was necessary to demonstrate the feasibility of the sensor prior to translation to human models. Store-bought gelatin was added to 1000mL of DI water following the formula developed by Kandadai et al. and brought to a boil

[85]. A plastic bag was placed within the plastic skull model such that the opening of the bag exited the foramen magnum on the skull. Once all of the gelatin had dissolved, it was allowed to cool, and the conductivity was measured. Table salt was added to the solution to bring the conductivity to 0.2 S/m. The skull was then placed in the refrigerator until several hours before experimentation, at which point it was removed and allowed to warm to room temperature (Figure 3-8).

Figure 3-8: Constructing a gelatin brain model.

To demonstrate the feasibility of our sensor, we developed a benchtop intracranial hemorrhage model. We developed this model using a plastic life-sized skull replica, gelatin brain parenchyma, and diluted saline to mimic blood. The gelatin brain was confirmed to have the same uniform conductivity at room temperature as its in vivo counterpart, which is 0.2 S/m [85, 86]. Saline was diluted to a conductivity of 0.65 S/m to mimic blood and injected into several latex balloons, with the volume of each balloon ranging from roughly 20mL to 200mL. Eight equidistant horizontal scanning rows were marked onto the skull with flexible tubing, with the first row just above the eyebrows and the last row at the occiput as described in Section 2.7, along which the sensor moved

to measure and record R_p values. A third-party placed one of the balloons within the skull, and the individuals scanning were blinded to hemorrhage size and location (Figure 3-9).

Figure 3-9: Placing a saline hemorrhage mimic in the model.

The design of this model allowed us to confirm the repeatability of each experiment, and it allowed us to test several different sized coils for each hemorrhage volume and location. Feasibility of benchtop models allowed for a smooth transition to live human experimentation.

3.7 Point-Scanning Model

Preliminary experiments with the ECD sensor focused on point-scanning of the skull. To accomplish this goal, 11 points were marked on the plastic skull model including front, back, left, right, top, top right, top left, back right, back left, front right, and front left. Each sensor was placed at each location to record data. Data was recorded twice per point: once for control values with no saline blood mimic in place, and then again when the saline balloon was placed. Differential

scanning was implemented, and the points with the lowest R_p values predicted the greatest probability of hemorrhage since higher conductive areas correspond to higher damping, and thus reduced R_p. Two point-scanning experiments were conducted to demonstrate the feasibility of ECD stationary scanning through the plastic skull and to show that all three sensors may detect superficial lesions. Data was recorded in series from the large, medium, and small sensors respectively to reduce the degree of capacitive coupling taking place between the sensors when more than one sensor was active at a time. Diagrams for the two experiments may be seen in Figure 3-10 and 3-11.

Coil	Large	Medium	Small
Front	-200	50	-220
Back	-40	10	120
Left	10	60	120
Right	-380	60	120
Top	-200	0	0
T-R	-220	0	240
T-L	-390	10	120
F-R	-100	0	120
F-L	0	-40	220
B-R	-280	0	120
B-L	-200	20	100
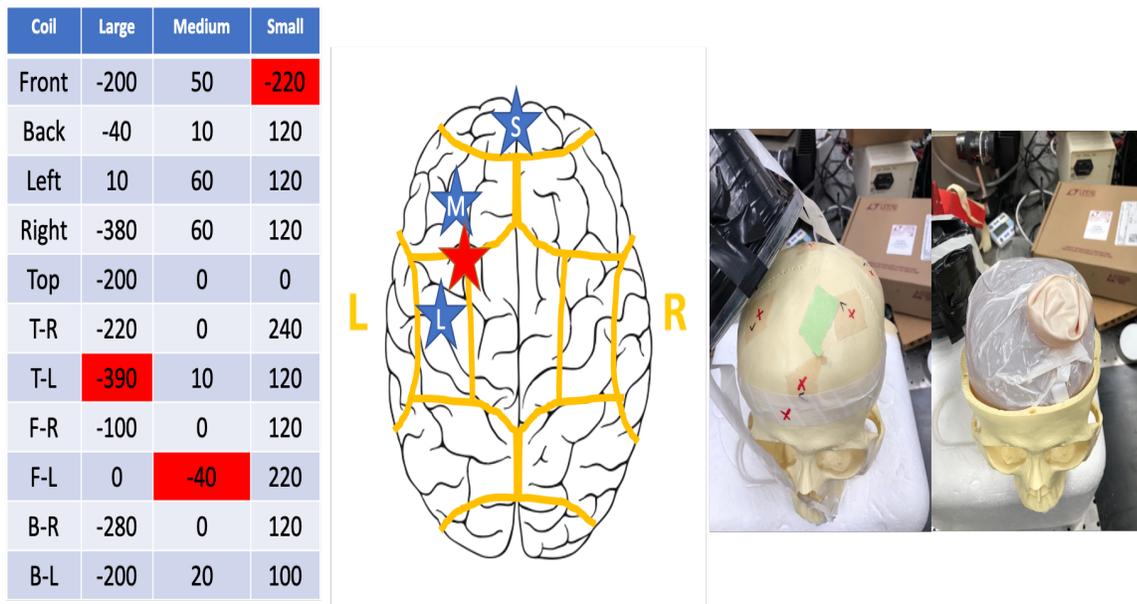
Figure 3-10: Demonstration of the first point-scan benchtop model.

Coil	Large	Medium	Small
Front	-390	0	-100
Back	-500	-80	210
Left	-630	-20	230
Right	-930	-30	200
Top	-600	-100	190
T-R	-190	-90	150
T-L	-500	-130	20
F-R	-360	-180	40
F-L	-380	-110	330
B-R	-630	-90	170
B-L	-730	-70	170
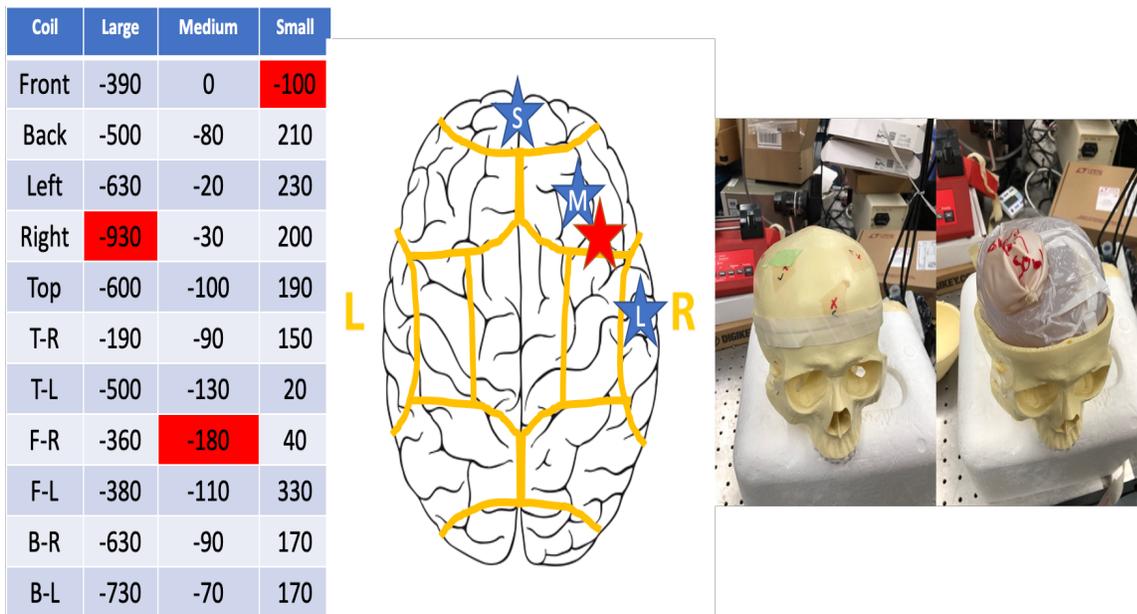
Figure 3-11: Demonstration of the second point-scan benchtop model.

The experiments above demonstrate feasibility of an ECD sensor in detecting hemorrhages within

the head model. Point-scanning showed reasonable accuracy in locating two intracranial lesions.

The large, medium, and small coils in the first experiment (Figure 3-10) suggest that the 50mL hemorrhage may be located at either the top left, front left, or front of the head respectively. Inspection revealed that the hemorrhage was located between the top left and front left of the brain. In the second experiment (Figure 3-11), the large, medium, and small coils suggested that the 50mL hemorrhage was located at the right, front right, and front of the head respectively. Further inspection revealed that the hemorrhage was closest to the front right area of the head.

Several hypotheses were considered as to why all three coils did not agree about the location of the hemorrhage. First, point-scanning introduces a great amount of empty space between each scanning point, and lesions located within these "empty spaces" may not be accurately resolved. Furthermore, when point-scanning is implemented, the degree of damping and resistance change within the sensor is proportional to the degree of superimposition between the sensor coils and the balloons. Because the skull is a convex hemisphere, point-scanning does not fully consider the geometric considerations of the skull or the variety of placement of an intracranial lesion.

With these limitations in mind, additional scanning techniques were considered. Continuous scanning presented an opportunity to avoid the limitations of point-scanning while achieving greater spatial resolution than previous techniques.

3.8 Continuous Scanning Model

The second iteration of the benchtop skull model involved the development of continuous scanning techniques. As described in Section 2.7, guide rails with eight equidistant scanning paths were developed to facilitate scanning across the skull model. Each scanning path was traversed with each ECD sensor from right to left while data was recorded. Polytetrafluoroethylene (PTFE)

teflon spray was utilized to minimize the coefficient of friction between the silicon attachment on the sensor and the plastic tubing utilized to create the rows.

Following completion of scanning, the >40,000 data points collected by each sensor for each row were downsampled to eight averaged points per scanning row. Interpolation was implemented to fill in the gaps between each data point. This step was performed to filter out high frequency noise and any anomalous data that may arise as an artifact of hand scanning. The results of the continuous scanning may be seen in Figure 3-12.
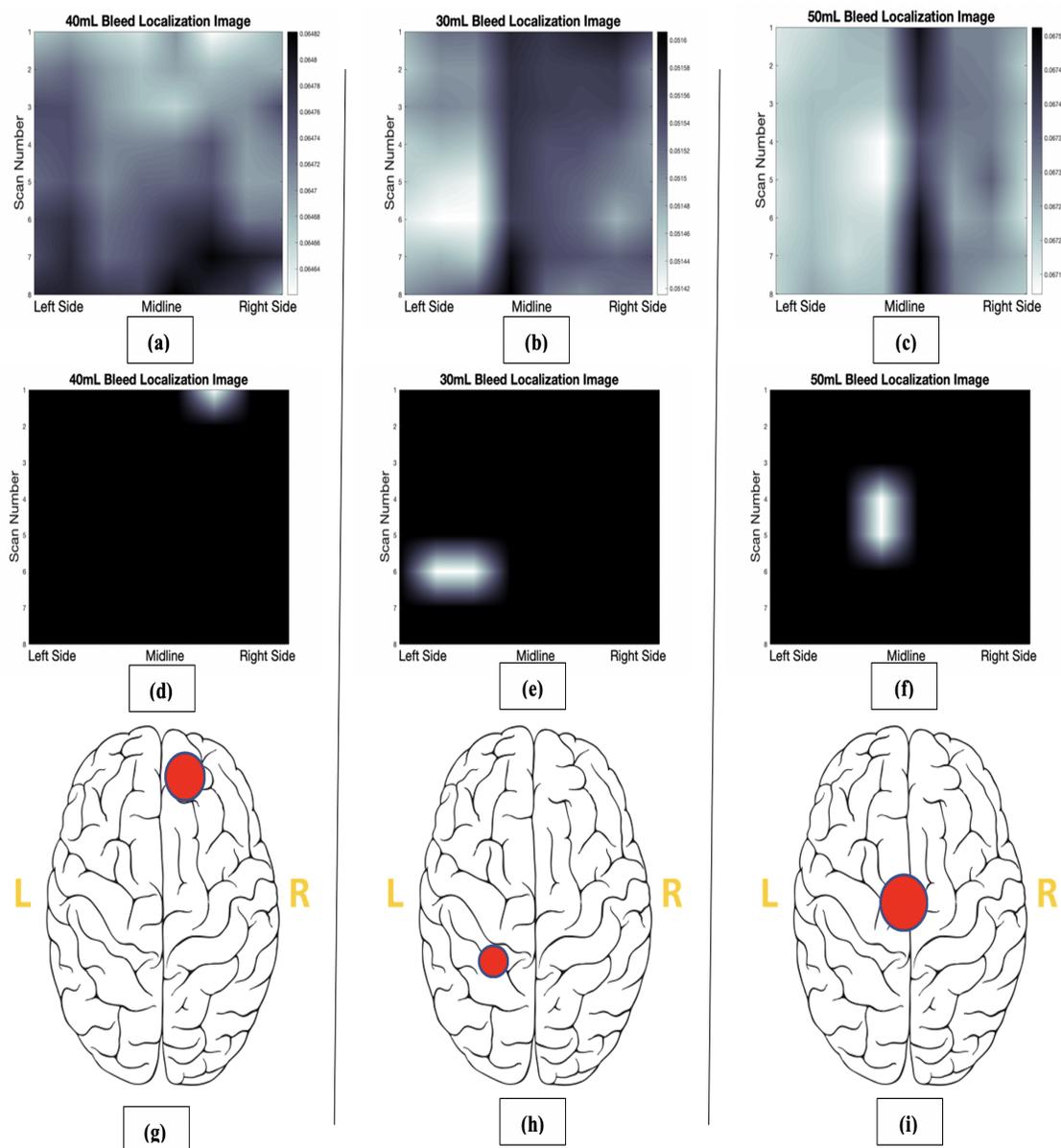
Figure 3-12: Demonstration of benchtop continuous scanning.

Scanning the head model with the ECD sensor, we are able to create composite images that

predict bleed location. More conductive areas are shown brighter, and less conductive areas are

shown darker. With reference to Figure 3-12, the raw data collected after scanning along 8 scanning paths of a brain with a 40mL, 30mL, and 50mL hemorrhage is converted to an image in (a), (b), and (c) respectively. Using thresholding methods, we clean the data to produce the images seen in (d), (e), and (f). Actual bleed locations can be seen in (g), (h), and (i) by the red circles. Excellent spatial resolution is achieved in all cases on a centimeter scale as based on the overlap between the actual and predicted 2D rendered images.

The thresholding methodology utilized in our benchtop experiments acted to preserve the highest 5% of all conductivity values (i.e., greatest amount of damping) while setting the remaining 95% of data to the lowest local conductivity values. As such, the areas with the highest probability of conductive hemorrhage (or non-conductive ischemia) may be highlighted through the use of thresholding.

In all benchtop skull experiments (n=16), it was possible to approximate the location of the hemorrhage with centimeter resolution. The average time spent scanning across the entire head with one sensor was 2.43 minutes, at which point enough data was collected to produce a predictive conductivity map. This potentially marks a drastic reduction (~50 times less) in the time-to-diagnosis in potential stroke patients and establishes the feasibility of the ECD device as a hemorrhage sensor.

3.9 Optimizing Image Production

The optimal sampling dimensions of data to produce two-dimensional images with the ECD sensor sensor were thoroughly explored. Configurations involving 2x2, 4x4, 8x8, 16x16, and 31x31 heatmaps were each created following scanning the head model with a 50mL bleed placed

in the right superior medial frontal lobe for the medium coil and right anterior frontal lobe for the large coil.

Each scanning configuration involved the placement of additional scanning rows on the head. For example, for the 16x16 configuration, 16 equidistant scanning paths were drawn on the skull and plastic guide rail tubing was glued to ensure accurate scanning. More than 40,000 data points were collected for each of the 16 rows during the scanning process. Following data collection, all data was post processed and downsampled to produce a total of 16 averaged and equally sampled points for each of the 16 rows.

At this point, heatmaps were generated using the 16x16 data to predict the location of the lesion. Lighter boxes indicated a higher conductivity, while darker boxes indicated a lower conductivity. Through this process, it was possible to determine which configuration resulted in the highest accuracy of signal while maintaining reliable spatial resolution (Figure 3-13).
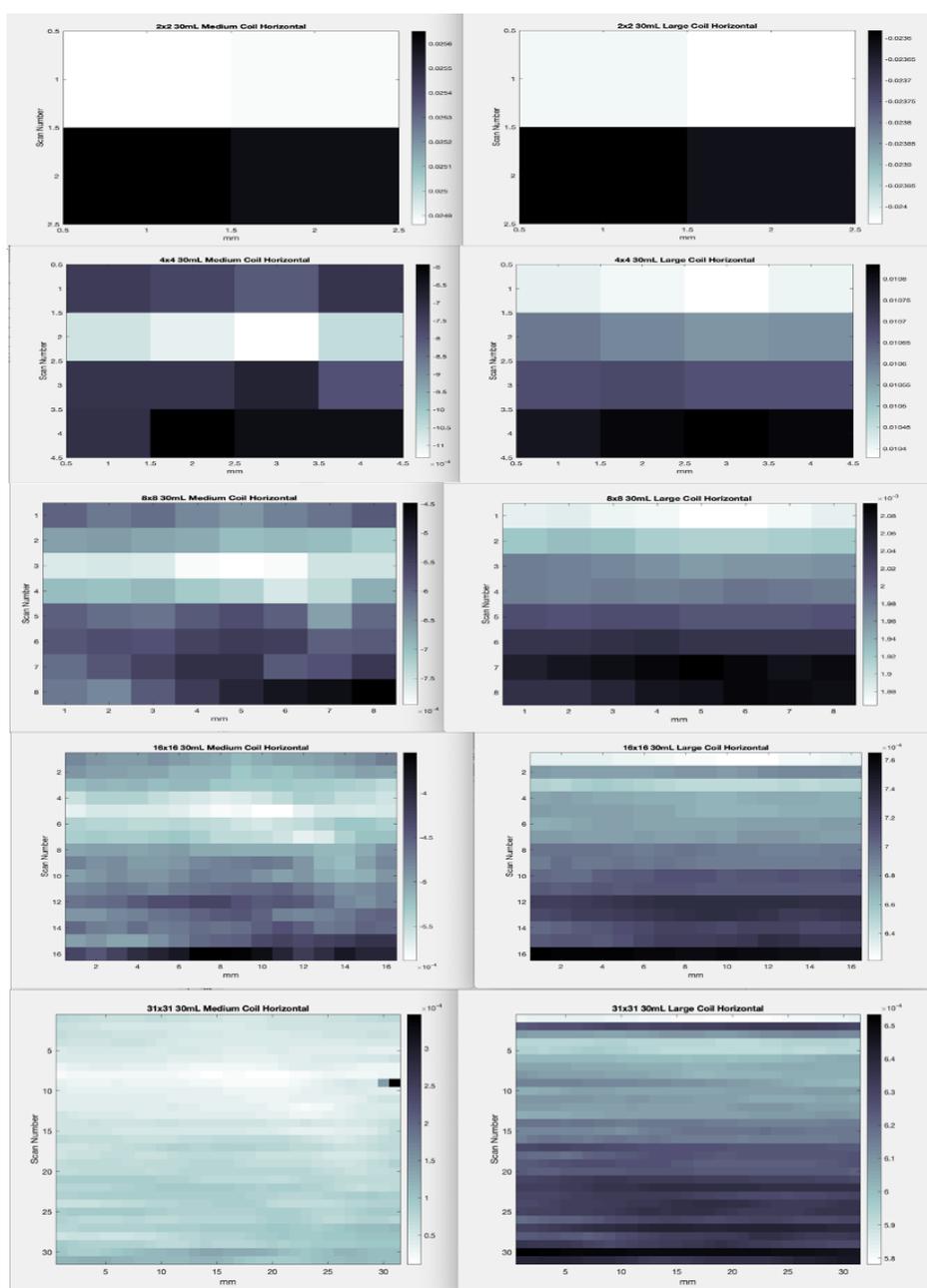
Figure 3-13: Optimized imaging dimensions.

Overall, each scanning dimension was successfully able to locate the approximate region of the balloon. However, some scanning dimensions performed better than others. When determining the optimal scanning dimension, it is important to consider both the accuracy of the predicted location and the noise level generated within the figure.

For example, while the 4x4 dimensional grid did successfully locate both balloons using the medium and large coils, it failed to provide additional spatial data regarding accurate lesion location. Conversely, the sampling procedure necessary to produce the 31x31 dimensional grid failed to average out some of the additional noise picked up by the sensor, resulting in erroneously non-conductive points on both medium and large coil heatmaps. As a result, the rest of the points are erroneously shown as having higher conductivity values than expected. This noise is likely due to the limitations of hand scanning and the innate noise produced within the commercial chips attached to the sensor.

Thus, we considered the 8x8 and 16x16 configurations as our optimal scanning protocol. In the end, we opted to go with the 8x8 over the 16x16 because scanning 8 rows takes half the time of scanning 16 rows. By reducing the scanning time with the sensor, it is possible to then reduce the time-to-diagnosis which is critical in the case of neurovascular emergencies such as stroke.

Following post hoc sampling to produce 8x8 grids after scanning, interpolation may be used to smoothen the heatmap and generate the final prediction map seen in Figure 3-12.

3.10 LC Tank vs LDC 1101 Circuits

As previously mentioned, the LDC 1101 commercial inductance-to-digital chip had a non-optimal amount of internal noise (SNR<10), and we decided to pursue the development of our own LC tank for scanning with a higher SNR (SNR=14). To achieve this goal, the circuitry developed

in Section 2.9 was utilized to scan a 30mL saline-filled balloon placed within a benchtop skull model. Scanning took place, and data was recorded for analysis. Table 3-1 displays the sensor output for the 30mL scan seen in Figure 3-12.

Raw Data Using LDC 1101 for 30mL Hemorrhage (ΔRp)							
0.05147783	0.05151702	0.05151512	0.05157156	0.05155726	0.05157439	0.05158249	0.05154926
0.0514601	0.05149477	0.05149441	0.05156482	0.05155073	0.05155151	0.05155644	0.05149823
0.05148837	0.05150357	0.05149698	0.05156347	0.05155396	0.05154701	0.05155019	0.05150617
0.0514555	0.05147271	0.05146341	0.0515602	0.0515377	0.05153883	0.05152026	0.0514899
0.05145736	0.0514377	0.05142599	0.05155846	0.05153603	0.05152547	0.0515074	0.05149665
0.05143376	0.05141568	0.05141665	0.05155251	0.05153875	0.0515203	0.05147644	0.05150756
0.05146325	0.0514732	0.05145677	0.0515933	0.05154262	0.05153641	0.05152592	0.05153943
0.05149587	0.05151602	0.05153225	0.05160622	0.05151892	0.05149931	0.0515189	0.05151309

Table 3-1: Raw data using the LDC 1101.

In the table above, the lowest R_p (highest conductivity) is seen in the sixth row, second column. Following 95% thresholding, this point is the one that will light up as seen in the 30mL example of the associated figure. However, it is clear that the entire matrix associated with the produced image contains a lot of noise and thresholding is necessary to fully establish the location of the lesion.

The use of an LC tank in detecting an intracranial lesion is based on a different set of principles. As previously discussed, introduction of a conductive balloon would increase the coils'

maximum operating Rf. The circuitry is much less noisy as well, and data obtained from the LC

tank for the identification of a 30mL lesion in the same position is shown in Table 3-2.

Raw Data Using LC Tank for 30mL Hemorrhage (ΔRf)							
0	0	0	0	0	0	0	0
0	0	0	0	0	0	0	0
0	0	0	0	0	0	0	0
0	0	0	0	0	0	0	0
0	0	0	0	0	0	0	0
0	0.04	0	0	0	0	0	0
0	0	0	0	0	0	0	0
0	0	0	0	0	0	0	0

Table 3-1: Raw data using the LC tank.

The data in the table above demonstrates a 0.04 MHz increase in Rf at the location of the

balloon following differential scanning. In addition, the noise floor in the case of the LC tank is

much more homogeneous and accurate in differentiating signal from noise. Importantly, data

tables this clean may be achieved prior to thresholding methods, rendering 95% thresholds useless

in the case of a LC tank circuit for stroke scanning.

In addition, the table representing the output from the LC tank is measured in the units of

Rf while the table representing the output from the LDC 1101 sensor is in the units of R_p. However,

several advantages still favor the use of commercial sensors. First, the LC tank currently only

supports point-scanning because the Rf must be tuned and determined at each point while

scanning. As such, the LDC 1101 sensor allows for faster scanning. Furthermore, the sensor was

also attached to a network/spectrum analyzer to measure the magnitude of the input signal against

the frequency of the instrument. The graph of impedance and θ may be seen in Figure 3-14 below.
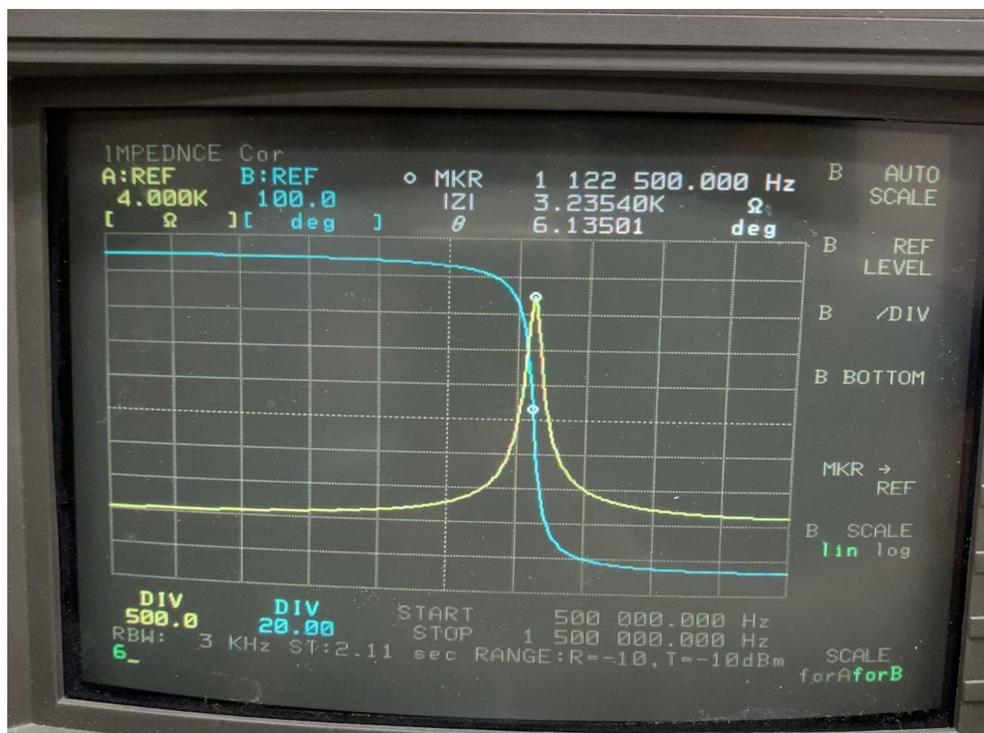
Figure 3-14: Spectrum analysis of impedance and θ.

A similar analysis was also performed using the spectrum analyzer to determine the inductance

and resistance profiles of the sensor over a 1MHz frequency range. This figure may be seen as

Figure 3-15 below.
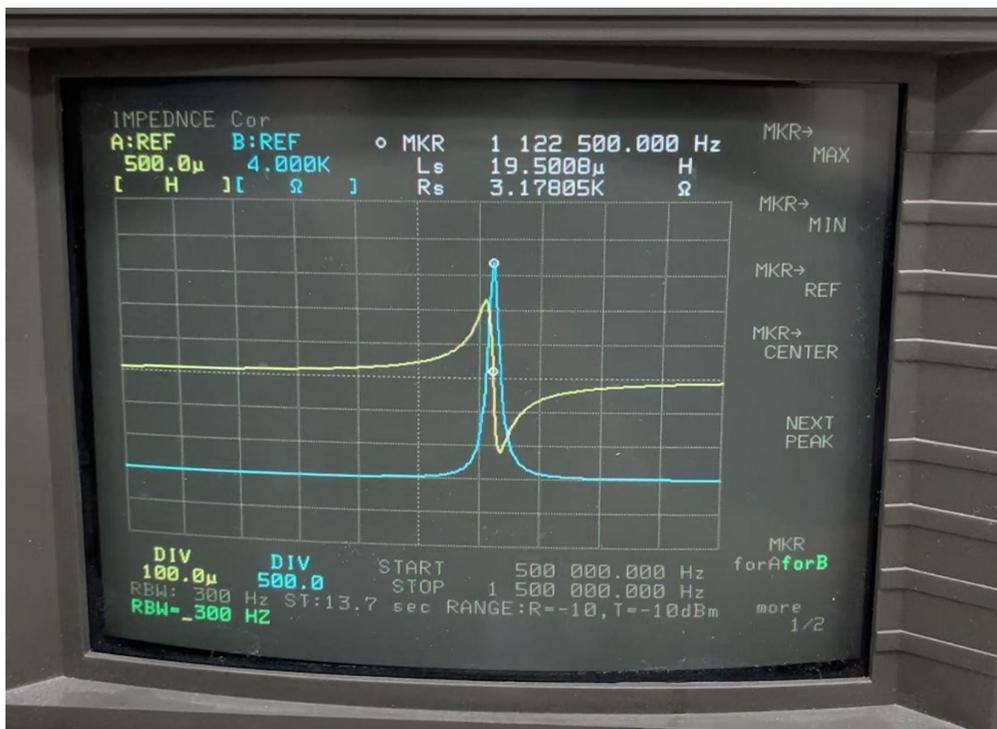
Figure 3-15: Spectrum analysis of impedance and resistance.

In both cases shown here, the network/spectrum analyzer was tuned immediately prior to characterization. However, because the equipment is several decades old, it is possible that some of the values were slightly different than what we expected while using the oscilloscope, signal generator, and frequency counter. Regardless, the general waveforms for the two experiments shown above demonstrate adequate performance around 1MHz, confirming previous experiments investigating the efficacy of LC tanks for stroke detection.

Further advancements of the LC tank allowing for automated readout, Rf maximization, and data saving to the computer may favor the LC tank over the LDC sensor. Undoubtedly, the LC tank demonstrates a greater SNR with accurate and intuitive noise floors and signal outputs that are highly responsive to changes in conductivity. Lastly, signal characterization using a network/spectrum analyzer confirmed the robust capacity of the LC tank.

3.11 Conclusion

Benchtop experimentation with the ECD sensor demonstrated feasibility in detecting, localizing, classifying, and imaging stroke subtypes. Through the creation of tuning curves for distance, volume, and shape, we demonstrate the possibility of providing information regarding these variables following head scanning. In addition, both point-scanning and continuous scanning were successful in localizing intracranial lesions. However, continuous scanning boasted higher accuracy and minimized scanning time and efforts. Lastly, both image production and the sensor circuit were evaluated and optimized to increase accuracy and SNR while reducing unwanted noise.

Overall, these benchtop experiments demonstrated the feasibility of the ECD sensors for stroke diagnostic applications. The next few chapters will focus on the translational potential of the ECD sensors for human applications. The problems solved during the benchtop experimentation phase allowed for a more seamless transition into more sophisticated experiments and reduced the time spent during the iterative sensor design process. Finally, much of the software developed at this stage was retrofitted and improved for all subsequent experiments described in this thesis.

CHAPTER 4: CADAVER EXPERIMENTATION

4.1 Introduction

Translational medical innovation encompasses sufficient benchtop experimentation and development that can be easily translated into clinical models and applications. With any medical device, the ultimate goal for development is clinical use with live human patients. However, such a goal requires incremental transitioning through the use of more complicated and realistic models to demonstrate device safety and efficacy.

To demonstrate the clinical efficacy of the ECD stroke sensor, cadaver modeling and testing was explored following successful benchtop experimentation, as described in Chapter 3. The goal of this chapter is to demonstrate the potential effectiveness of the stroke sensor when applied to a likelike human cadaver ICH model. In addition, this chapter allows for innovation on a human head model and a thorough understanding of potential limitations with clinical scanning, which will greatly inform the protocols developed to scan live human patients in Chapter 5.

4.2 Cadaver Model Development

A plethora of cadaver models have been used in clinical medicine to practice a variety of multiple surgical procedures, to train surgical residents, and to innovate novel procedures and devices for live human use [87–91]. Such cadaveric simulation models have been popularly adopted by surgical training programs for clinically accurate testing due to the preserved anatomy

of specimens. In addition, the optimal haptic feedback provided by such models allows for accurate modeling of surgical techniques and instrumentation.

As a consequence, the realistic properties of cadaveric simulation modeling provided an opportunity to translate the ECD sensor to an intermediate human setting prior to full-on live human clinical testing. Several pilot cadaveric studies have confirmed the feasibility of an ECD sensor for intracranial hemorrhage detection and imaging. Using the translated experimental setup involving a wearable skull cap with eight equidistant scanning paths made of flexible tubing, each cadaver head was scanned. The cadaveric simulation models consisted of fresh frozen, unfixed human cadaver heads with no history of cerebrovascular disease. All experiments took place at the Keck School of Medicine of USC Surgical Skills Simulation and Education Center.

A right supraorbital skin incision and skull burr hole are made with the cadaver in supine position. The quality of the brain was evaluated to ensure that it still retained properties of a live human brain. Frozen uncoagulated porcine blood was thawed, and a various volume of blood was injected directly through the burr hole, 7cm deep into the brain parenchyma (Figure 4-1 & 4-2).
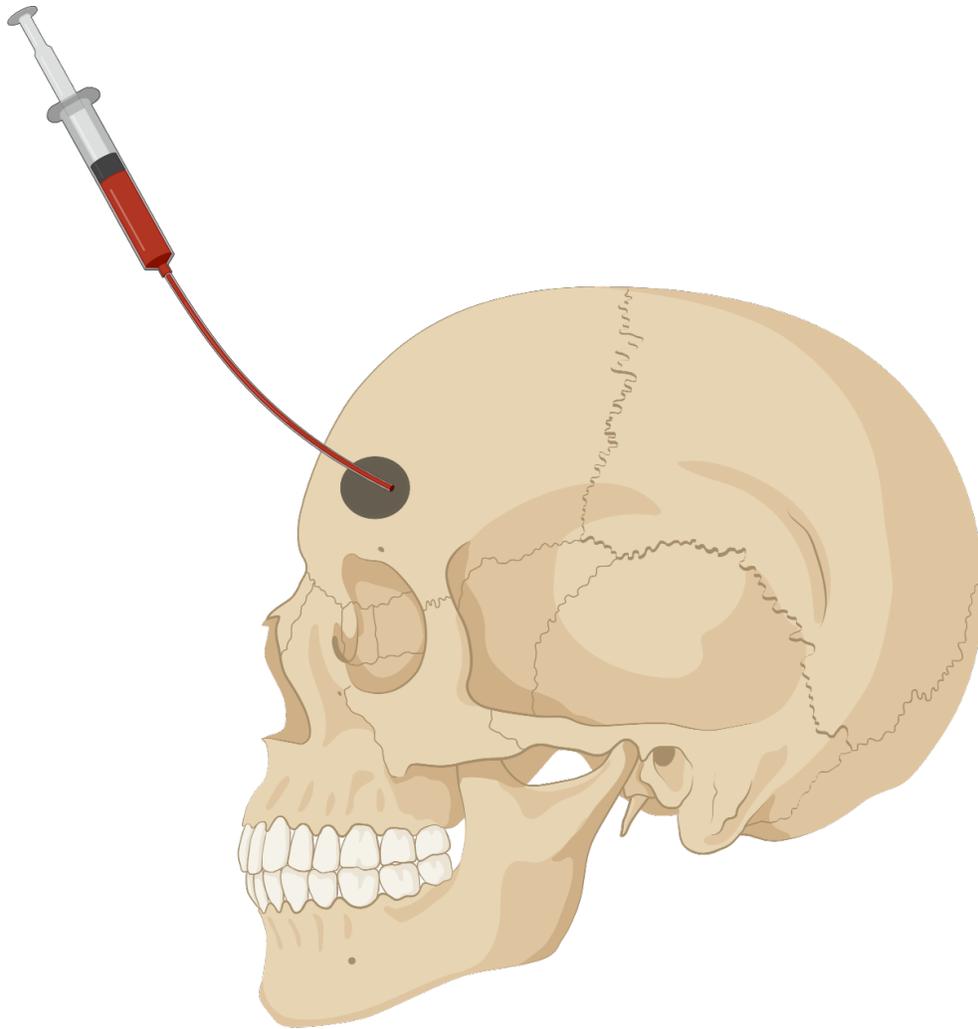
Figure 4-1: ICH cadaver model of blood insertion. Created with Biorender.com.

Figure 4-2: Actual ICH cadaver model.

Scanning the cadaveric head with the large, medium, and small sized coils allowed for image production, and a composite image was created by adding the three heatmaps. The image

analysis and thresholding process used here is the same workflow used in the benchtop experiments. The presence of a signal in all coils suggests that the hemorrhage falls within the detection distance of all three coils, which predicts that the hematoma is less than 2.29cm from the sensor surface (Figure 4-3).
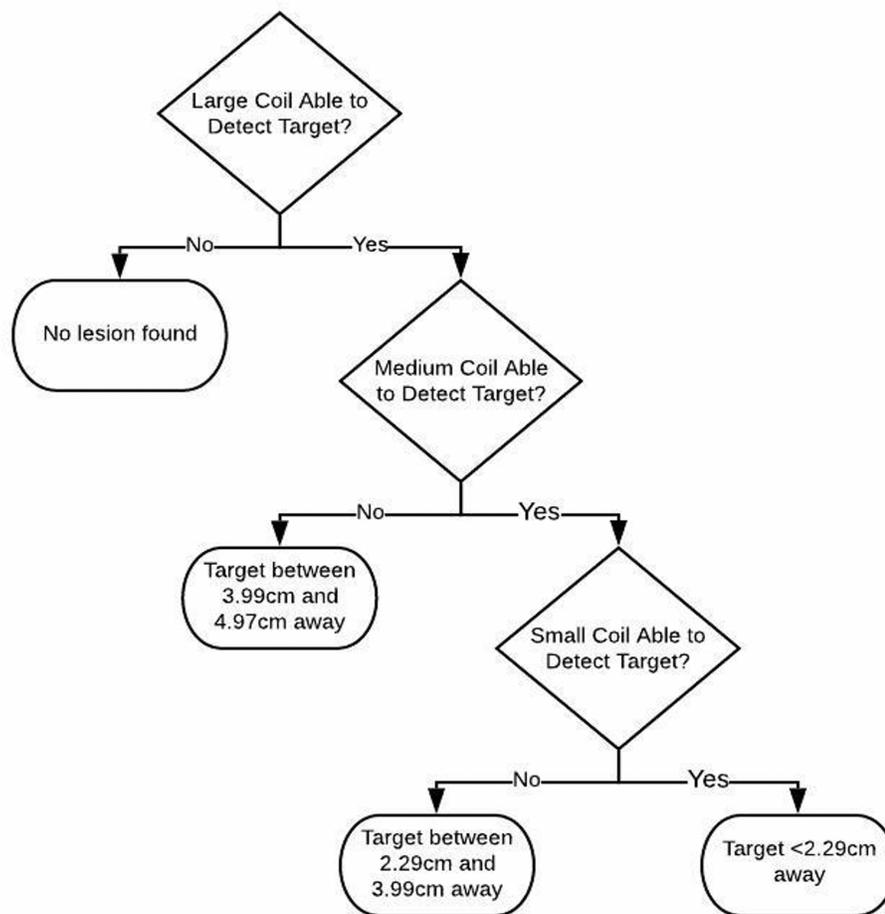
Figure 4-3: Flowchart outlining the binary decision tree used to approximate lesion depth.

4.3 ECD Sensor Cadaver Testing

With an established protocol for the cadaver model, the ECD sensor was utilized to scan to collect conductivity data. Prior to a 30mL ICH injection, each coil was used to scan the head, in series. Data collected at this stage were saved for use as control measurements for the cadaver heads. Following 30mL hemorrhage placement within the right lobe of the brain, each coil was used to scan the cadaver head once more to calculate the post-lesion conductivity values. The approximate area of hemorrhage injection is seen in Figure 4-4a. The composite image generated at this point is shown in Figure 4-4b.
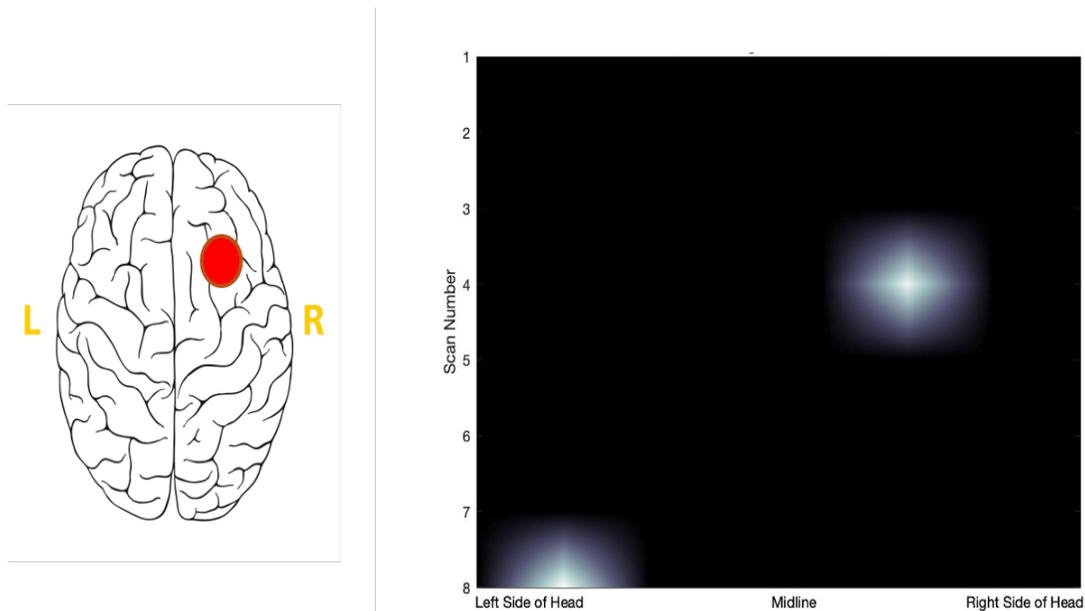
Figure 4-4: (a) Injected location of 30mL porcine hemorrhage (b) Image produced by ECD sensor of 30mL porcine hemorrhage.

As seen in the figure above, the spot lighting up on the mid-right side of the brain correlated well with the ICH injection point. However, an additional signal lit up on the ECD image in the bottom left side of the head near the nape of the neck. To fully understand what was happening within the confined of the ICH model cadaver head, the experiment was repeated with noncontrast

CT imaging to confirm the location of the lesion (Figure 4-5a). Each sensor was utilized to scan the head, 60mL of porcine blood was injected into the left cerebral hemisphere, and each sensor was used to scan the head once more.

Interpreting the conductivity map, we expected the bleed to be positioned at the posterior-left corner of the head, just behind the left ear. To confirm the actual location of the hemorrhage, noncontrast CT imaging was used to create axial, sagittal, and coronal sections with 1mm thickness, as it represents the current gold standard for the diagnosis of hemorrhagic stroke and other intracerebral hemorrhages. CT imaging corroborated the presence of a hemorrhage in the posterior-left corner of the head, in the same location detected by our sensor (Figure 4-5b). Furthermore, the estimated hemorrhage depth beneath the skull is roughly 1.5cm, which is far less than the detection limit for either of the sensors. Bone contrast enhancement and windowing were also performed with CT to confirm that the hyperdense structure seen on CT was in fact blood, and not a bony abnormality (Figure 4-6).
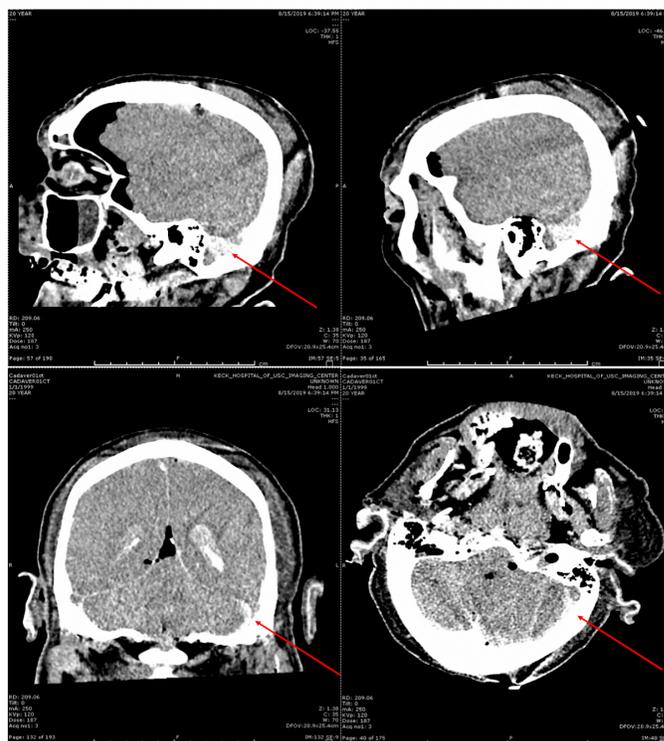
(a)
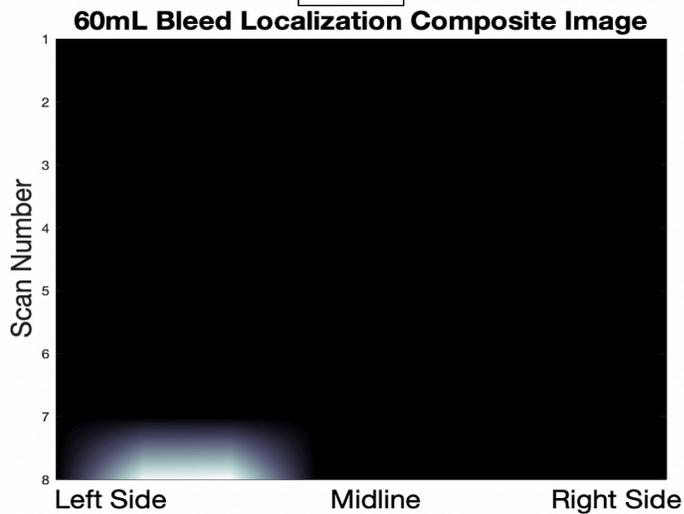
(b)

Figure 4-5: (a) CT scanning of 60mL porcine hemorrhage (b) Image produced by ECD

sensor of 60mL porcine hemorrhage.
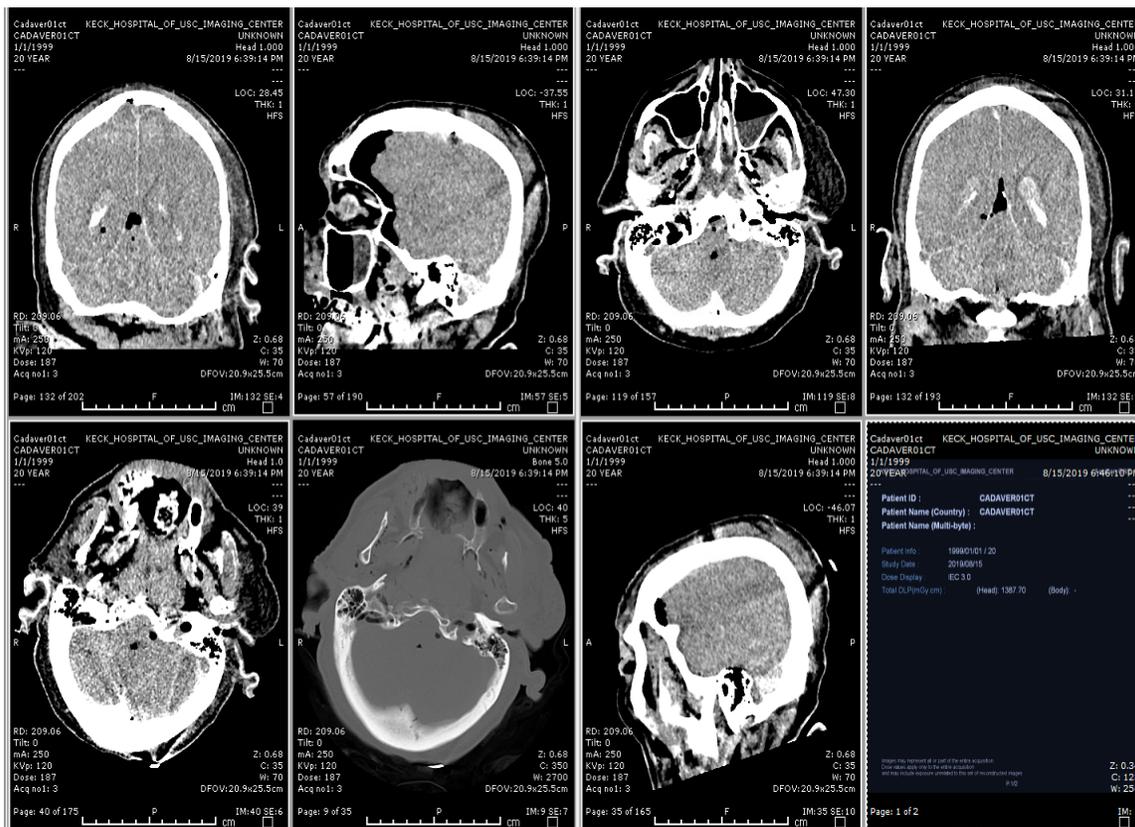
Figure 4-6: CT imaging in all dimensions, in addition to bone contrast enhancement.

As seen in the example above, the lesion was successfully captured using the sensor. However, the same phenomenon seen in Figure 4-4 is also seen in Figure 4-5 in which a large signal is produced in the bottom left side of the head near the nape of the neck. Further investigation demonstrated that the porcine hemorrhage mimic utilized in this study lacked clotting factors, which are classically present during an acute neurological event. The lack of such factors decrease the clotting capabilities of blood, resulting in a permanent liquid state. As such, gravity tends to draw the liquid to the lowest point in the skull, which happens to be the back of the head at the occiput near the nape of the neck. This phenomenon likely happened in both cases shown above, and is further confirmed by the CT imaging seen in Figure 4-5.

Successful demonstration of the ECD sensor solidified the hypothesis that such a sensor may be applicable for applications of acute aberrations in cerebral conductivity, including but not limited to strokes. ECD sensing may accurately detect ICH and produce an image in real-time, even through thick cortical bone. Several limitations, in addition to the lack of clotting factors, became apparent while performing cadaver modeling experiments. Primarily, the quality of porcine hemorrhage blood mimics did not fully match those of actual blood seen during an ICH. Thus, an analysis of the porcine blood conductivity revealed a value of 0.42 S/m. Since normal human blood has a conductivity of 0.65 S/m, the reduced conductivity of porcine hemorrhage mimic inherently resulted in diminished signal production. As a result, the potential for signal generation may be greater than that shown in these experiments since the physics underlying the sensor suggest that increased conductivities generate larger signals.

Furthermore, while preliminary inspection revealed that the cadaver brain was in good condition and that the cause of death was not from a neurological disorder or cerebrovascular accident, CT imaging revealed that there was still a good amount of air pockets following thawing for fresh frozen cadaver heads. Since the conductivity of air is roughly 0, increased air pockets may further increase noise within the system and reduce the specificity of our ECD images. Additionally, the development of cadaveric simulation models requires a significant amount of time and effort. First, the cadaveric specimens must be purchased and procured, often at a price of several thousand dollars per head. Next, experienced neurosurgeons with available neurosurgical equipment are necessary to drill burr holes and inject porcine ICH. Lastly, ample funding is necessary to support radiography with a CT scanner.

4.4 Significance of Preliminary Cadaver Results

Previous clinical trials, including the Surgical Trial in Intracerebral Hemorrhage (STICH), as well as the follow up STICH II, failed to demonstrate a statistically significant difference between patients treated with early surgical ICH evacuation and those treated with best medical management [92, 93]. However, the results of the STICH trials have been heavily criticized because they exclude patients with brain herniation, in which neurosurgical intervention is a life-saving procedure, and who may be the patients who show the greatest improvement with juxtaposition to those treated with medical management alone. Similar clinical trials include the MIND and ENRICH trials, which continue to investigate the efficacy of minimally invasive ICH evacuation.

With continuing investigation regarding the optimal treatment of ICH, diagnostic strategies that reduce the time-to-intervention following cerebrovascular accidents continue to be critical. The results of our cadaver experimentation bolster the claim that ECD sensors may allow for rapid triage and stroke imaging and provide diagnostic information accurately in acute neurovascular lesions.

Furthermore, there are two main paths to clinical studies for medical devices pending approval in the United States. First, the traditional route to device production involves collaboration with the FDA to conduct agency testing, pre-clinical experimentation, and first-in-man trials. The second, however, involves early feasibility experimentation with small patient numbers. Feasibility may be accomplished through the demonstration of preclinical data, including but not limited to mathematical modeling, in-vitro testing, benchtop testing, animal experimentation, and cadaver experimentation. With these studies, it is possible to demonstrate the efficacy and clinical feasibility of a sensor prior to the implementation of extensive human clinical testing and examination.

As such, the implementation of cadaveric simulation and testing provided an opportunity to obtain a plethora of feasibility data. The human cadaver heads utilized during cadaver simulation were the most accurate models for human ICH experimentation with respect to both anatomy and conductivity distributions within the specimen. The development of cadaveric simulation models spearheaded a smooth transition towards live human first-in-man clinical testing through the demonstration of device safety and feasibility.

4.5 Conclusion

Overall, intermediate experimentation was required to demonstrate the feasibility of the ECD stroke sensor following successful benchtop experimentation and prior to first-in-man live human experimentation. Because animal models of ICH are difficult to recreate accurately without the use of blunt force trauma, we opted to perform several experiments using fresh-frozen cadaver tissue.

The results of the cadaver simulation experiments were two-fold. First, we successfully demonstrated the efficacy and reproducibility of modeling ICH in a simulated fresh-frozen cadaver head specimen. By doing so, many opportunities arise in utilizing these cadaver models to test novel stroke technologies in addition to their use in neurosurgical and neurological training. Second, we successfully demonstrated the feasibility of the ECD stroke sensor within the context of an accurate human cadaveric simulation model. ICH was resolved in all experiments with reasonable accuracy and heatmaps predicted lesion location very well.

However, one limitation of our cadaveric simulation was the difficulty in simulating ischemic stroke. In the case of an infarct, local blood flow distal to the embolus or thrombus is disrupted while proximal blood flow remains intact. In addition, the ischemic penumbra following

an infarct changes in a time-dependent manner. This phenomenon is difficult to recreate using cadaveric simulation, and either animal or human models are necessary due to the complex physiology underlying these phenomena.

As such, the promising results from the cadaveric simulation trials allowed for live human testing protocol development. In these human trials, we implement testing with both hemorrhagic and ischemic stroke patients and aim to demonstrate the real-world efficacy of the sensor.

CHAPTER 5: LIVE HUMAN EXPERIMENTATION

5.1 Introduction

The pinnacle of device feasibility, for any novel medical device, is successful testing in live human patients diagnosed with a disease of interest. However, to reach this step, it is crucial to demonstrate successful experimentation in pre-clinical models, including benchtop validation, animal model experiments, or cadaveric model simulation. In this thesis, Chapter 1 through Chapter 4 described the safety, efficacy, and feasibility of the stroke sensor using a variety of laboratory and cadaveric experimental models. Following successful validation of previous checkpoints, this chapter describes the results of first-in-man clinical testing of the stroke sensor.

At this point in the iterative design process of the stroke sensor, the main outcomes of interest included accuracy in detecting lesion location and ability to differentiate between ischemic and hemorrhagic stroke subtypes. As such, a prospective cohort study was conducted to recruit stroke patients in a blinded fashion.

5.2 Study Design and Protocol

IRB approval was obtained at the Keck School of Medicine of the University of Southern California. Inclusion criteria included all patients aged 18-80 who had experienced a TBI, hemorrhagic stroke, and ischemic stroke, in addition to normal volunteers. Pregnant women, neonates, prisoners, children, and institutionalized individuals were all excluded from this study. Also, patients with neurological diseases, neurological cancer, medical implants near the head,

metal implants, or previous strokes/TBI were excluded from the study. These criteria applied to both healthy volunteers and individuals with stroke/TBI.

The study was designed as a prospective, non-randomized, blinded proof-of-concept study to assess alternative methods of stroke subtyping, TBI detection, and imaging in a perioperative setting using non-invasive inductive-damping sensors. For control participants, the device was used to collect data, and our results will be compared to that of the standard imaging. The device was not used for clinical decision making and was used in conjunction with the normal standard of care. The device resembled a headpiece, as described in the previous chapter, and the sensor was moved over the headpiece several times to fully scan and image the patients' head. Healthy volunteers were entirely recruited through word of mouth, and received scanning with our device. However, they did not receive MRI or CT scanning. The purpose of including healthy controls was to: 1) better understand where healthy control values lie in a healthy brain, 2) determine how vascular variability influences conductivity variability in a healthy brain and, 3) acquire control data to facilitate differential scanning to amplify signal in stroke/TBI patients. Controls were also between 18 and 80 years old.

Patients experiencing stroke symptoms were admitted and given a workup according to the traditional standard of care. Imaging studies were conducted (CT scanning) to determine the location, depth, volume, and type of injury in accordance with the normal standard of care. Immediately after imaging, the test device was used to collect data, and the results were compared to that of the standard imaging. The test device resembled a headpiece similar to the aforementioned device. Patient files were accessed to view CT scans and compare them to the images produced by the device.

Adverse event data collection and reporting, which are required as part of every clinical trial, were performed to ensure the safety of all subjects enrolled in the studies as well as those who will enroll in future studies using similar devices. Adverse events were reported in a routine manner at scheduled times during a trial. Additionally, certain adverse events were required to be reported in an expedited manner to allow for optimal monitoring of patient safety and care. Of note is that the only anticipated adverse event possible as a result of participating in this study was discomfort from wearing the hat sensor. The original data collection forms and all other study documents were kept in secure file cabinets in the allocated office and clinic space. These offices had limited access and were only available to authorized personnel. At the time of registration, signed and dated copies of the patient Informed Consent with the Human Rights and the HIPAA authorization were given to each patient. Institutional policy regarding distribution and location of original consent documents were fully followed. The original form was kept in the patient research chart maintained by the research coordinator.

5.3 Hemorrhagic Stroke Detection

Using the same technique described above in scanning the head model, a wearable head cap with eight equidistant scanning paths was developed for live human testing at the Keck Hospital of USC. The entire process—which included obtaining consent, positioning each patient, and scanning with the sensors—took roughly 15 minutes from start to end for each participant enrolled in our study (n=8).

Patient #1 was a 32-year-old woman who presented with left-sided hemiparesis and placed on stroke protocol. CT imaging showed a 15cc lesion in the right basal ganglia with the presence of moderate right intraventricular hemorrhage (IVH) (Figure 5-1a). Large, medium, and small coils

were all used to collect data from the patient at bedside following CT imaging and all necessary stroke interventions. Two-dimensional (Figure 5-1b) and three-dimensional (Figure 5-1c) images of the lesion were produced. Both the 2D and 3D images produced by the sensor corroborated the presence of a hemorrhage in the right lobe of the patient, and the range of the large coil (4.97cm) allowed it to detect the right IVH. Both the small and medium coils were unable to detect the IVH likely due to their shorter scanning ranges, demonstrating their ability to provide depth information (Figure 5-2). By interpreting the readings of the coils, we predicted that the IVH was between 4.97cm and 3.99cm from the surface of the skull, which was the confirmed depth range of the IVH at the right occipital horn of the lateral ventricle.
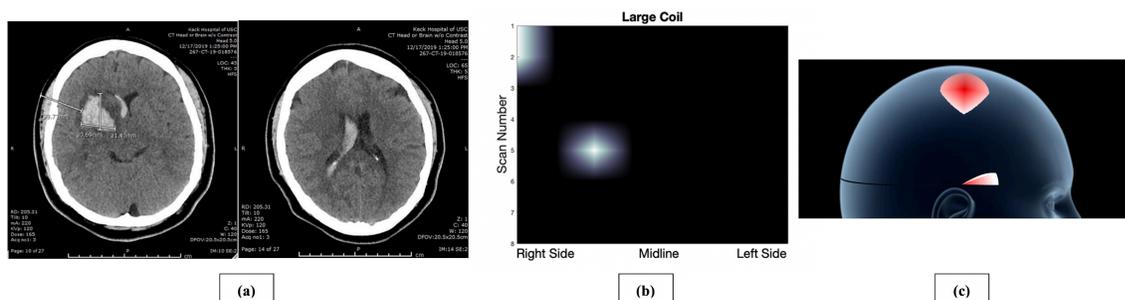
Figure 5-1: a) CT imaging showing a right basal ganglia ICH and associated IVH. b) Two-dimensional data gathered from the ECD sensor. Of note, the Large Coil has the largest magnetic field depth, and thus was able to detect both hemorrhages. c) Three-dimensional projections of each coil. 3D graphics can be created in real-time to rapidly guide clinical judgement and reduce time-to-treatment.
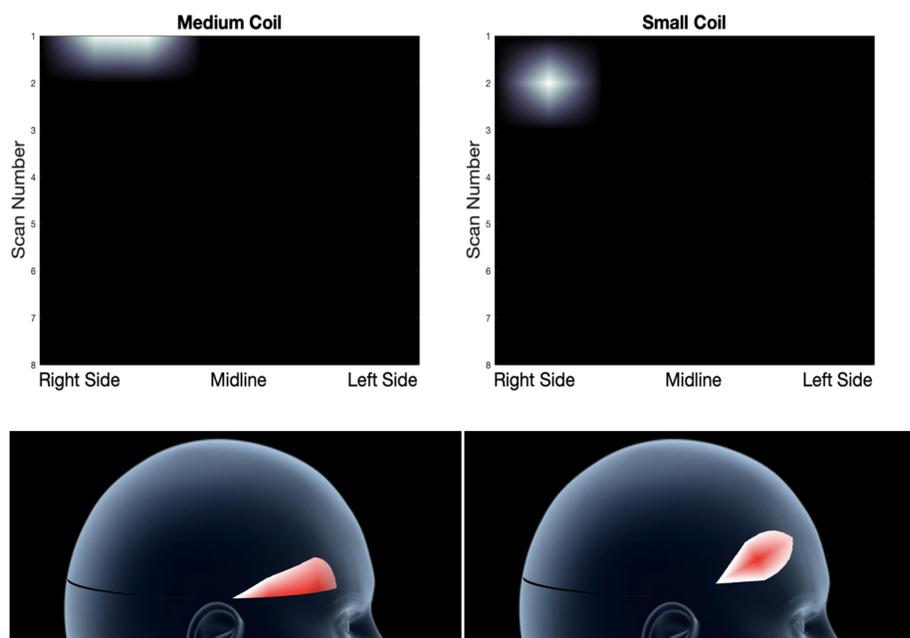
Figure 5-2: 2D and 3D output for medium and small coils. While only the large coil is used for image production, the medium and small coils provide information regarding lesion depth, which can be seen in this example. While both coils pick up the larger basal ganglia hemorrhage, they both fail to detect the IVH. However, IVH was detected by the large coil with the deeper scanning depth.

Patient #2 was a 78-year-old man who presented with right hemiparesis and loss of consciousness. CT imaging showed an 80cc left parietal lobar hemorrhage. Scanning with the large ECD sensor was performed, and image production corroborated the findings of the CT image (Figure 5-3). Comprehensive scanning with the medium and small coils can be seen in Figure 5-4.
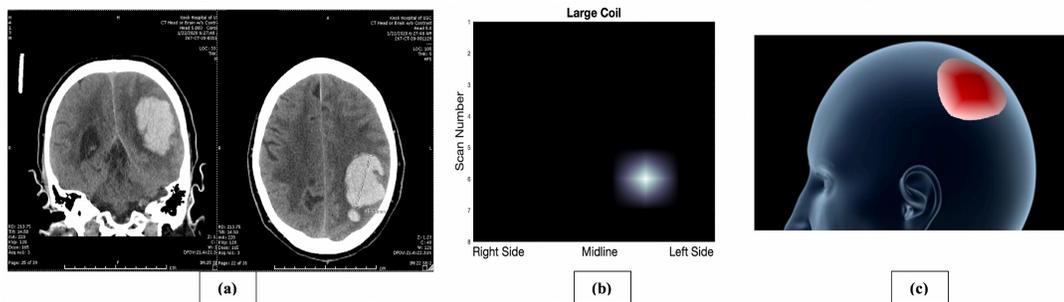
Figure 5-3: a) CT imaging showing a left parietal lobar ICH b) Two-dimensional data gathered from ECD sensor scanning. c) Three-dimensional projections of the lesion.
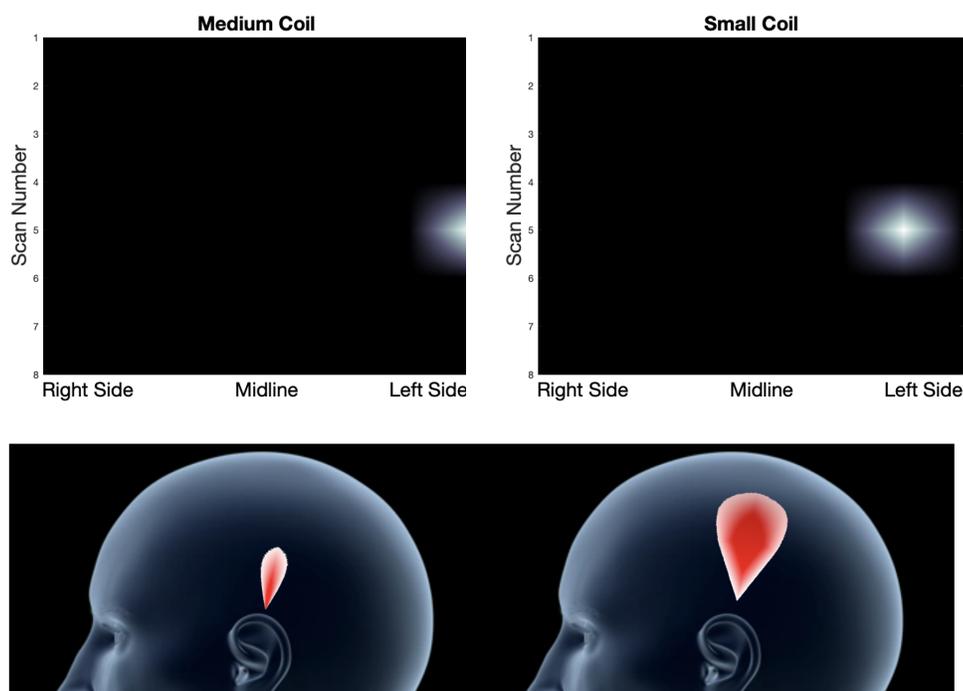
Figure 5-4: 2D and 3D output for medium and small coils. The relative similarity between these scans and the large coil confirms that the bleed extends superficially and can be detected by all coils.

Patient #3 was a 71-year-old woman with sudden onset loss of consciousness and coma. CT imaging revealed severe bifrontal, right greater than left ICH and subarachnoid hemorrhage (SAH) due to an aneurysmal rupture. Scanning with the ECD sensor revealed a diffuse hematoma, with the largest region of bleeding located in the right frontal lobe (Figure 5-5). Due to the diffuse nature of her ICH, the ECD sensor was able to best detect the bleed at the area of maximum hemorrhage, as seen in the 2D and 3D images generated from the large coil. Both small and medium coils were able to locate the hemorrhage near the area of maximum hemorrhage but failed to locate smaller regions of bleeding due to limited scanning depth (Figure 5-6).
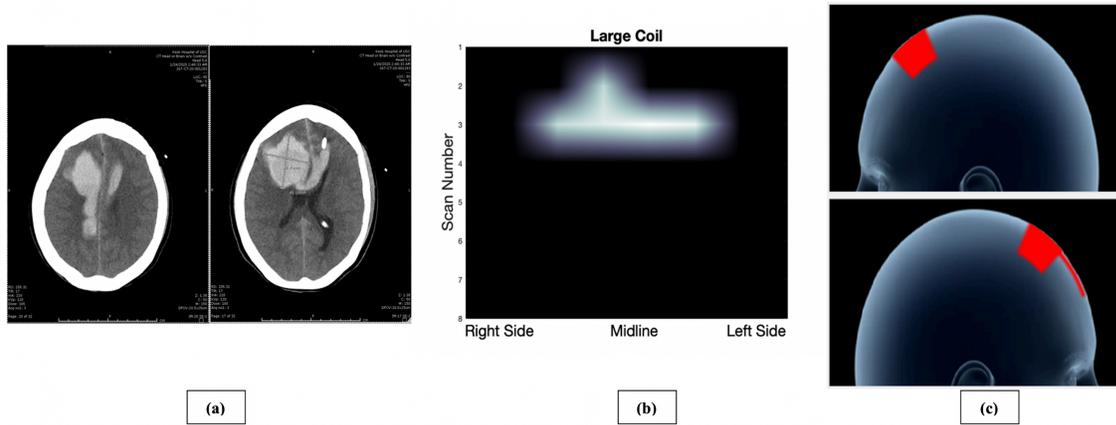
Figure 5-5: a) CT imaging showing bilateral ICH, right greater than left b) Two-dimensional data gathered from ECD sensor scanning. c) Three-dimensional projections of the lesion. The lesion crosses the midline, so two images are provided with left (top) and right (bottom) profiles.
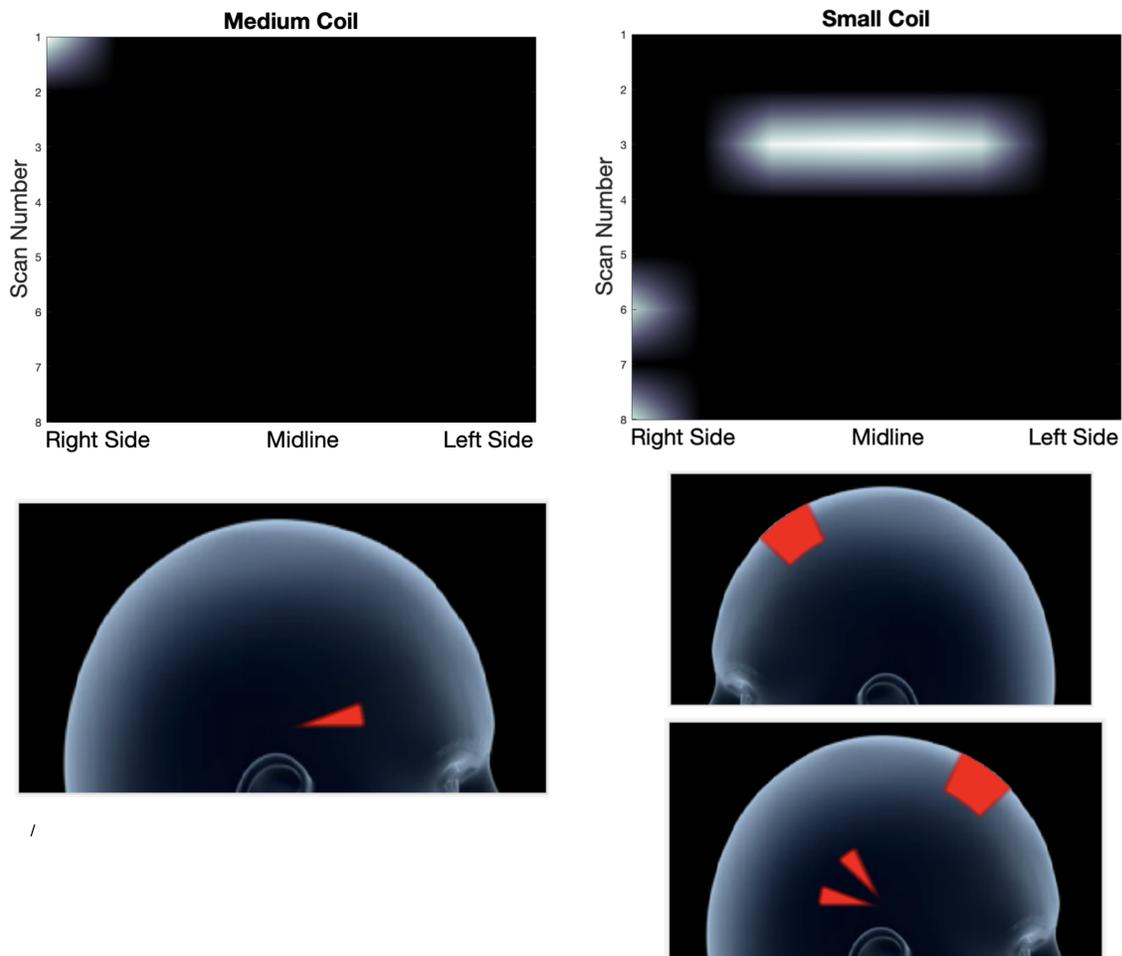
Figure 5-6: 2D and 3D output for medium and small coils in the setting of a large SAH. Both coils (especially the medium coil) produce the largest signal at the point of maximal hemorrhage diameter or at points that extend superficially.

5.4 Ischemic Stroke Detection

Patient #4 was a 50-year-old man with right arm weakness and aphasia, who presented with a left middle cerebral artery (MCA) occlusion, resulting in developed regions of infarct and edema on CT imaging (Figure 5-7a-c & Figure 5-8). The ECD sensor successfully localized the area of infarct to the left temporal and frontal region.

Patient #5 was a 77-year-old man with left hemiparesis and a large right MCA territory infarct on CT imaging. Scanning with the ECD provided localization of the lesion, shown in Figure 5-7d-f. Additional scans with medium and small coils are provided as Figure 5-9.
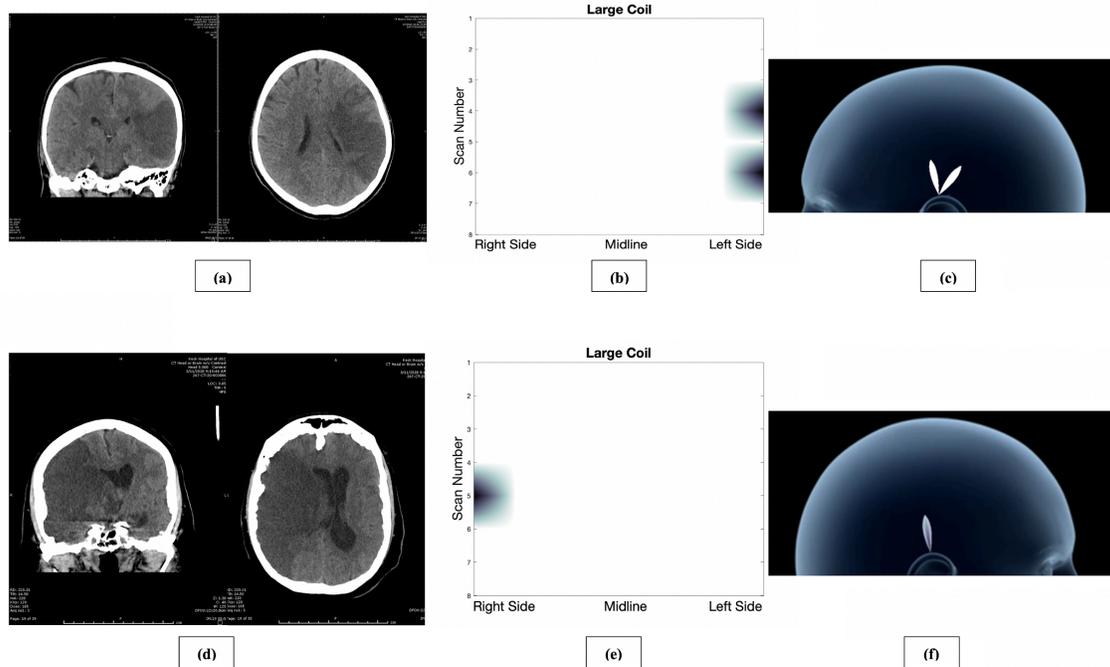
Figure 5-7: a) CT imaging showing left MCA ischemic stroke. b) Two-dimensional data gathered from ECD sensor scanning from Patient #4. c) Three-dimensional projections of the maximal point of the lesion. d) CT imaging showing right MCA ischemic stroke. e) Two-dimensional data gathered from ECD sensor scanning from Patient #5. f) Three-dimensional projections showing the maximal region of the ischemic lesion.
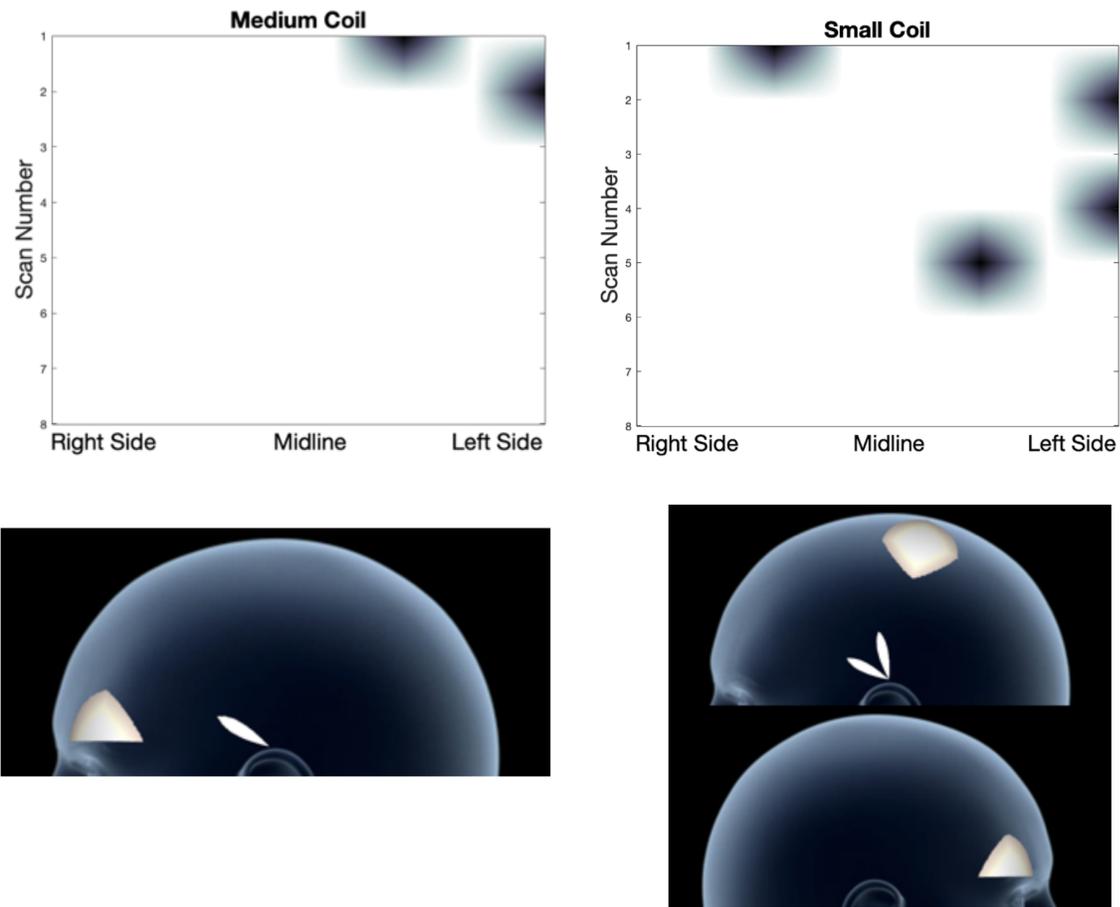
Figure 5-8: 2D and 3D output for medium and small coils in the setting of a left MCA occlusion. While the large coil is more sensitive to areas of ischemia (hence why it is used for image production), the small and medium coils both suggest that the left MCA might be involved per the signal generated above the left ear.
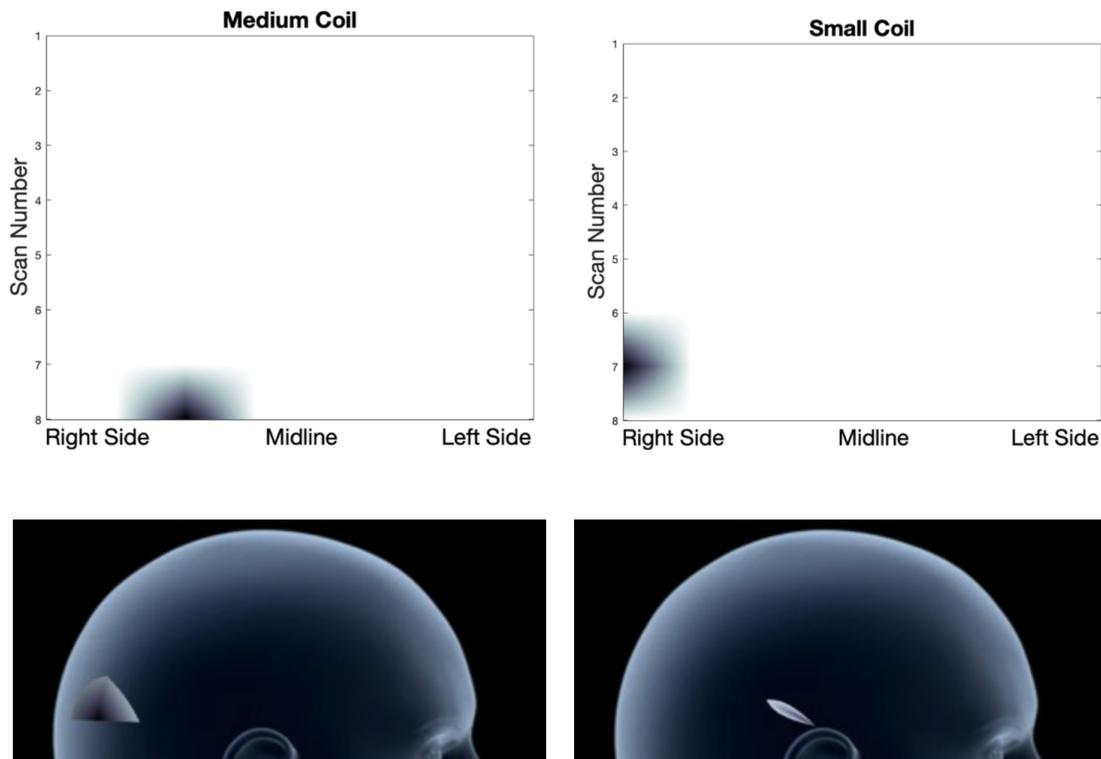
Figure 5-9: 2D and 3D output for medium and small coils in the setting of a right MCA occlusion. While the large coil is more sensitive to areas of ischemia (hence why it is used for image production), the small and medium coils both suggest that there might be areas of ischemia on the right side of the patient.

Although both infarcts occupy large cortical stroke territories in both patients, the images produced from the ECD sensor highlight the area of maximal ischemia, which in both cases happens to be just above the ear ipsilateral to the lesion. This phenomenon is explored in Chapter 6, but is likely due to the magnitude of ECD occurring as a result of larger conductivity regimes at the maximum diameter of the lesion. In addition, filtering algorithms developed to remove noise

from the images may confuse areas of lower conductivity with noise, thus reducing signal intensity in these regions.

5.5 Future Advancements

While the feasibility of the stroke sensor has been demonstrated in distinguishing ischemic and hemorrhagic stroke variants, future research is planned to efficiently distinguish between subtypes. Several deep learning algorithms may be used to develop automated disease classification guidelines. To develop the most powerful classification algorithm, statistical measures of performance (specificity, sensitivity, positive predictive value, and negative predictive value) of both support vector machines (SVMs) and neural networks (NN) must be gauged. SVMs are non-parametric models that use maximal margins and kernel weighting to identify unique, predictive features in a training set. NNs are parametric algorithms that contain multiple hidden layers capable of pinpointing identifying characteristics of a training group. Furthermore, it may be possible to explore the realm of unsupervised machine learning, including methods such as principal component testing and k-cluster analysis. Specifically, multilayered perceptron (MLP) models may show the greatest promise in using conductivity values to differentiate between normal brain, ischemic stroke, hemorrhagic stroke, and TBI. The successful use of MLP in radiographic image analysis has been demonstrated in several studies, and it has even been used to differentiate glioblastoma from primary central nervous system lymphoma on MRI [94]. To develop training sets, conductivity measurements from each disease group may be processed in MATLAB and separated into their own datasets. These datasets can be fed into the model for training, and as prospective testing continues, testing sets will be established and fed into algorithms to gauge accuracy. Confusion matrices and statistical testing will be used to evaluate predictive value of our models.

Furthermore, the main outcome measure to demonstrate the efficacy of the ECD sensor is a receiver operating characteristic (ROC) curve, with a corresponding area under curve (AUC) value. Such a curve may be constructed by collecting additional patient data and comparing sensor outputs directly to data

obtained from CT imaging. A ROC curve with a high AUC is desirable, as this indicates high device sensitivity to strokes.

In order to achieve either of these future goals, a high number of patients must be recruited and analyzed. Future advancements are geared towards software development and improvement of circuit SNR.

5.6 Conclusion

The stroke sensor is shown to safely and accurately provide information regarding stroke subtypes in live human patients diagnosed and admitted to the hospital with a stroke. In addition, continuous scanning allowed for accurate imaging of the patient brain and lesion, providing additional information necessary for clinical decision making and operative planning. Future advancement may be aimed at developing automatic stroke subtyping and detection through the use of machine learning algorithms once a large pool of patient data is secured. Through such advancements, the time-to-diagnosis may be further reduced, and sensor accuracy may improve through model creation.

CHAPTER 6: COMPUTATIONAL MODEL DEVELOPMENT

6.1 Introduction

Computational model generation represents an important tool for feasibility studies and study optimization, especially when designing and testing complex devices or methodologies. As such, computational models in neuroscience have gained a great deal of traction because they allow rapid prototyping and testing without the need for live human subjects, thereby reducing the risk of patient harm while advancing the device's iterative designing process [95, 96]. In addition, computational models allow for theoretical testing of completely novel devices, highlighting yet unexplored avenues for device production [97, 98].

Our aim in this chapter is to develop computational models to evaluate the feasibility of microtesla-level magnetic brain scanning, including detection of ICH. The current paradigm for ICH detection involves either MRI or CT imaging, both of which involve expensive and non-portable equipment [99–101]. ICH involves relative increases in local blood concentration compared to steady state, non-active brain, and wearable medical devices capable of detecting local changes in blood concentration may facilitate rapid prediction of hemorrhage. Here, we use finite element modeling (FEM) software to develop computational models for a wearable electromagnetic device capable of detecting hemodynamic changes within the brain.

6.2 FEM Methodology

Using COMSOL Multiphysics version 5.5 (COMSOL Inc., Burlington, MA), we generated both three-dimensional (3D) and two-dimensional (2D) models of hemodynamic changes within a human head model, in addition to one-dimensional (1D) modeling of magnetic field decay as a function of distance. Text files of coordinate data from MRI head scanning were imported as an interpolation curve and organized in sectionwise format, and lofting of the closed curve allowed for the generation of a solid object roughly 20 cm in height and 10 cm in width [102, 103]. A novel material with a density of 2000 kg/m^3, electrical conductivity of 0.4 S/m, relative permeability of 1, and relative permittivity of 568 was added to simulate the properties of a human head. An ellipsoid with dimensions of 0.035 m in the a-axis, 0.045 m in the b-axis, and 0.025 m in the c-axis was added within the head to simulate the brain. A novel material with a density of 1000 kg/m^3, electrical conductivity of 0.2 S/m, relative permeability of 1, and relative permittivity of 827 was added to simulate the properties of the human brain. Lastly, a smaller ellipsoid with dimensions of 0.014 m in the a-axis, 0.018 m in the b-axis, and 0.010 m in the c-axis was added within the head to simulate an area of increased blood concentration. A novel material with a density of 1,060 kg/m^3, electrical conductivity of 0.65 S/m, relative permeability of 1, and relative permittivity of 3,030 was added to simulate an area of increased blood concentration [104, 105]. Using the simplified formula for intracerebral hemorrhage volume, which estimates blood volume as half the product of all three ellipsoid semiaxes (ABC/2), we determined our small ellipsoid to represent a local increase of 1.26 mL of blood [106–109]. This volume was decided because previous studies have established that local brain activation may increase local blood concentration by approximately 1.5mL [110].

Two scenarios were explored with reference to magnetic coil design: 1) a small handheld coil with 12.1 cm external diameter that could be moved across the head and 2) a larger coil with an

external diameter of 27 cm that resembles a headband and is placed on the head circumferentially. Both scenarios shared the following parameters: peak current of 0.0027 amperes, 6 coil turns, coil width of 4.2 cm, and material properties including copper wire with a density of 8960 kg/m^3, electrical conductivity of 5.998x10^7 S/m, relative permeability of 1, and relative permittivity of 1. An infinite element with the material properties of air and modeled as a sphere was added encapsulating the entire head and sensor model.

Ampere's Law was implemented to calculate the electric current density as the curl of the magnetic field. Electrical conductivity was modeled through Ohm's Law. Lastly, magnetization and dielectric models were included, which utilized the relative permeability and permittivity values respectively to solve their corresponding equations. Testing frequency was set at 1 MHz and a stationary solver was implemented and finite elements included in the model utilized fine meshing with a total of 286,184 degrees of freedom in the small coil and 314,478 degrees of freedom in the larger coil.

6.3 Model Results

Using Biot-Savart's Law, we can calculate the expected magnetic fields produced by both the small and large coils. These values can then be compared to those obtained through COMSOL modeling. For the smaller coil, the maximum magnetic field flux densities at the sensor (x=0) and 5 cm away from the sensor (x=5) are 0.1682μT and 0.0771μT respectively. For the larger coil, the maximum magnetic field flux densities at the sensor (x=0) and 5 cm away from the sensor (x=5) are 0.0754μT and 0.0622μT respectively.

We evaluated the magnetic flux density generated within a head model when a small solenoid coil was placed concentrically above an elliptical volume of increased blood

concentration. Both contour and volume plots are shown in Figure 6-1, where the microtesla-level

magnetic fields generated by the sensor are sufficient to generate magnetic flux within the volume

of blood, suggesting a measurable ECD signal is produced. In addition, the magnetic fields

generated within the head model are comparable to those calculated via Biot-Savart's Law,

suggesting that the computational model accurately represents the expected physical phenomena.
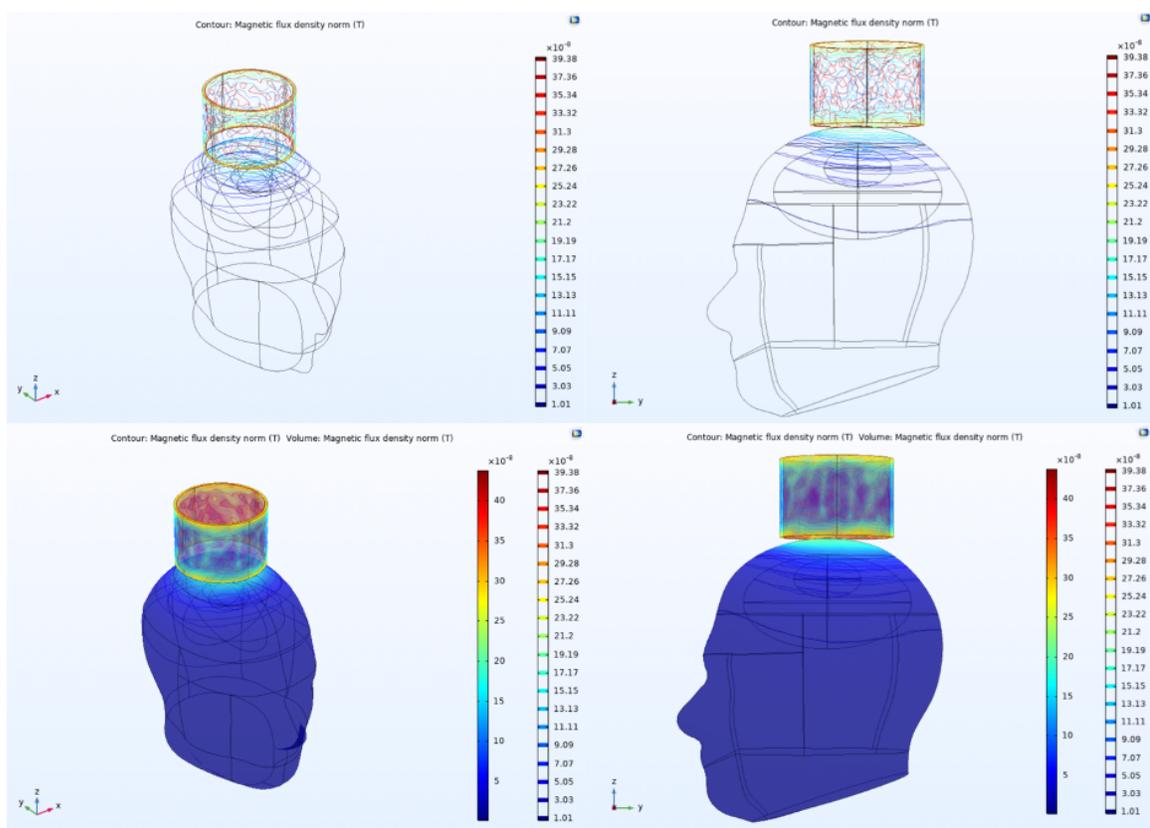
Figure 6-1: COMSOL multiphysics 3D simulations of the large coil on a human head model.

The 3D model was projected on a 2D surface to better visualize the magnetic flux density

profile generated by the small coil. As seen in Figure 6-2, the magnetic flux decays as a function

of distance, with the strongest magnetic flux being produced at the apex of the lesion. This finding

suggests that microtesla magnetic sensors may be most sensitive to the hemodynamic changes closest to the sensor. Furthermore, the magnetic flux density suggests that the greatest magnetic flux is generated when both the coil and volume of blood are concentrically placed.
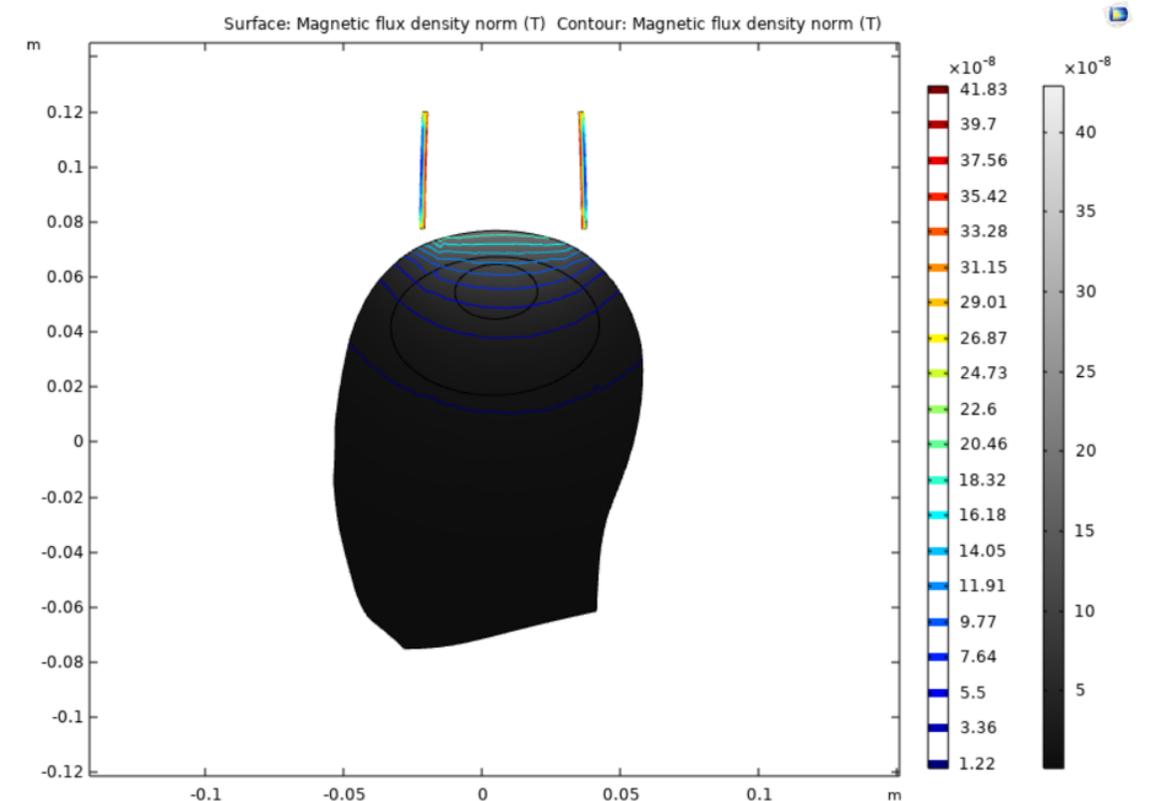
Figure 6-2: COMSOL multiphysics 2D simulation of the large coil on a human head model.

To investigate the effects of distance on magnetic flux density, the head model was used to generate the 1D plot seen in Figure 6-3. The bottom of the head is represented at x=0.0 m and the surface of the coil is represented at x=0.60 m, and the arc length used to generate this plot passed through the center of the head and coil model. As expected, the areas adjacent to the coil will produce the largest magnetic flux, which will decay as a function of distance. The ellipsoid representing the volume of blood was located roughly 5 cm away from the sensor (x=0.55) and from Figure 6-3 we would expect a magnetic flux density of roughly 0.07μT. Calculations using

Biot-Savart's Law predicted a magnetic flux density of $0.0771\,\mu T$ at 5 cm, supporting the accuracy

of our model.
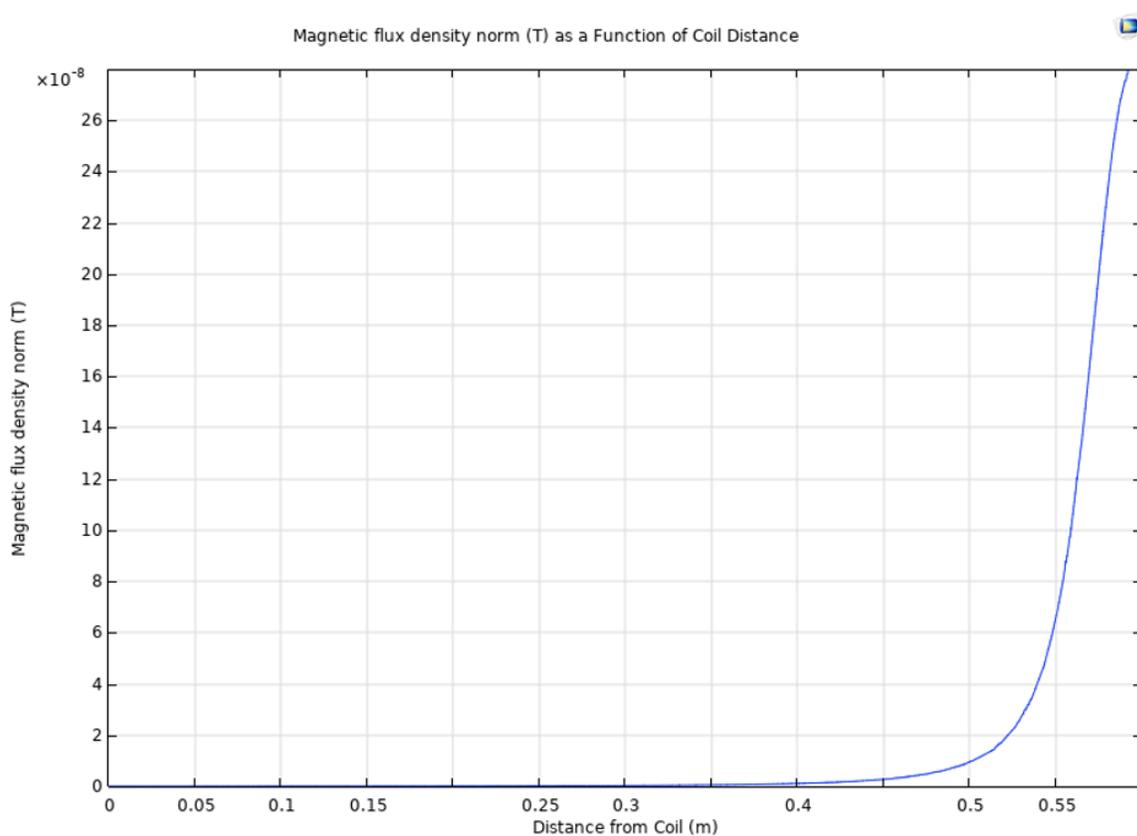
Figure 6-3: COMSOL multiphysics 1D simulation of the large coil on a human head model.

The 3D model was generated with the extra-large coil circumferentially wrapping around

the head model. Both contour and volume plots are shown in Figure 6-4. The extra-large coil elicits

a higher degree of magnetic flux within the head model. However, due to the high degree of head

surface area scanned by the circumferential design, most of the magnetic flux density changes, and

thus ECD signals, are produced by interactions with the tissue of the head and not the volume of

hemorrhage.
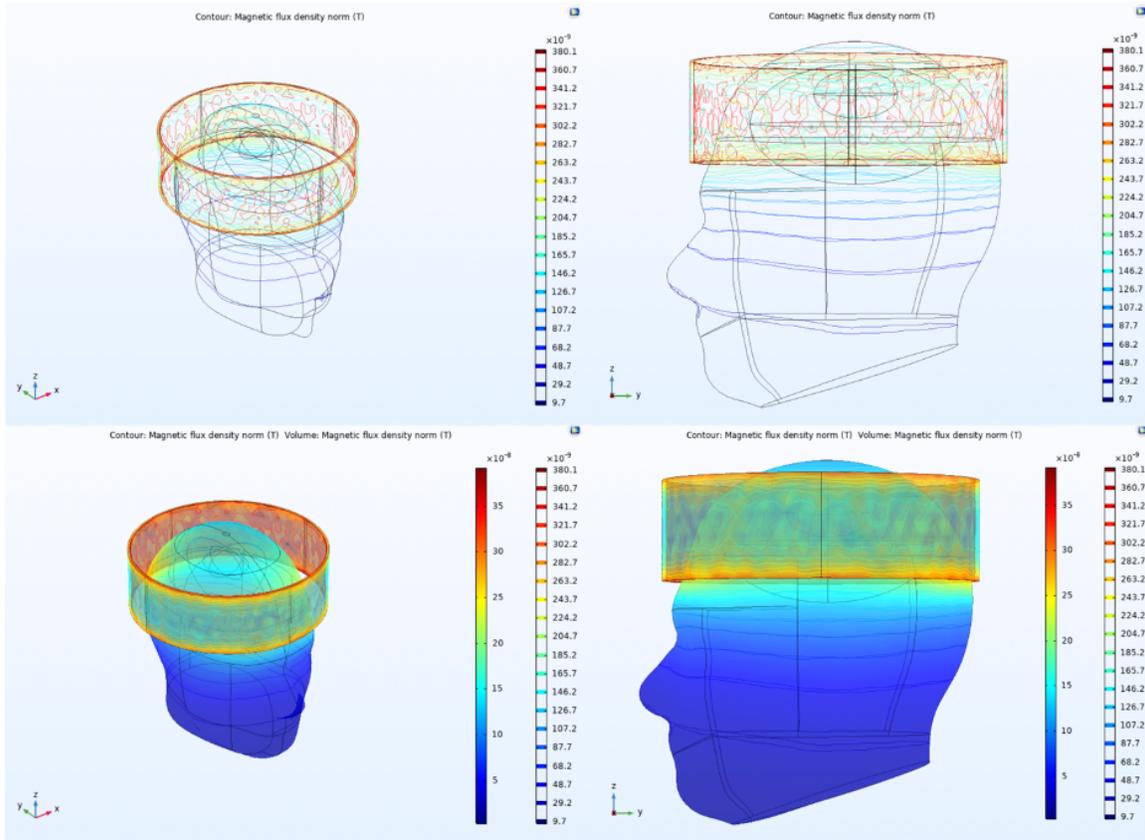
Figure 6-4: COMSOL multiphysics 3D simulations of the extra-large coil on a human head.

To investigate the large surface area interactions introduced by a circumferential design, a 2D projection of the 3D head model was developed. A uniform magnetic field is seen in Figure 6-5 throughout the entirety of the head model, with the greatest magnitude of magnetic flux at the edges closest to the coil. Further, little magnetic flux is seen within the elliptical blood model.
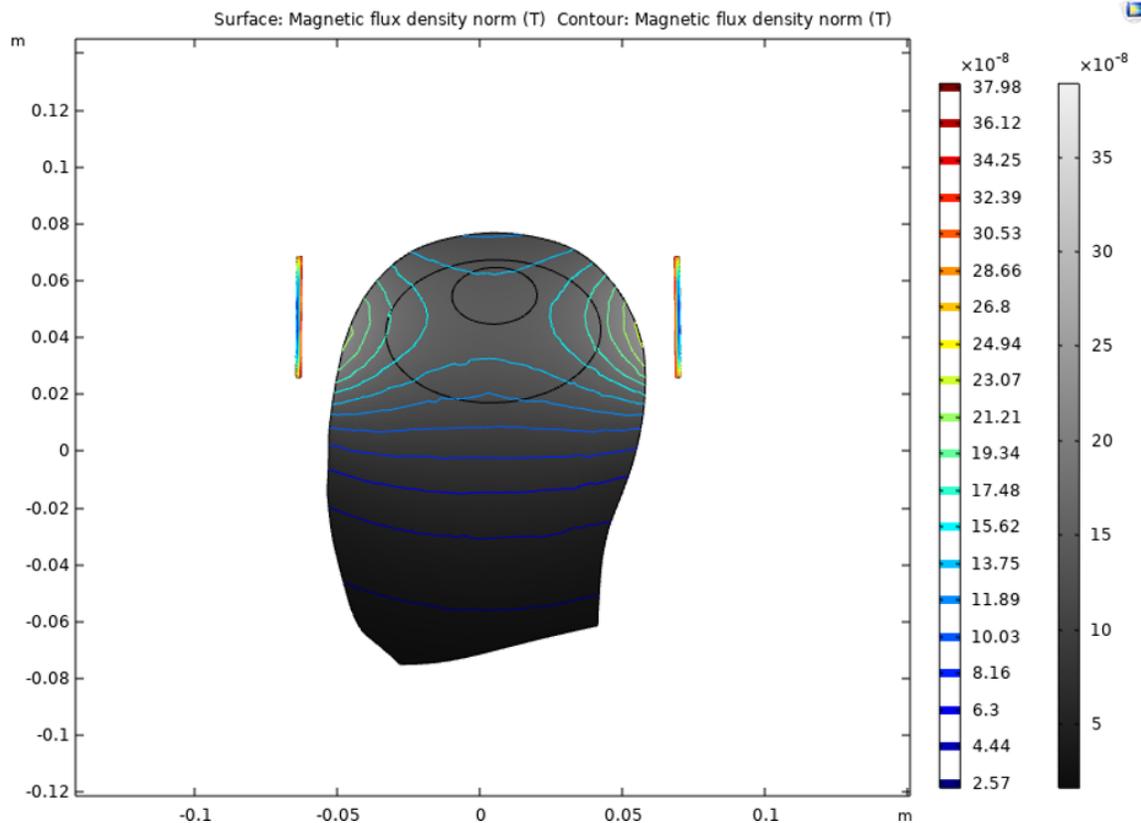
Figure 6-5: COMSOL multiphysics 2D simulation of the extra-large coil on a human head.

To investigate the effects of distance on magnetic flux density, the head model was used to generate the 1D plot seen in Figure 6-6. The bottom of the head is represented at x=0.0 m and the surface of the coil is represented at x=0.55 m, and the arc length used to generate this plot passed through the center of the head and coil model. Interestingly, the maximum magnetic flux density produced by the extra-large coil was lower than that of the large coil, consistent with our Biot-Savart calculations.
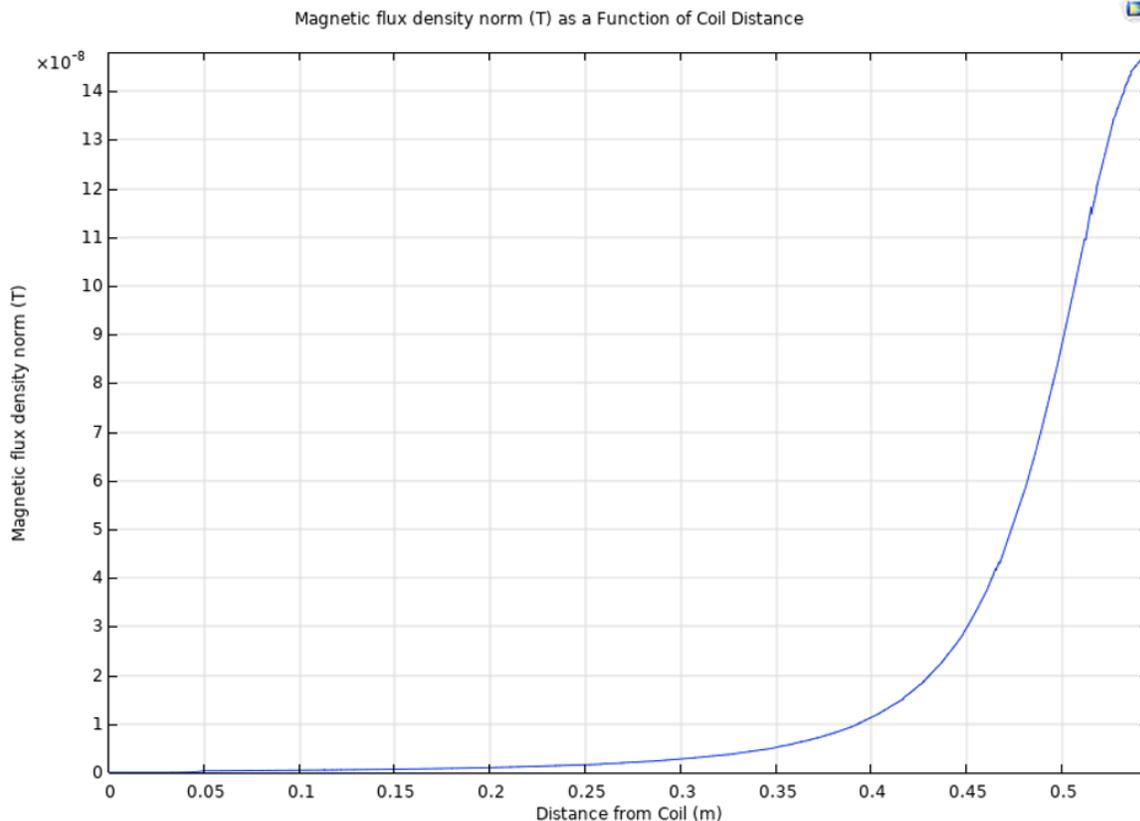
Figure 6-6: COMSOL multiphysics 1D simulation of the extra-large coil on a human head.

6.4 Model Interpretation

The benefits of low-energy portable magnetic coils for brain scanning are quite clear in the realm of clinical neuroscience, neurology and neurosurgery. Current estimates suggest that the average time to treatment following ICH may be 2 hours because MRI/CT imaging is required prior to treatment to rule out ischemic stroke, localize hemorrhage location, and plan for neurosurgical evacuation [49–51]. During this time, the rate of neuronal death is constant, contributing to the high rates of morbidity and mortality classically seen following hemorrhagic stroke [52]. Translational portable medical devices capable of accelerating the time to treatment

in the field or at the patient bedside may potentially reduce the short and long-term complications following an ICH.

From our computational modeling, we can also determine that the use of microtesla-level magnetic brain scanning poses little to no physiological harm. MRI imaging and transcranial magnetic stimulation (TMS) devices typically operate on the order of several teslas and have achieved FDA approval with little potential for physical harm [111, 112]. As such, reduction of the SMF to the microtesla scale further reduces the risk of such a device. In addition, prior studies have established that EMFs in the millitesla range may interact with neuronal signaling, thus impairing walking in some experiments with locusts [113]. However, the threshold for physiological disturbances has been well studied and is believed to be set at 4mT for motor disturbances [113] and at 38mT for evoking miniature endplate potential (mepp) inhibition [114, 115]. Thus, the risk of adverse physiologic events or mepp disturbance is extremely low when using microtesla magnetic fields at 1MHz.

Not surprisingly, much of the sensor developments described in Chapters 1-5 are bolstered by the findings of the FEMs. Specifically, ICH detection and classification through the use of an ECD sensor is feasible on both computational and experimental models. In addition, the predicted and actual magnetic field magnitudes for each coil are quite similar, further strengthening the feasibility of the stroke sensor.

6.5 Conclusion

Computational models can be developed to test the feasibility of novel medical devices and facilitate device development without risk to human participants. Models generated for microtesla-level devices show that they may be able to detect hemodynamic changes within the brain as a

function of changes in magnetic flux density and ECD. These models almost exactly mirror the

experimental results described previously in this thesis.

CHAPTER 7: ADDITIONAL SENSOR APPLICATIONS

7.1 Introduction

In light of the coronavirus disease 2019 (COVID-19) pandemic, additional sensor considerations for the stroke sensor were investigated. We were curious to see if it would be possible to predict changes in pulmonary waveforms, volumes, and/or region-dependent conductivities using the large coil of the stroke sensor previously described. Additional sensor applications suggest that ECD-based sensors may be implemented in a variety of medical subspecialties for a variety of clinical diagnoses and conditions.

7.2 Respiratory Sensor Background

Pulmonary function testing (PFT) involves comprehensive evaluation of the lungs to provide objective and quantifiable metrics for pulmonary function. Oftentimes, PFTs are indicated when the clinician suspects obstructive lung disease, such as chronic obstructive pulmonary disease (COPD) and asthma, or restrictive lung disease, such as pulmonary fibrosis or sarcoidosis. In contemporary clinical practice, PFTs are most commonly performed using spirometry, and occasionally with lung plethysmography [116–118]. However, the American Thoracic Society and many comparable international societies have recommended postponing PFTs during the COVID-19 pandemic, due to the high risk of COVID-19 transmission during the outpatient testing visit [119–123]. While these restrictions were put in place through expert guidance to prevent the spread of disease, they have made it difficult to gauge pulmonary function in patients with previously

diagnosed lung disease as well as those recovering from COVID-19 pneumonia who require close follow-up examination.

As such, wearable continuous pulmonary biosensors may play a unique role in evaluating pulmonary function without requiring direct inpatient or outpatient examination. In fact, several pulmonary biosensors have been previously described in the literature. Devices utilizing accelerometers have been shown to accurately characterize the respiratory waveform through anteroposterior displacement of the thorax during breathing [124]. Other groups have developed acoustic-based sensors that monitor air movement near the nose, or air moving through an airway, to monitor respiration [125, 126]. Similarly, mechanical strain sensors, placed on the chest like a piece of tape, have been implemented by some groups to accurately measure the respiratory waveform in addition to approximation of non-statistically significant ratios of forced expiratory volume in one second (FEV_1) and forced vital capacity (FVC) [127]. However, many of these sensors are unable to accurately gauge respiration volume and relevant pulmonary metrics, and strain-based sensors require calibration and tight contact with the patient's skin to yield accurate results.

With current limitations in mind, our group describes the development of a non-contact, wearable, and continuous pulmonary function sensor capable of detecting both respiratory waveforms and volumes. The sensor relies on the generation of microtesla-level magnetic fields and the ECD phenomenon to track changes in conductivity during the respiratory cycle. As non-conductive air enters the lungs during inspiration, local measured conductivity decreases; conversely, expiration decreases the anteroposterior dimension of the chest, putting the sensor in closer proximity to conductive vasculature and tissue within the thoracic cavity. We demonstrate that our wearable electromagnetic sensor is safe and can continuously measure relevant pulmonary

function with a high degree of accuracy through clothing. Additionally, implementation of conductivity-based scanning allowed for crude imaging of the thoracic cavity due to the wide range of conductivities of organs contained within. The development of such a device may allow for efficient non-contact PFTs during the COVID-19 pandemic, provide relevant respiratory metrics for remote clinical assessment, and monitor conductivity changes within the lungs resulting from edematous or inflammatory lung pathologies.

7.3 Respiratory Sensor Testing Methodology

For our experiments, we constructed a solenoid coil with an outer diameter of 11.4cm and 6 turns out of 46 AWG Litz wire. The coil was wound around a non-conductive plastic scaffold and connected to the Texas Instruments LDC 1101 inductance-to-digital converting chip [81]. Non-destructive techniques based on the ECD phenomenon are widely used to test the presence, quantity, and integrity of various conductive materials, most commonly metals [79]. Eddy currents generated by a conductive material flow in the direction that decreases coil inductance and coil parallel resistance (R_p), which may be used to quantify the degree of ECD produced. As a result, this change in resistance then becomes proportional to the conductivity of the material placed in front of the sensor.

The sensor was designed to have a resonant frequency at 1 megahertz (MHz), which was confirmed through analysis with the LDC 1101 graphical user interface (GUI). In order to minimize capacitive coupling and reduce the noise of our sensor, we covered the lateral sensor border with thin ferrite sheets, leaving the end facing the target unshielded. The use of magnetic shielding with ferrite material helped to redirect the magnetic field distribution toward the target and block the electromagnetic interference from external sources. The average relative

permeability of the ferrite sheet (MULL12060-000, Laird Technologies Inc.) is approximately 135 from 1MHz to 10MHz, which encapsulates the frequency range used in this study [84]. Prior to testing, the sensor sampling rate was found to be 6,660 Hz and the signal-to-noise ratio of the sensor was found to be 9.4. Characterization of the sensor magnetic field using both Biot-Savart's law (0.1786μT) and multiphysics modeling (0.1μT) confirmed a magnitude of several microteslas.

All data was converted into digital signals using the inductance-to-digital converting chip and stored on a local laptop for analysis in MATLAB. Savitzky-Golay and simple Gaussian filters from the Signal Processing Toolbox were implemented to smooth the respiratory time series waveforms and to remove high frequency noise. Local maxima and minima were located within the respiratory diagrams and the difference between the peaks and troughs were averaged for each individual trial, yielding the average change in R_p per breath. The total number of breathing cycles within the data, defined as one inhalation paired with one exhalation, as well as the scanning time were utilized to predict the respiratory rate of volunteers according to the following equation: [60 Seconds]/[Scanning Time (Seconds)]*[Number of Cycles]. Sensor calibration was not required prior to scanning volunteers to achieve the results described in this study.

Using COMSOL Multiphysics version 5.5 (COMSOL Inc., Burlington, MA), we generated two-dimensional (2D) models of magnetic flux density changes within the magnetic field space when the chest is placed near the sensor. All models utilized a peak current of 0.0027 amperes, 6 coil turns, diameter of 11.4cm, and material properties including copper wire with a density of 8,960 kg/m^3, electrical conductivity of 5.998x10^7 S/m, relative permeability of 1, and relative permittivity of 1. The skin/bone (0.4 S/m) and underlying vasculature (0.65 S/m) were modeled with appropriate electrical conductivity values.

IRB approval was obtained at the California Institute of Technology (IRB Number: 20-1005) for non-randomized human feasibility testing of the respiratory sensor. All participants tested negative for COVID-19 before data collection, and patients with any pulmonary pathology were ineligible for recruitment. Consent and scanning data were obtained by S.S., and a total of 4 participants were recruited (two participants tested twice). Each participant was asked to lay prone on a non-conductive surface while 8 vertical scans were obtained across the chest. In addition, the patient's chest was recorded with the sensor while sitting straight up. In all trials, participants were instructed to breathe through their nose with regular, non-labored respiratory rhythms. It was ensured that each patient was not wearing any metallic items (jewelry, clothing, etc.) and that the immediate surrounding was void of any metallic items to minimize interference with the electromagnetic sensor.

The Medical International Research (MIR) Spirobank II® spirometer was utilized to record baseline PFTs for each volunteer in the study according to instructions of use. Spirometry was recorded immediately following scanning with the sensor. This device was utilized to obtain the FEV_1 and FVC of each participant to compare with the results obtained with the ECD sensor described in this study.

The anterior chest was scanned using 8 equidistant vertical scanning paths, starting at the left midaxillary line to the right midaxillary line. The length of each scan spanned from the lower rib border up to the clavicles/sternal notch. Data from the sensors was filtered to remove high frequency noise. The data collected from each row was down-sampled from >50,000 data points collected during scanning to eight averaged points. We use the eight data points from the eight scanning rows to create an 8x8 interpolated conductivity heatmap of the chest, with brighter areas

indicating higher probability of more conductive organs or regions and darker areas indicating a higher probability of air or non-conductive tissue.

Basic demographics and relevant values were visualized using GraphPad Prism 8. Statistical analysis was performed in MATLAB and aimed to establish the accuracy of sensor resistance values in predicting pulmonary volume changes. Specifically, regression analyses were performed to investigate the correlation between spirometry, respiratory rates, and ECD sensor values. Both p-values and R-squared values were reported for each regression model to evaluate goodness-of fit. P-values <0.05 were considered statistically significant.

7.4 Respiratory Sensor Results

Chest movement produced with inspiration and expiration displaced the sensor in the anteroposterior direction with the chest wall, with each inhaled breath replacing conductive tissue and vasculature within the sensor magnetic field space with non-conductive room air. Eddy currents generated due to the decrease in local conductivity during inhalation resulted in increased R_p measurements taken by the chip (Figure 7-1A). Upon exhalation, non-conductive air in the lungs is released and the corresponding reduction in chest diameter brings conductive tissue back into the range of the sensor, thus increasing eddy currents and decreasing R_p measurements (Figure 7-1B).
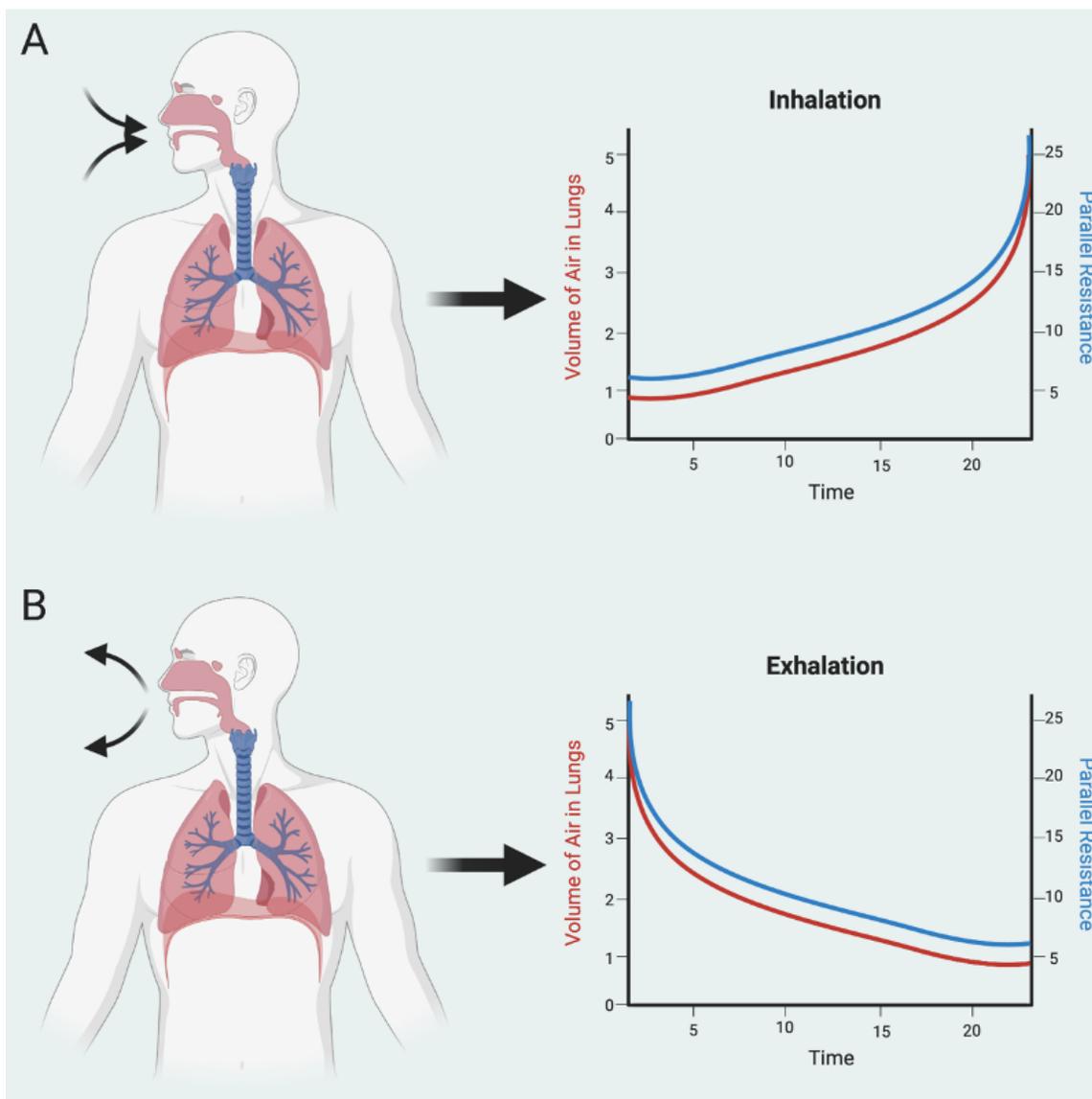
Figure 7-1: Correlation between resistance and lung air volume. **A**, As the volume of air in the lungs increases during inhalation, so do the parallel resistance values queried by the sensor. This is because room air is non-conductive, resulting in reduced eddy current damping and thus, increased parallel resistance. **B**, Conversely, exhalation decreases the volume of air within the thoracic cavity, reducing lung air volume and parallel resistance. Created with BioRender.com

In contrast to similar biosensors that require calibration or tight contact with the individual to produce accurate results, our pulmonary sensor required no calibration and generated pulmonary

waveforms through the shirt after being freely placed on the chest of participants (Figure 7-2A). As such, the anteroposterior motion of the chest during the breathing cycle results in a sinusoidal change in coil R_p, which is converted to digital signals and stored on a local computer for analysis.

Through signal processing and smoothing, it is then possible to generate an approximate respiratory waveform using the sensor. By subtracting the lower R_p resulting from expiration from the higher R_p resulting from inspiration, it is possible to approximate the amount of signal generated from each breath (Figure 7-2B). This change in resistance is directly proportional to the amount of ECD generated or lost with each exhalation or inhalation, respectively. Changes in R_p for each breath may then be averaged across the respiratory time-series of participants to yield the mean change in R_p per breath.

The sensor architecture developed for this application consists of a sensor coil paired with a capacitor to form an electrical resonant circuit, which is significantly different from the architecture of previous ECD sensors used in industry for metal detection and crack inspection consisting of a bridge circuit that measures the sensor coil impedance [79]. Opting for the simplest sensor achievable, our device is constructed from 6 loops of Litz copper wire wound as a solenoid on a plastic scaffold connected to a commercial inductance-to-digital converter for digital readout into a local computer (Fig. 2C).

When the sensor is brought in close proximity with a conductive material, such as the heart, aorta, liver, and vessels of the chest, the magnetic field generated within the solenoid coil will generate eddy currents in the target, which will produce a counteracting magnetic field resulting in a decrease in coil inductance and R_p (Figure 7-2D). The magnitude of counteracting magnetic fields is directly proportional to the conductivity of the target material and the orthogonal distance

between the sensor and the target [82]. Because lung pathology is characterized as either obstructive or restrictive, changes in the pulmonary time-series waveform generated by such a sensor may provide clinically relevant patterns aiding in diagnosis following alveolar damage (Figure 7-2E). Continuous monitoring over long periods of time may be able to detect slow progression of lung disease using non-contact methods, which is particularly of interest for specific lung pathologies including pulmonary fibrosis and COVID-19 acute respiratory distress syndrome (ARDS).
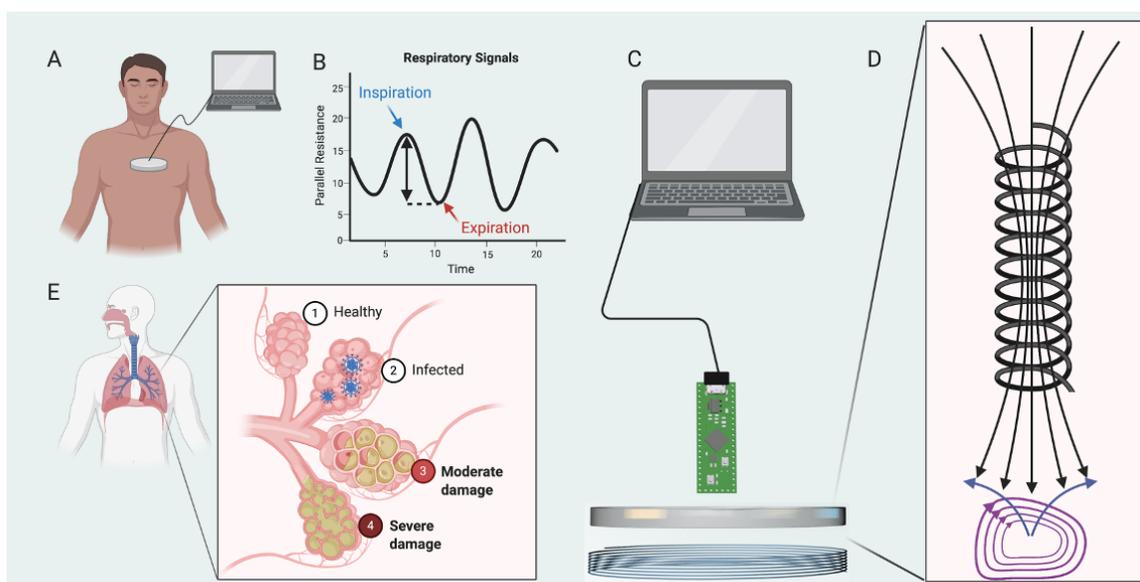
Figure 7-2: Experimental setup and sensor principles. **A**, During static pulmonary testing, the sensor is placed on the mid-chest, with data recorded and stored on a local computer. **B**, Fluctuations in parallel resistance during scanning result in a sinusoidal time-series waveform, with inspiration resulting in local maxima and expiration resulting in local minima. The difference between maxima and minima yield parallel resistance changes per breath. **C**, The sensor is constructed as a solenoid with 6 turns on a plastic scaffold connected to a commercial inductance-to-digital converting chip which is powered via a USB connection. **D**, The magnetic field generated by the solenoid induced eddy currents within the target proportional to target conductivity, which produce counteracting magnetic fields that influence coil resistance. **E**, Alveolar damage, following COVID-19 for example, presents with varying degrees of damage which may present differently. Early-stage pulmonary dysfunction may be queried with such a sensor. Created with BioRender.com

To determine the respiratory waveform and respiratory rate (RR) of participants, 15-25 seconds worth of data was recorded from the sensor while it was placed directly on the sternum (Figure 7-2A). Other scanning sites on the chest were investigated, but placement on the sternum generated the greatest and most consistent signal, while allowing for data collection from both lung fields simultaneously. Signals generated by respiration were collected in real-time, and post-collection data processing was implemented to visualize smooth transitions between inhalation and exhalation.

Pulmonary waveforms following human testing were generated for each trial. (Figure 7-3A to 7-3F). Between all volunteers, the approximate R_p range for respiratory cycles ranged between a minimum of 13.4 ohms and a maximum of 14.1 ohms. For most samples, basic data smoothing resulted in periodic waveforms, while others showed some small amounts of hysteresis or sensor drift over time. Basic demographics for all participants were recorded, including age and body mass index (BMI) (Figure 7-4A & Figure 7-4B). The predicted RR was also calculated using the time-series of each trial and compared to the actual participant RRs (Figure 7-4C). As previously described, differences were taken between local maxima and minima in the sensor output time-series waveforms to estimate the mean change in R_p breath (Figure 7-4F) per trial.

Immediately following scanning with our sensor, PFTs were recorded using the MIR Spirobank II®, which is a commercially available spirometer. Previous studies have shown that the Spirobank II® is an accurate and appropriate research tool for pulmonary testing [128]. Through this step, the FEV_1 and FVC of each participant was queried for comparison with R_p changes seen using the sensor (Figure 7-4D & Figure 7-4E). FEV_1 to FVC ratios less than 80% have been highly correlated with obstructive lung disease due to a greater decrease in FEV_1 than FVC [129, 130].

As such, it was ensured that the ratio of FEV$_1$ to FVC was >80% for all patients, with a mean of 97.7% in the cohort.
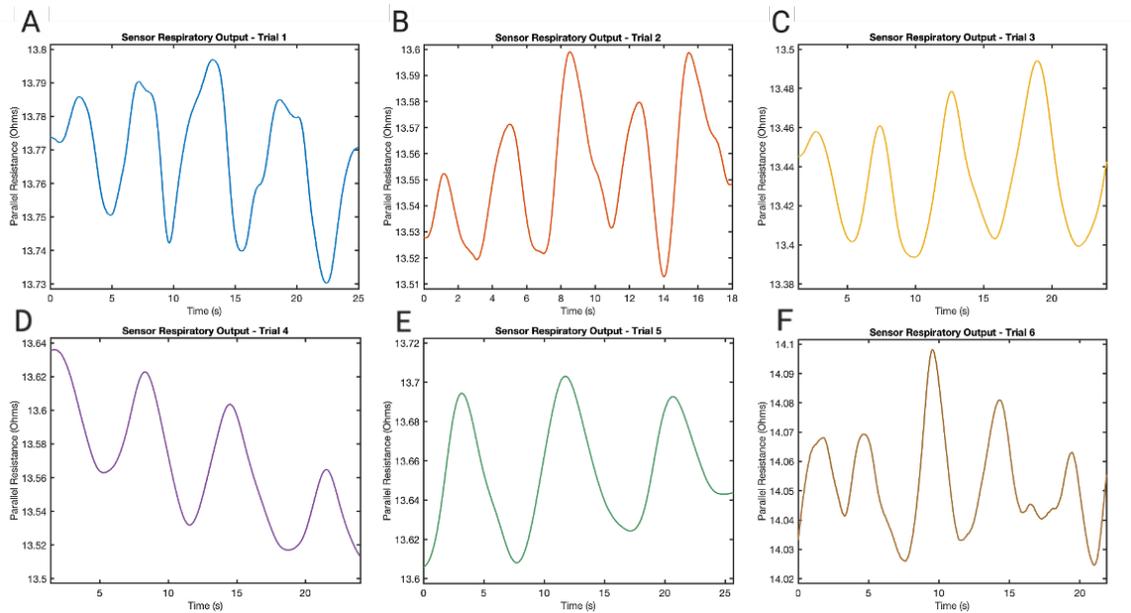
Figure 7-3: Sensor respiratory waveform output. **A-F**, Each waveform shows the unique pulmonary waveform, as generated by the sensor, for each trial in this study.
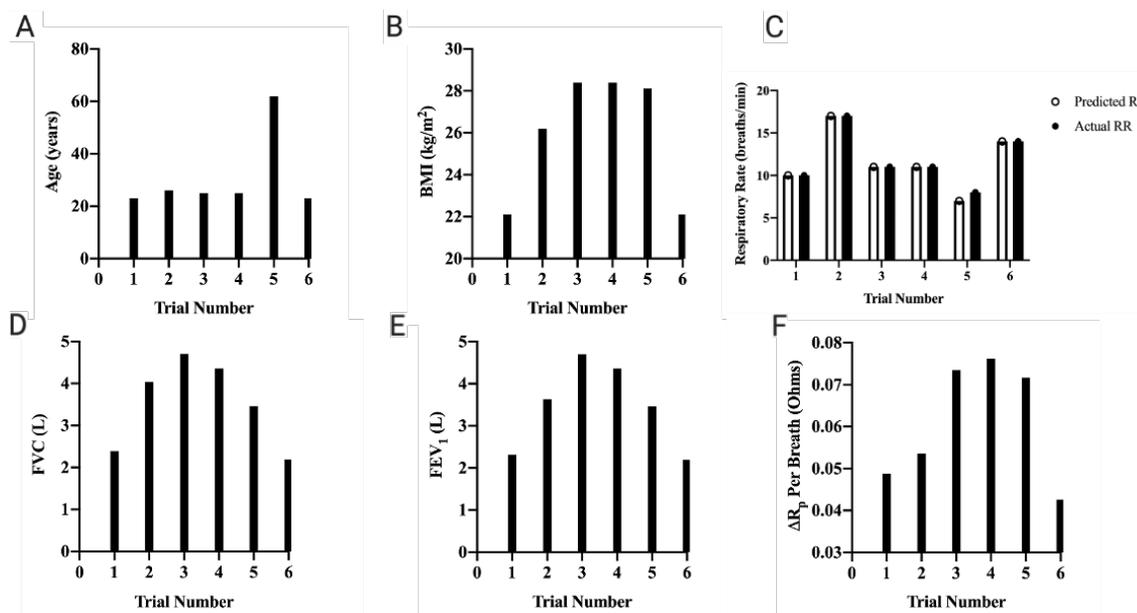
Figure 7-4: Participant variables and demographics. **A**, Age of participants by trial. **B**, Body mass index (BMI) of participants by trial. **C**, Respiratory rate of participants by trial. **D**, Forced vital capacity (FVC) of participants by trial. **E**, Forced expiratory volume in one second (FEV$_1$) of participants by trial. **F**, Change in R$_p$ of participants by trial.

Statistical regression analysis was performed to demonstrate the accuracy of sensor output as a predictor for RR, FEV$_1$, and FVC. Correlation between mean change in R$_p$ per breath and all three pulmonary variables demonstrated a statistically significant positive correlation, with RR showing the greatest predictive value (R^2=1.00, p-value<0.0001; Figure 7-5C). With respect to pulmonary volume metrics, regression analysis demonstrated that mean change in R$_p$ per breath was more closely correlated with FEV$_1$ (R^2=0.94, p-value=0.0012; Figure 7-5B) than FVC (R^2=0.90, p-value=0.0039; Figure 7-5A).
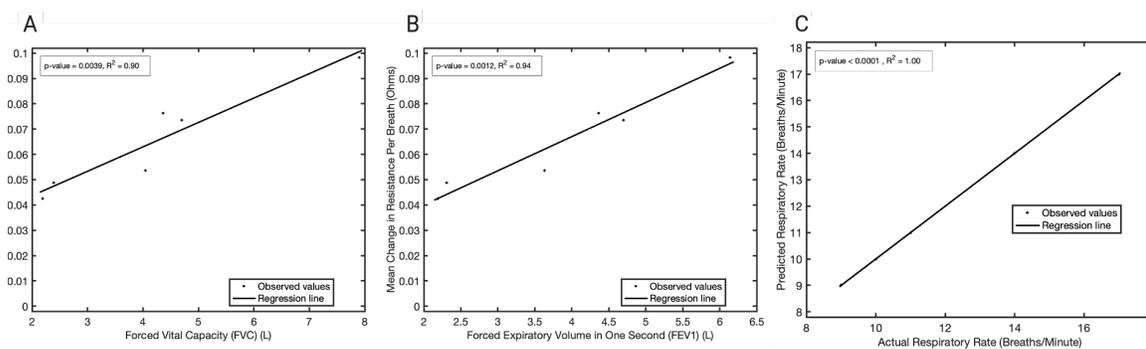
Figure 7-5: Regression analyses. **A**, Linear regression analysis correlating mean change in parallel resistance per breath and FVC. **B**, Linear regression analysis correlating mean change in parallel resistance per breath and FEV$_1$. **C**, Linear regression analysis correlating predicted and actual respiratory rates.

To achieve preliminary conductivity-based imaging of the thoracic cavity, the sensor was scanned vertically across 8 equidistant rows on the chest. Scanning the anterior chest wall started at the left mid-axillary line (row 1) and continued to the right mid-axillary line (row 8), vertically from the inferior border of the ribs to the clavicles superiorly. Real-time data was collected during each scan and data from all 8 scans were normalized, smoothed, and plotted as a heatmap (Figure 7-6A).

According to the underlying physics of the sensor, more conductive regions will result in lower R$_p$ values while less conductive regions will result in higher R$_p$ values. Within the thoracic cavity, large vessels branching off of the aorta and the heart would be expected to generate the largest ECD changes, while the air-filled lungs would produce the smallest ECD. On the same note, previous studies have found that the liver has the same conductivity as the heart at 1MHz (~0.3 S/m), and as a result, the liver would be expected to be visualized as well [86]. By overlaying

relevant thoracic organs in their appropriate locations, the conductivity-based heatmap can be better interpreted and understood (Figure 7-B). It is then clear that more conductive organs generate smaller signals on the heatmap, thus confirming our hypothesis.

In addition, finite element modeling (FEM) can be implemented to better understand the degree of ECD when the sensor is dynamically scanned across the chest. The magnetic flux densities generated within the thoracic cavity are greatest at the points nearest the sensor, although significant signal continues to be produced when the conductive target is 5cm from the sensor coil (Figure 7-C & Figure 7-D). Similarly, empty areas (modeled by air) generate little to no ECD signals within the model. This phenomenon is analogous to inhalation, during which the lungs and thoracic cavity are full of non-conductive room air.
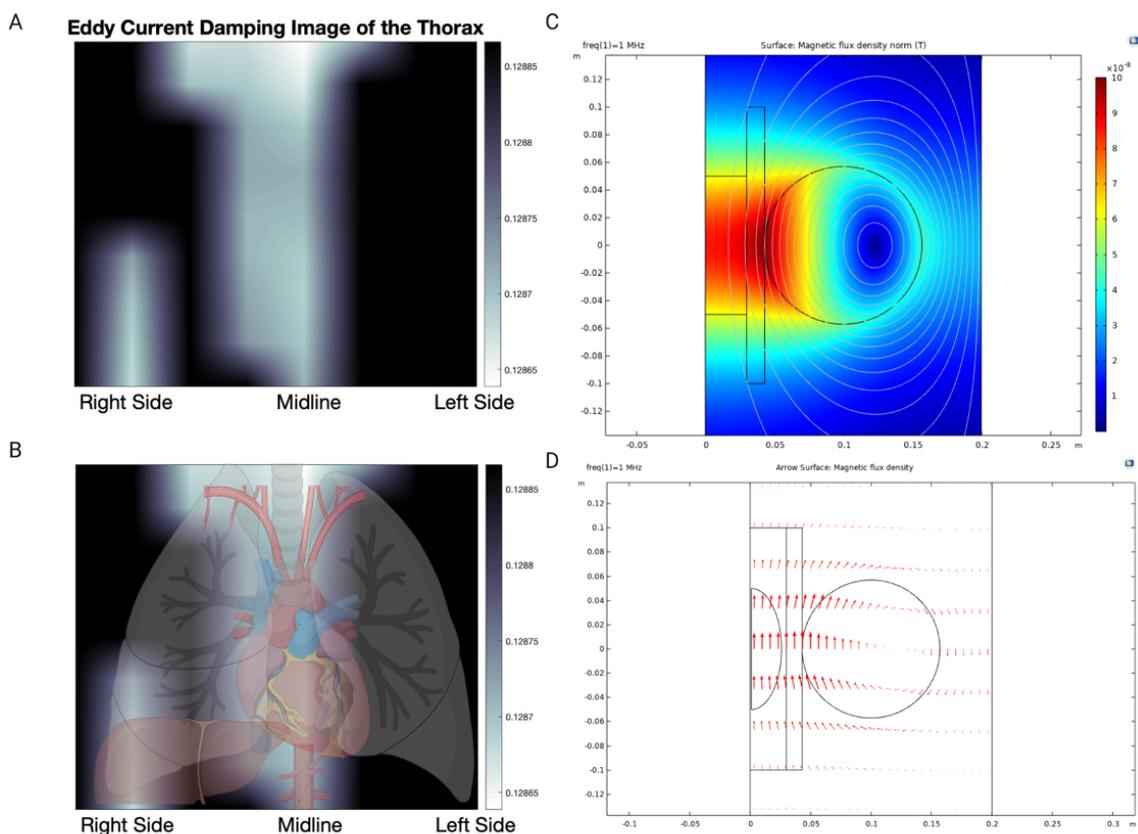
Figure 7-6: Heatmap images and finite element modeling. **A**, Heatmap generated using R_p values during dynamic scanning of the chest. More conductive regions are shown brighter, while less conductive regions are shown darker. **B**, Heatmap of the chest with overlaid anatomical landmarks. **C**, Finite element model (FEM) surface plot demonstrating magnetic flux density changes when the coil sensor is placed near skin and tissue. Red colors demonstrate the greatest damping, while blue colors demonstrate minimal damping. **D**, FEM arrow surface plot demonstrating magnetic flux density changes when the coil sensor is placed near skin, tissue, and vasculature. Larger arrows indicate the highest eddy current damping. Created with BioRender.com

7.5 Respiratory Sensor Discussion

Our characterization of a continuous wearable ECD pulmonary function sensor suggests translational feasibility and utility for high-risk patients or pulmonary conditions. In a series of first-in-man experiments using a static sensor, we demonstrate statistically significant linear correlations between sensor output and critical pulmonary metrics, including RR, FEV_1, and FVC. Changing to a dynamic scanning mode allowed for point-by-point conductivity measurements and heatmap-facilitated rudimentary imaging of the thoracic cavity, which can be further honed to provide near real-time imaging of the thoracic cavity in the field setting. FEM analysis confirmed our hypothesized magnetic field distributions and sensor behavior near conductive targets. Device safety was further confirmed as the sensor operated at 1MHz and generated magnetic fields of microtesla magnitudes.

The unique electromagnetic properties associated with ECD have resulted in several precedent devices, primarily used for industrial applications. ECD automobile braking systems have been developed that utilize the counteracting magnetic fields generated within the conductive target to slow vehicles. However, the ECD phenomenon has not yet been fully investigated within the context of biomedical research. Our investigation suggests that ECD sensors may accurately track changes in local conductivity, resulting from accumulation or removal of biological fluids or tissues. In addition, one major advantage of the sensor circuit is the low power consumption, which is of great importance for wearable sensors. In all trials, the sensor was powered via USB connection with a laptop, with a maximum current of 0.0027 amperes. On the same note, ECD sensors demonstrate an astounding price-to-accuracy tradeoff, and the sensor utilized in this study

cost less than $30 to construct, with a majority of the cost consumed by the commercial inductance-to-digital converter.

Recent work has described a mix of linear and non-linear relationships between bioimpedance and respiratory metrics, such as RR, with the general consensus being that the two are linearly correlated [131–136]. This attitude within the general pulmonary literature allowed for accurate model selection, as seen in the linear regression models shown as Figure 7-5. In fact, linear modeling demonstrated a statistically significant relationship between sensor output and pulmonary metrics, further supporting the nature of this relationship.

With regard to sensor construction, previous studies have investigated a wide range of sensors utilizing a vast array of physical phenomenon to predict pulmonary function. Specifically, acoustic biosensors have been developed for pulmonary diagnosis, RR, and wheeze detection [125, 137, 138], mechanical biosensors have been designed to measure strain during respiration [127], and electrical impedance tomography (EIT) has been shown to be an accurate method for non-invasive cardiopulmonary investigation [139, 140]. While each methodology boasts its own unique advantages and disadvantages, the sensor developed in this study is the first reported pulmonary ECD sensor in the literature. In addition, the sensor architecture described in this study allows for cheap, real-time, non-contact, wearable, continuous, and accurate biosensing and crude imaging that can easily interface with electronic health records or with a physician through telehealth services.

Of particular timely concern is COVID-19 and the wide range of presentations of ARDS following infection with the virus. Although PFTs are often not performed in acutely ill patients,

chronic pulmonary sequelae following COVID-19 ARDS may be accurately tracked with such a sensor. In addition, management of patients with chronic COVID-19 cannot rely on PFTs due to the high risk of respiratory droplet transmission of virus following forced expiration during spirometry [141]. As such, clinical understanding of PFTs in patients diagnosed with chronic COVID-19 sequelae continues to be limited, and non-contact wearable sensors may be able to provide additional patient-specific information regarding disease progression, and continuous sensing may hold information regarding reduced pulmonary functioning prior to clinical manifestations. To further minimize patient contact, these devices can be placed externally on the patients' clothing or interwoven within the shirt fabric, with Bluetooth transmission to a local computer for storage and analysis.

Furthermore, since March 2020, COVID-19 has reduced the number of inpatient and elective outpatient procedures in hospitals worldwide in an effort to limit disease spread [142]. Novel biosensors capable of monitoring pulmonary function accurately may present a distinct benefit during these times. Additional uses for lung transplant patients who require frequent PFTs and diagnosis of traumatic thoracic injury such as, hemothorax, pneumothorax, or hemidiaphragm may be possible in the field setting in the future with additional development of the ECD device. For all non-traumatic indications, continuous recording and digital interfacing provided by the sensor allow for remote PFT monitoring so that chronically ill patients can stay at home, thus minimizing potential COVID-19 exposure by reducing the frequency of hospital visits.

Limitations of this work include the requirement for the ECD sensor to be isolated from metallic objects and magnetic fields when scanning and a small series of participants. However, the number of volunteers recruited in this study was subject to Institutional limitations stemming

from the COVID-19 pandemic to prevent contact-based disease transmission. Furthermore, the resolution of heatmap-based images produced by the sensor is currently low and approximate due to the resolution of data output possible with the commercial sensor. Despite these limitations, our data shows robust evidence of the capacity of such a sensor for point-of-care pulmonary monitoring. Future work with a larger patient series aims at improving the circuit signal-to-noise ratio to improve sensor accuracy and boost the resolution of dynamic heatmap images produced through scanning. By doing so, such a device may provide information regarding critical lung metrics in sick and high-risk patients.

7.6 Conclusion

Overall, the same ECD sensor developed for stroke applications was also quite efficacious in measuring pulmonary waveforms, volumes, and conductivities. In light of the COVID-19 pandemic, ECD pulmonary sensors may allow for non-contact PFTs and lung monitoring in patients with COVID-19 or serious pulmonary illnesses. In addition to stroke detection and respiratory measurements, ECD sensors should be explored for a variety of medical conditions that may result in changes in bodily volumes or conductivities.

CHAPTER 8: CONCLUSION

This work demonstrates the role of ECD sensors in detecting, diagnosing, and imaging strokes. The proposed device has been tested and proven safe and efficacious within laboratory benchtop, human cadaver, and live human settings. In addition, rigorous mathematical and computational analysis of the developed sensor has been performed to ensure that the predicted sensor behavior matches its expected physical behavior.

Based on the findings of this thesis, future research evaluating ECD stroke sensors is warranted and may yield a potential alternative to CT and MRI imaging for stroke subtyping and triage. In fact, rapid, portable, and affordable stroke diagnosis and triage may facilitate patient management and accelerate time-to-treatment.

In addition, the same ECD sensor was evaluated for quantification of respiratory metrics, inspired by the COVID-19 pandemic which took place during this thesis. We demonstrate accurate and effective quantification of respiratory waveforms and volumes within seconds, allowing for non-contact PFTs in a time of social distancing and separation.

BIBLIOGRAPHY

1. Lopez AD, Mathers CD, Ezzati M, et al (2006) Global and regional burden of disease and risk factors, 2001: systematic analysis of population health data. Lancet 367:1747–1757

2. Donkor ES (2018) Stroke in the 21st Century: A Snapshot of the Burden, Epidemiology, and Quality of Life. Stroke Res Treat 2018:3238165

3. Ovbiagele B, Goldstein LB, Higashida RT, et al (2013) Forecasting the future of stroke in the United States: a policy statement from the American Heart Association and American Stroke Association. Stroke 44:2361–2375

4. Kivlahan C, Orlowski JM, Pearce J, et al (2016) Taking Risk: Early Results From Teaching Hospitals' Participation in the Center for Medicare and Medicaid Innovation Bundled Payments for Care Improvement Initiative. Acad Med 91:936–942

5. Germann AM, Al Khalili Y (2019) Anatomy, Head and Neck, Scalp Veins. In: StatPearls. StatPearls Publishing, Treasure Island (FL)

6. Li H, Ruan J, Xie Z, et al (2007) Investigation of the critical geometric characteristics of living human skulls utilising medical image analysis techniques. Int J Veh Saf 2:345–367

7. Nogles TE, Galuska MA (2020) Middle Cerebral Artery Stroke. In: StatPearls. StatPearls Publishing, Treasure Island (FL)

8. Grau AJ, Weimar C, Buggle F, et al (2001) Risk factors, outcome, and treatment in subtypes of ischemic stroke: the German stroke data bank. Stroke 32:2559–2566

9. Sacco RL (1995) Risk factors and outcomes for ischemic stroke. Neurology 45:S10–4

10. Jerrard-Dunne P, Cloud G, Hassan A, Markus HS (2003) Evaluating the genetic component of ischemic stroke subtypes: a family history study. Stroke 34:1364–1369

11. Casas JP, Hingorani AD, Bautista LE, Sharma P (2004) Meta-analysis of genetic studies in ischemic stroke: thirty-two genes involving approximately 18,000 cases and 58,000 controls. Arch Neurol 61:1652–1661

12. Bravata DM, Myers LJ, Reeves M, et al (2019) Processes of Care Associated With Risk of Mortality and Recurrent Stroke Among Patients With Transient Ischemic Attack and Nonsevere Ischemic Stroke. JAMA Netw Open 2:e196716

13. Son MK, Lim N-K, Kim HW, Park H-Y (2017) Risk of ischemic stroke after atrial fibrillation diagnosis: A national sample cohort. PLoS One 12:e0179687

14. Alshehri AM (2019) Stroke in atrial fibrillation: Review of risk stratification and preventive therapy. J Family Community Med 26:92–97

15. Hui C, Tadi P, Patti L (2020) Ischemic Stroke. In: StatPearls. StatPearls Publishing, Treasure Island

(FL)

16. Lin MP, Liebeskind DS (2016) Imaging of Ischemic Stroke. Continuum 22:1399–1423

17. Tong E, Hou Q, Fiebach JB, Wintermark M (2014) The role of imaging in acute ischemic stroke. Neurosurg Focus 36:E3

18. French BR, Boddepalli RS, Govindarajan R (2016) Acute Ischemic Stroke: Current Status and Future Directions. Mo Med 113:480–486

19. Catanese L, Tarsia J, Fisher M (2017) Acute Ischemic Stroke Therapy Overview. Circ Res 120:541–558

20. Cheng NT, Kim AS (2015) Intravenous Thrombolysis for Acute Ischemic Stroke Within 3 Hours Versus Between 3 and 4.5 Hours of Symptom Onset. Neurohospitalist 5:101–109

21. Barreto AD (2011) Intravenous thrombolytics for ischemic stroke. Neurotherapeutics 8:388–399

22. Papanagiotou Panagiotis, Ntaios George (2018) Endovascular Thrombectomy in Acute Ischemic Stroke. Circ Cardiovasc Interv 11:e005362

23. Meyer L, Politi M, Alexandrou M, et al (2017) Primary Aspiration Technique in Endovascular Stroke Treatment. Hellenic Journal of Radiology 2.: https://doi.org/10.36162/hjr.v2i2.118

24. Lapergue B, Blanc R, Guedin P, et al (2016) A Direct Aspiration, First Pass Technique (ADAPT) versus Stent Retrievers for Acute Stroke Therapy: An Observational Comparative Study. AJNR Am J Neuroradiol 37:1860–1865

25. Nogueira Raul G., Liebeskind David S., Sung Gene, et al (2009) Predictors of Good Clinical Outcomes, Mortality, and Successful Revascularization in Patients With Acute Ischemic Stroke Undergoing Thrombectomy. Stroke 40:3777–3783

26. Singer OC, Berkefeld J, Nolte CH, et al (2015) Mechanical recanalization in basilar artery occlusion: the ENDOSTROKE study. Ann Neurol 77:415–424

27. Kumar G, Shahripour RB, Alexandrov AV (2015) Recanalization of acute basilar artery occlusion improves outcomes: a meta-analysis. J Neurointerv Surg 7:868–874

28. Hemorrhagic Stroke (Bleeds). In: American Stroke Association. stroke.org/en/about-stroke/types-of-stroke/hemorrhagic-strokes-bleeds. Accessed 15 Jul 2020

29. Smajlović D, Kojić B, Sinanović O (2006) Five-year survival-after first-ever stroke. Bosn J Basic Med Sci 6:17–22

30. Tenny S, Thorell W (2020) Intracranial Hemorrhage. In: StatPearls. StatPearls Publishing, Treasure Island (FL)

31. Sun L, Clarke R, Bennett D, et al (2019) Causal associations of blood lipids with risk of ischemic stroke and intracerebral hemorrhage in Chinese adults. Nat Med 25:569–574

32. Chen C-J, Brown WM, Moomaw CJ, et al (2017) Alcohol use and risk of intracerebral hemorrhage.

Neurology 88:2043–2051

33. Shah RS, Cole JW (2010) Smoking and stroke: the more you smoke the more you stroke. Expert Rev Cardiovasc Ther 8:917–932

34. Biffi A, Anderson CD, Battey TWK, et al (2015) Association Between Blood Pressure Control and Risk of Recurrent Intracerebral Hemorrhage. JAMA 314:904–912

35. Woo D, Sekar P, Chakraborty R, et al (2005) Genetic epidemiology of intracerebral hemorrhage. J Stroke Cerebrovasc Dis 14:239–243

36. Etminan N, Buchholz BA, Dreier R, et al (2014) Cerebral aneurysms: formation, progression, and developmental chronology. Transl Stroke Res 5:167–173

37. Novitzke J (2008) The basics of brain aneurysms: a guide for patients. J Vasc Interv Neurol 1:89–90

38. Rutledge WC, Ko NU, Lawton MT, Kim H (2014) Hemorrhage rates and risk factors in the natural history course of brain arteriovenous malformations. Transl Stroke Res 5:538–542

39. Torpy JM, Burke AE, Glass RM (2010) JAMA patient page. Hemorrhagic stroke. JAMA 303:2312

40. Tepper D (2016) Thunderclap Headaches. Headache 56:1563–1564

41. Ojaghihaghighi S, Vahdati SS, Mikaeilpour A, Ramouz A (2017) Comparison of neurological clinical manifestation in patients with hemorrhagic and ischemic stroke. World J Emerg Med 8:34–38

42. Teasdale G, Jennett B (1974) Assessment of coma and impaired consciousness. A practical scale. Lancet 2:81–84

43. Naidech AM (2011) Intracranial hemorrhage. Am J Respir Crit Care Med 184:998–1006

44. Aguilar MI, Brott TG (2011) Update in intracerebral hemorrhage. Neurohospitalist 1:148–159

45. Wada Ryan, Aviv Richard I., Fox Allan J., et al (2007) CT Angiography "Spot Sign" Predicts Hematoma Expansion in Acute Intracerebral Hemorrhage. Stroke 38:1257–1262

46. Broderick J, Connolly S, Feldmann E, et al (2007) Guidelines for the Management of Spontaneous Intracerebral Hemorrhage in Adults: 2007 Update: A Guideline from the American Heart Association/American Stroke Association Stroke Council, High Blood Pressure Research Council, and the Quality of Care and Outcomes in Research Interdisciplinary Working Group: The American Academy of Neurology affirms the value of this guideline as an educational tool for neurologists. Stroke 38:2001–2023

47. Morgenstern LB, Hemphill JC 3rd, Anderson C, et al (2010) Guidelines for the management of spontaneous intracerebral hemorrhage: a guideline for healthcare professionals from the American Heart Association/American Stroke Association. Stroke 41:2108–2129

48. Schellinger PD, Fiebach JB, Hoffmann K, et al (2003) Stroke MRI in intracerebral hemorrhage: is there a perihemorrhagic penumbra? Stroke 34:1674–1679

49. Marler JR, Winters-Jones P, Emr P, eds. (1997) National Institute of Neurological Disorders and Stroke, Proceedings of a National Symposium on Rapid Identification and Treatment of Acute Stroke. Bethesda, Md: National Institutes of Health

50. Mohr JP, Biller J, Hilal SK, et al (1995) Magnetic resonance versus computed tomographic imaging in acute stroke. Stroke 26:807–812

51. Wintermark M, Reichhart M, Cuisenaire O, et al (2002) Comparison of admission perfusion computed tomography and qualitative diffusion- and perfusion-weighted magnetic resonance imaging in acute stroke patients. Stroke 33:2025–2031

52. Rymer MM (2011) Hemorrhagic stroke: intracerebral hemorrhage. Mo Med 108:50–54

53. Kidwell CS, Hsia AW (2006) Imaging of the brain and cerebral vasculature in patients with suspected stroke: advantages and disadvantages of CT and MRI. Curr Neurol Neurosci Rep 6:9–16

54. Pearce MS, Salotti JA, Little MP, et al (2012) Radiation exposure from CT scans in childhood and subsequent risk of leukaemia and brain tumours: a retrospective cohort study. Lancet 380:499–505

55. Mathews JD, Forsythe AV, Brady Z, et al (2013) Cancer risk in 680,000 people exposed to computed tomography scans in childhood or adolescence: data linkage study of 11 million Australians. BMJ 346:f2360

56. Smith-Bindman R, Lipson J, Marcus R, et al (2009) Radiation dose associated with common computed tomography examinations and the associated lifetime attributable risk of cancer. Arch Intern Med 169:2078–2086

57. Wei Y, Yu H, Geng J, et al (2018) Hospital efficiency and utilization of high-technology medical equipment: A panel data analysis. Health Policy and Technology 7:65–72

58. Santos RP, Pires ALA, Almeida RMVR, Pereira WCA (2017) Computed Tomography Scanner Productivity and Entry-Level Models in the Global Market. J Healthc Eng 2017:1304960

59. du Plessis A, le Roux SG, Guelpa A (2016) Comparison of medical and industrial X-ray computed tomography for non-destructive testing. Case Studies in Nondestructive Testing and Evaluation 6:17–25

60. Sistrom CL, McKay NL (2005) Costs, charges, and revenues for hospital diagnostic imaging procedures: differences by modality and hospital characteristics. J Am Coll Radiol 2:511–519

61. Food and Drug Administration (2010) De Novo Classification Request For Infrascan, Inc.'s Infrascanner Model 1000. https://www.accessdata.fda.gov/cdrh_docs/reviews/K080377.pdf. Apr 2020

62. Kellner CP, Sauvageau E, Snyder KV, et al (2018) The VITAL study and overall pooled analysis with the VIPS non-invasive stroke detection device. J Neurointerv Surg 10:1079–1084

63. Dowrick T Blochet C Holder (2015) In vivo bioimpedance measurement of healthy and ischaemic rat brain: implications for stroke imaging using electrical impedance tomography. Physiol Meas 36:1273–1282

64. Robertson CS, Zager EL, Narayan RK, et al (2010) Clinical evaluation of a portable near-infrared device for detection of traumatic intracranial hematomas. J Neurotrauma 27:1597–1604

65. Brogan RJ, Kontojannis V, Garara B, et al (2017) Near-infrared spectroscopy (NIRS) to detect traumatic intracranial haematoma: A systematic review and meta-analysis. Brain Inj 31:581–588

66. Persson M, Fhager A, Trefná HD, et al (2014) Microwave-based stroke diagnosis making global prehospital thrombolytic treatment possible. IEEE Trans Biomed Eng 61:2806–2817

67. Merunka I, Massa A, Vrba D, et al (2019) Microwave Tomography System for Methodical Testing of Human Brain Stroke Detection Approaches. Int J Antennas Propag 2019.: https://doi.org/10.1155/2019/4074862

68. Jickling GC, Sharp FR (2011) Blood biomarkers of ischemic stroke. Neurotherapeutics 8:349–360

69. Tang Y, Lu A, Aronow BJ, Sharp FR (2001) Blood genomic responses differ after stroke, seizures, hypoglycemia, and hypoxia: blood genomic fingerprints of disease. Ann Neurol 50:699–707

70. Chernavsky NE, Morcos M, Wu P, et al (2019) Technical assessment of a mobile CT scanner for image-guided brachytherapy. J Appl Clin Med Phys 20:187–200

71. Cooley CZ, Stockmann JP, Armstrong BD, et al (2015) Two-dimensional imaging in a lightweight portable MRI scanner without gradient coils. Magn Reson Med 73:872–883

72. Karakoc K, Suleman A, Park EJ (2016) Analytical modeling of eddy current brakes with the application of time varying magnetic fields. Appl Math Model 40:1168–1179

73. Ebrahimi B, Khamesee MB, Golnaraghi F (2008) Eddy current damper feasibility in automobile suspension: modeling, simulation and testing. Smart Mater Struct 18:015017

74. Maurya VK, Jalan R, Agarwal HP, et al (2011) Eddy current braking embedded system. International Journal of Applied Engineering and Technology 1:

75. Ma D-M, Shiau J-K (2011) THE DESIGN OF EDDY-CURRENT MAGNET BRAKES. Trans Can Soc Mech Eng 35:19–37

76. Pendrill A-M, Karlsteen M, Rödjegård H (2012) Stopping a roller coaster train. Phys Educ 47:728

77. Krause HJ, Hohmann R, Gruneklee M, Maus M (2000) Aircraft wheel and fuselage testing with eddy current and SQUID. INSIGHT-WIGSTON THEN NORTHAMPTON- 42:148–151

78. Bo L, Feilu L, Zhongqing J, Jiali L (2010) Eddy Current Array Instrument and Probe for Crack Detection of Aircraft Tubes. In: 2010 International Conference on Intelligent Computation Technology and Automation. pp 177–180

79. García-Martín J, Gómez-Gil J, Vázquez-Sánchez E (2011) Non-destructive techniques based on eddy current testing. Sensors 11:2525–2565

80. Ditchburn RJ, Burke SK, Posada M (2003) Eddy-Current Nondestructive Inspection with Thin Spiral Coils: Long Cracks in Steel. J Nondestr Eval 22:63–77

81. Instruments T (2016) Optimizing L Measurement Resolution for the LDC161x and LDC1101. http://www.ti.com/lit/an/snoa944/snoa944.pdf. Apr 2020

82. C. V. Dodd WED (1968) Analytical solutions to eddy-current probe-coil problems. J Appl Phys 39:2829–2838

83. Christiansen MG, Howe CM, Bono DC, et al (2017) Practical methods for generating alternating magnetic fields for biomedical research. Rev Sci Instrum 88:084301

84. MULL Ferrite Sheets. In: Laird. https://www.laird.com/emc-components/ferrite-sheets/mull-series/mull-ferrite-sheets. Apr 2020

85. Kandadai MA, Raymond JL, Shaw GJ (2012) Comparison of electrical conductivities of various brain phantom gels: Developing a "Brain Gel Model." Mater Sci Eng C Mater Biol Appl 32:2664–2667

86. Gabriel C, Peyman A, Grant EH (2009) Electrical conductivity of tissue at frequencies below 1 MHz. Phys Med Biol 54:4863–4878

87. Xiong Z, Yan X, Xin C, et al (2019) Intracerebral hemorrhage cadaver model for training in hematoma evacuation under endoscopy. J Clin Neurosci 63:272–277

88. James HK, Chapman AW, Pattison GTR, et al (2019) Systematic review of the current status of cadaveric simulation for surgical training. Br J Surg 106:1726–1734

89. Gilbody J, Prasthofer AW, Ho K, Costa ML (2011) The use and effectiveness of cadaveric workshops in higher surgical training: a systematic review. Ann R Coll Surg Engl 93:347–352

90. Held JM, McLendon RB, McEvoy CS, Polk TM (2019) A Reusable Perfused Human Cadaver Model for Surgical Training: An Initial Proof of Concept Study. Mil Med 184:43–47

91. Leblanc F, Champagne BJ, Augestad KM, et al (2010) A Comparison of Human Cadaver and Augmented Reality Simulator Models for Straight Laparoscopic Colorectal Skills Acquisition Training. J Am Coll Surg 211:250–255

92. Mendelow A, Gregson B, Fernandes H, et al (2005) Early surgery versus initial conservative treatment in patients with spontaneous supratentorial intracerebral haematomas in the International Surgical Trial in Intracerebral Haemorrhage (STICH): a randomised trial. The Lancet 365:387–397

93. Mendelow AD, Gregson BA, Rowan EN, et al (2013) Early surgery versus initial conservative treatment in patients with spontaneous supratentorial lobar intracerebral haematomas (STICH II): a randomised trial. Lancet 382:397–408

94. Yun J, Park JE, Lee H, et al (2019) Radiomic features and multilayer perceptron network classifier: a robust MRI classification strategy for distinguishing glioblastoma from primary central nervous system lymphoma. Scientific Reports 9

95. Tek P, Chiganos TC, Mohammed JS, et al (2008) Rapid prototyping for neuroscience and neural engineering. J Neurosci Methods 172:263–269

96. Cardone D, Merla A (2017) New Frontiers for Applications of Thermal Infrared Imaging Devices:

Computational Psychopshysiology in the Neurosciences. Sensors 17.: https://doi.org/10.3390/s17051042

97. Taylor JO, Meyer RS, Deutsch S, Manning KB (2016) Development of a computational model for macroscopic predictions of device-induced thrombosis. Biomech Model Mechanobiol 15:1713–1731

98. Sacco R, Carichino L, de Falco C, et al (2014) A multiscale thermo-fluid computational model for a two-phase cooling system. Comput Methods Appl Mech Eng 282:239–268

99. Hemphill J. Claude, Greenberg Steven M., Anderson Craig S., et al (2015) Guidelines for the Management of Spontaneous Intracerebral Hemorrhage. Stroke 46:2032–2060

100. Broderick JP, Adams HP Jr, Barsan W, et al (1999) Guidelines for the management of spontaneous intracerebral hemorrhage: A statement for healthcare professionals from a special writing group of the Stroke Council, American Heart Association. Stroke 30:905–915

101. Kidwell CS, Chalela JA, Saver JL, et al (2004) Comparison of MRI and CT for detection of acute intracerebral hemorrhage. JAMA 292:1823–1830

102. Gothäll H (2017) Modeling Irregular Shapes: How to Import Curve Data and Loft a Solid. In: COMSOL. https://www.comsol.com/blogs/modeling-irregular-shapes-how-to-import-curve-data-and-loft-a-solid/. Accessed 5 Jun 2020

103. Importing Curve Data and Lofting a Solid. In: COMSOL. https://www.comsol.com/model/importing-curve-data-and-lofting-a-solid-54331. Accessed 5 Jun 2020

104. Gabriel C (1996) Compilation of the Dielectric Properties of Body Tissues at RF and Microwave Frequencies

105. Shmukler M (2004) Density of blood. The Physics Factbook

106. Yu Y-L, Lee M-S, Juan C-J, Hueng D-Y (2013) Calculating the tumor volume of acoustic neuromas: comparison of ABC/2 formula with planimetry method. Clin Neurol Neurosurg 115:1371–1374

107. Roark C, Vadlamudi V, Chaudhary N, et al (2018) ABC/2 Method Does not Accurately Predict Cerebral Arteriovenous Malformation Volume. Neurosurgery 82:220–225

108. Won S-Y, Zagorcic A, Dubinski D, et al (2018) Excellent accuracy of ABC/2 volume formula compared to computer-assisted volumetric analysis of subdural hematomas. PLoS One 13:e0199809

109. Kleinman JT, Hillis AE, Jordan LC (2011) ABC/2: estimating intracerebral haemorrhage volume and total brain volume, and predicting outcome in children. Dev Med Child Neurol 53:281–284

110. Krieger SN, Streicher MN, Trampel R, Turner R (2012) Cerebral blood volume changes during brain activation. J Cereb Blood Flow Metab 32:1618–1631

111. Dempsey MF, Condon B, Hadley DM (2002) MRI safety review. Semin Ultrasound CT MR 23:392–401

112. Panych LP, Madore B (2018) The physics of MRI safety. J Magn Reson Imaging 47:28–43

113. Wyszkowska J, Shepherd S, Sharkh S, et al (2016) Exposure to extremely low frequency electromagnetic fields alters the behaviour, physiology and stress protein levels of desert locusts. Sci Rep 6:36413

114. Rosen AD (1994) Threshold and limits of magnetic field action at the presynaptic membrane. Biochim Biophys Acta 1193:62–66

115. Rosen AD (2010) Studies on the effect of static magnetic fields on biological systems. Piers Online 6:133–136

116. Celli BR, MacNee W, ATS/ERS Task Force (2004) Standards for the diagnosis and treatment of patients with COPD: a summary of the ATS/ERS position paper. Eur Respir J 23:932–946

117. Falliers CJ (1974) Letter: Self-measurements for asthma. JAMA 230:537–538

118. Redding GJ, Walund L, Walund D, et al (1990) Lung function in children following empyema. Am J Dis Child 144:1337–1342

119. Lombardi C, Milanese M, Cottini M (2020) Rethinking respiratory function laboratories in the era of coronavirus disease 2019: Considerations for today and the day after. Ann Allergy Asthma Immunol 125:210–211

120. Crimi C, Impellizzeri P, Campisi R, et al (2020) Practical considerations for spirometry during the COVID-19 outbreak: Literature review and insights. Pulmonology. https://doi.org/10.1016/j.pulmoe.2020.07.011

121. Wong AW, Fidler L, Marcoux V, et al (2020) Practical considerations for the diagnosis and treatment of fibrotic interstitial lung disease during the COVID-19 pandemic. Chest

122. Jindal SK, Jindal A, Moitra S, Others (2020) Problems of management of non-corona respiratory diseases in the era of COVID-19. International Journal of Noncommunicable Diseases 5:63

123. Task Force of Pulmonary Function Testing and Clinical Respiratory Physiology, Chinese Association of Chest Physicians, Pulmonary Function Testing Group, Respiratory Therapeutics Group, Chinese Thoracic Society (2020) [Expert consensus on pulmonary function testing during the epidemic of coronavirus disease 2019]. Zhonghua Jie He He Hu Xi Za Zhi 43:302–307

124. Phan DH, Bonnet S, Guillemaud R, et al (2008) Estimation of respiratory waveform and heart rate using an accelerometer. Conf Proc IEEE Eng Med Biol Soc 2008:4916–4919

125. Mimoz O, Benard T, Gaucher A, et al (2012) Accuracy of respiratory rate monitoring using a non-invasive acoustic method after general anaesthesia. Br J Anaesth 108:872–875

126. AL-Khalidi FQ, Saatchi R, Burke D, et al (2011) Respiration rate monitoring methods: A review. Pediatr Pulmonol 46:523–529

127. Chu M, Nguyen T, Pandey V, et al (2019) Respiration rate and volume measurements using wearable strain sensors. npj Digital Medicine 2

128. Degryse J, Buffels J, Van Dijck Y, et al (2012) Accuracy of office spirometry performed by trained primary-care physicians using the MIR Spirobank hand-held spirometer. Respiration 83:543–552

129. Lambert A, Drummond MB, Wei C, et al (2015) Diagnostic accuracy of FEV1/forced vital capacity ratio z scores in asthmatic patients. J Allergy Clin Immunol 136:649–653.e4

130. Vaz Fragoso CA, Concato J, McAvay G, et al (2010) The ratio of FEV1 to FVC as a basis for establishing chronic obstructive pulmonary disease. Am J Respir Crit Care Med 181:446–451

131. Seppa* V, Viik J, Hyttinen J (2010) Assessment of Pulmonary Flow Using Impedance Pneumography. IEEE Transactions on Biomedical Engineering 57:2277–2285

132. Seppä V-P, Viik J, Naveed A, et al (2009) Signal waveform agreement between spirometer and impedance pneumography of six chest band electrode configurations. In: World Congress on Medical Physics and Biomedical Engineering, September 7 - 12, 2009, Munich, Germany. Springer Berlin Heidelberg, pp 689–692

133. Seppä V-P, Hyttinen J, Uitto M, et al (2013) Novel electrode configuration for highly linear impedance pneumography. Biomed Tech 58:35–38

134. Malmberg LP, Seppä V-P, Kotaniemi-Syrjänen A, et al (2017) Measurement of tidal breathing flows in infants using impedance pneumography. Eur Respir J 49.: https://doi.org/10.1183/13993003.00926-2016

135. Grenvik A, Ballou S, McGinley E, et al (1972) Impedance Pneumography: Comparison between Chest Impedance Changes and Respiratory Volumes in 11 Healthy Volunteers. Chest 62:439–443

136. Koivumäki T, Vauhkonen M, Kuikka JT, Hakulinen MA (2012) Bioimpedance-based measurement method for simultaneous acquisition of respiratory and cardiac gating signals. Physiol Meas 33:1323–1334

137. Rao A, Huynh E, Royston TJ, et al (2019) Acoustic Methods for Pulmonary Diagnosis. IEEE Rev Biomed Eng 12:221–239

138. Li S-H, Lin B-S, Tsai C-H, et al (2017) Design of Wearable Breathing Sound Monitoring System for Real-Time Wheeze Detection. Sensors 17.: https://doi.org/10.3390/s17010171

139. Putensen C, Hentze B, Muenster S, Muders T (2019) Electrical Impedance Tomography for Cardio-Pulmonary Monitoring. J Clin Med Res 8.: https://doi.org/10.3390/jcm8081176

140. Tomicic V, Cornejo R (2019) Lung monitoring with electrical impedance tomography: technical considerations and clinical applications. J Thorac Dis 11:3122–3135

141. Desai AN, Patel P (2020) Stopping the Spread of COVID-19. JAMA 323:1516

142. Khullar D, Bond AM, Schpero WL (2020) COVID-19 and the Financial Health of US Hospitals. JAMA 323:2127–2128